Study of Aqueous Surfactant Systems with Focus on Interfacial Adsorption Layers

Dissertation zur Erlangung des Doktorgrades der
Naturwissenschaften (Dr. rer. nat.) an der Fakultät
Chemie und Pharmazie der Universität Regensburg

vorgelegt von

Alexander Anton Dietz

aus Regensburg

im Jahr 2020

Promotionsgesuch eingereicht am 01.10.2020

Diese Arbeit wurde angeleitet von: Prof. Dr. Hubert Motschmann.

Danksagung

Zu aller erst möchte ich mich ganz herzlich bei Prof. Hubert Motschmann für die Anleitung dieser Arbeit bedanken. Durch seine ausgewogene Art der Betreuung herrschte stets ein angenehmes und vertrauensvolles Klima, was es mir ermöglichte an der Schnittstelle zwischen Chemie und Physik Elemente beider Teilbereiche in dieser Arbeit zu vereinen.

Ein weiterer Dank gilt Dr. Peter Karageorgiev, der mich in der Anwendung und Durchführung der Summen-Frequenz-Spektroskopie unterwiesen hat und mir bei technischen Fragen mit Rat und Tat zur Seite stand.

Meinen Kollegen aus der Arbeitsgruppe Matthias Hofmann, Eva Brandes, Ulrike Paap und Dominik Feucht, aber auch meinen Büronachbarn Katharina Häckl, Damian Brock, Claudia Benkert und Florian Kroiss gilt besonderer Dank für die gute Zusammenarbeit und die nette Arbeitsatmosphäre.

Hervorheben möchte ich ebenfalls den generell guten Zusammenhalt der Mitarbeiter untereinander in den Arbeitskreisen der *Solution Chemistry Research Groups*, welcher sich nicht nur auf die Arbeitszeit erstreckte. Die sommerlichen Grillabende, die Kanufahrten auf der Naab und die geselligen Schafkopfrunden werden mir immer in guter Erinnerung bleiben.

Danken möchte ich auch Katrin, Tobi und meinen Eltern Gerlinde und Karl, die mich in meinem wissenschaftlichen Interesse immer gefördert und unterstützt haben und mir, wenn es hin und wieder nötig war, auch einiges an Geduld und Verständnis entgegengebracht haben.

Information

The present thesis is based on the work carried out between April 2017 and June 2020 in the Institute of Physical and Theoretical Chemistry of the University of Regensburg under the supervision of Prof. Dr. Hubert Motschmann.

Submitted:	01.10.2020
Colloquium:	03.12.2020
1^{st} Referee:	Prof. Dr. Hubert Motschmann
2^{nd} Referee:	Prof. Dr. Rainer Müller
3^{rd} Referee:	Prof. Dr. Arno Pfitzner
Chair:	Prof. Dr. Oliver Tepner

Contents

1. Introduction

The study of surfaces and interfaces is a scientific field which overlaps with nearly every sub-discipline of physics and chemistry. This is because the local molecular arrangement and composition at an interface or phase boundary is different compared to the respective bulk phases, which in many cases awards that environment with interesting and unusual properties. That in particular is the basis for phenomena like heterogeneous catalysis,[1,2] the structure and functionality of biological membranes,[3,4] or the longevity of thermodynamically unstable dispersions such as foams and emulsions.[5,6]

The study and description of interfaces and surfaces date back more than a century. The pioneering works of the likes of Gibbs,[7] Langmuir,[8] or Blodgett[9] paved the way for today's understanding of thin organic films and monolayers on liquids and solid substrates. In the following decades, numerous models with increasing complexity have been developed to describe the thermodynamics and structure of an interface on a molecular level. Thus, it is now possible to account for a zoo of different factors like surface charge,[10] molecular orientation,[11] phase transitions,[12] or non-ideal molecular interactions,[13] among others, when modelling the state of an interface.

However, the major obstacle in the experimental study and analysis of the interface is the small spatial dimension of that particular region. The depth of an interfacial layer only extends over a few molecules. Hence, with most of the common analytical techniques, it is almost impossible to separate the surface from the vastly dominating bulk response. Therefore, the emerging field of surface science created the demand for methods and tools which solely probe the interface. Techniques like EELS,[14] XPS[15] or STM[16] are sensitive for the surface but also require vacuum conditions and are therefore not suited for in-situ characterisation of air/water interfaces. X-ray or neutron reflectometry, however, can probe latter systems and deliver detailed insights concerning the structure of thin interfacial layers.[17] Unfortunately, access to these methods is very limited, since they require huge experimental effort, which can only be provided by a few facilities worldwide.

Vibrational spectroscopy appears as another candidate for the non-destructive investigation of surfaces and interfaces. Since linear optical spectroscopy suffers from the weak surface-to-bulk signal ratio, special adjustments were made to provide surface sensitivity. Although it is not completely surface specific, IRRAS[18] can probe a thin surface film by measuring the reflected intensity spectrum of a linear polarized infra-red (IR) beam under a grazing angle-of-incidence. The same holds for DRIFTS,[19] a technique which employs multiple diffuse reflection for the characterisation of small coated particles.

The increasing availability of reliable pulsed laser systems in recent years made it possible to also use non-linear optical effects for the characterisation of surfaces. Employing the second-order non-linear optical process of sum-frequency generation (SFG) for vibrational spectroscopy, as described by Shen and co-workers[20] in the late 1980s, has since then become a staple in modern surface science. This method's "blindness" for bulk media relies on SFG's inherent precondition of a complete absence of any form of centrosymmetry in the molecular environment of the probe.

In the present work, the amphiphilic properties of selected surface-active compounds will be tuned by exchanging certain molecular building blocks. Further, these compounds will be used to prepare binary mixtures with other surface-active substances. These systems will be studied via means of vibrational SFG-spectroscopy in combination with more conventional surface analytic techniques. The presented results shed some light on the molecular structure and composition of the self-assembled monolayers located at the interface between air and water.

2. Fundamentals

2.1. Surface Tension

With a value of $72.8\,\mathrm{mN\,m^{-1}}$ (at $20\,^{\circ}\mathrm{C}$) water has an extraordinarily high surface tension, as compared to other common solvents like acetone ($25.2\,\mathrm{mN\,m^{-1}}$), cyclohexane ($24.9\,\mathrm{mN\,m^{-1}}$), ethanol ($22.1\,\mathrm{mN\,m^{-1}}$) or pyridine ($38.0\,\mathrm{mN\,m^{-1}}$).[21] The reason behind that is the pronounced ability of water to form hydrogen bonds. This type of attractive force is responsible for strong cohesive interactions between individual water molecules. As in any typical liquid, water molecules are distributed isotropically within the bulk phase. Following the simplified textbook picture, such a distribution implies a completely occupied coordination sphere of nearest neighbours for any molecule in the bulk phase. By contrast, at the phase boundary the number of interaction partners present, here expressed via the coordination number Z, abruptly declines. Consequently, the coordination sphere of molecules in the topmost layer is no longer saturated. This leads to different energies for a molecule in bulk and surface (E_{bulk} and E_{surface}), which manifest as the surface tension γ. Assuming a molecular area of a_0 and pairwise additive interaction energies $W_{\mathrm{pair}} < 0$ between neighbouring molecules, the required work for pushing molecules from the bulk into the phase boundary (and thus creating a fresh interface) can be estimated roughly via the following relation:[22]

$$\gamma \simeq \frac{E_{\mathrm{surface}} - E_{\mathrm{bulk}}}{a_0} = \frac{W_{\mathrm{pair}} \cdot (Z_{\mathrm{surface}} - Z_{\mathrm{bulk}})}{2a_0} \tag{2.1}$$

A schematic illustration of the model is given in figure 2.1. From a macroscopic point of view, this explains why water drops strive for minimisation of their surface area. One of the implications of the strong interfacial tension of water is the dome-shaped profile (meniscus) of the phase boundary when water in a glass beaker is filled up to the rim. Furthermore, the ability of certain arthropods to walk on the water surface without sinking in, as if it was an impermeable membrane, is another vivid example for the strong surface tension of water.[23,24]

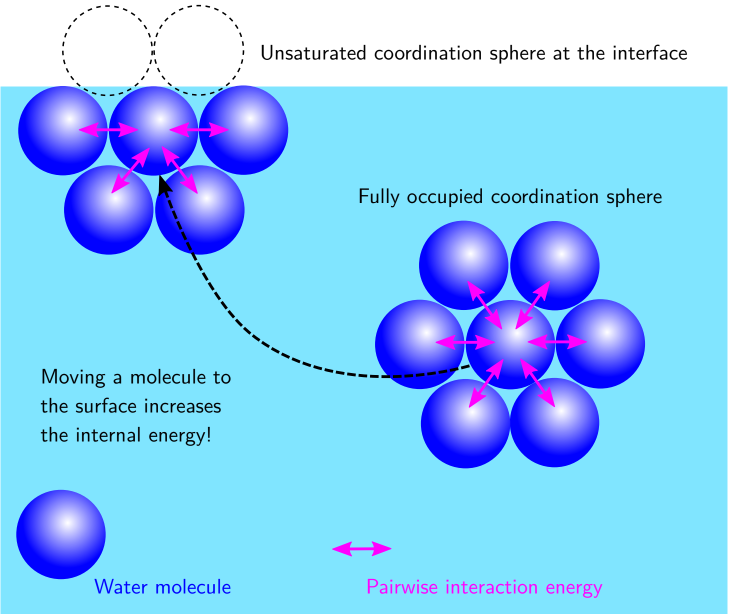

Figure 2.1.: Classical textbook picture concerning the origin of the surface tension of water (blue spheres). Due to net negative pairwise interactions between neighbouring molecules it is energetically favourable for a water molecule to be situated in the bulk phase rather than at the phase boundary.

Strictly speaking in terms of thermodynamics, the surface tension γ refers to the energy which is required to increase the surface area of a system by the amount of dA. The according description of the Gibbs energy in its differential form dG is given via the following relation:

$$dG = V dp - S dT + \sum_i \mu_i dn_i + \gamma dA \tag{2.2}$$

This complete expression also accounts for the quantities of Volume V, pressure p, entropy S, temperature T, as well as chemical potential μ_i and amount n_i of substance i. It will be used in the following section to derive a mathematical expression for the physicochemical process of surfactant adsorption at an air-water interface.

2.2. Adsorption to the Interface

The addition of surface-active agents, so-called surfactants, to pure water helps to significantly reduce its surface tension by the formation of a self-assembled monolayer at the phase boundary of the liquid solution. This type of compound usually possesses two or more moieties with opposing preferences regarding its molecular environment. The hydrophilic contribution is due to a moiety referred to as headgroup, for instance, a polar non-ionic moiety like polyoxyethylene alcohol or a monoglyceride group. Another common type of headgroup exhibits zwitterionic functionalities as in long-chain amino acids or sulfobetaines. The third category to be named here possesses dissociable ion pairs, such as organic salts of carboxylate (anionic) or quaternary ammonium ions (cationic).[25]

To render a hydrophilic compound surface-active, a rest with strong hydrophobic tendencies has to be introduced. In most cases, this is achieved via an alkane chain with a total length of eight or more carbon atoms. The resulting amphiphilicity leads to accumulation at air-water interfaces since each of the respective parts could be situated in an energetically favourable environment-hydrophilic headgroups facing the solution phase and nonpolar alkyl residues pointing towards the air phase. The respective physical process is referred to as adsorption. How much surfactant effectively adsorbs at a certain concentration, and thus decreases the surface tension, depends on the individual surfactant species, i.e. the balance between hydrophilic and lipophilic tendencies of the latter.[25,26] A typical curve for the concentration dependence is shown in figure 2.2.

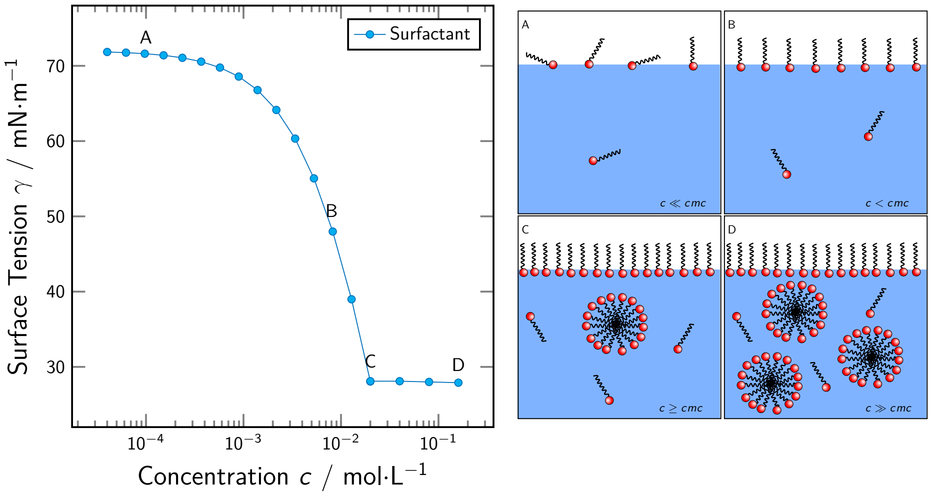

Figure 2.2.: Left: Exemplary dependence between surface tension and surfactant concentration. To get a better idea of the adsorption process the curve is divided into four subregions A,B,C,D. Right: Schematic illustration of the ongoing aggregation process for different surfactant concentrations. The monolayer density increases until the cmc is reached. From there on, additional surfactant is incorporated into micelles.

A peculiarity of most surfactant solutions is the formation of molecular clusters above the so-called critical micellar concentration (cmc). In these structures, alkyl tails agglomerate and water is mostly expelled from the hydrophobic micelle core as a consequence. The individual nature of the respective surfactant, as well as the solvent, defines the shape of the aggregates. Properties like steric demand of the hydrophobic backbone, attractive/repulsive headgroup interaction or ionic strength of the solution play a decisive role here. In the literature, a broad variety of micellar shapes has been reported - spheres, disks, rods, leaflets or multilayered structures[27] - only to name a few. Exceeding the threshold concentration for aggregation usually manifests in a distinct kink in the plot of surface tension (γ) vs. concentration (c). This is due to the fact, that from this point on, the surface layer is no longer the sole possibility for a surrounding, which satisfies both preferences of the amphiphilic molecule. Therefore, the surface tension levels off beyond the cmc because additional surfactant is rather incorporated into micellar structures than in the pre-saturated surface layer.[28]

An early approach to describe the thermodynamics of a surfactant solution interface in the pre-micellar regime is the model of Gibbs.[7] Therein, the gradual transition in the molecular distribution along the real depth profile z of a phase boundary is summarised by the aid of a pseudo two-dimensional interface. To do so, one assumes the neighbouring liquid and vapour phases to possess constant concentrations $c_i^{\mathrm{bulk}} = c_i(z \to +\infty)$ and $c_i^{\mathrm{vap}} = c_i(z \to -\infty)$ of solvent and solute (i). Both phases are separated by an infinitely thin layer - the so-called Gibbs dividing plane.

As shown in figure 2.3, deviations from $c_i(z \to \pm\infty)$ within the surface layer, which in reality covers a finite depth, are captured by the introduction of a new quantity: the surface excess Γ_i.

$$\Gamma_i = \frac{n_i^s}{A} \tag{2.3}$$

Within the Gibbs model Γ_i represents the excess amount n_i^s of species i

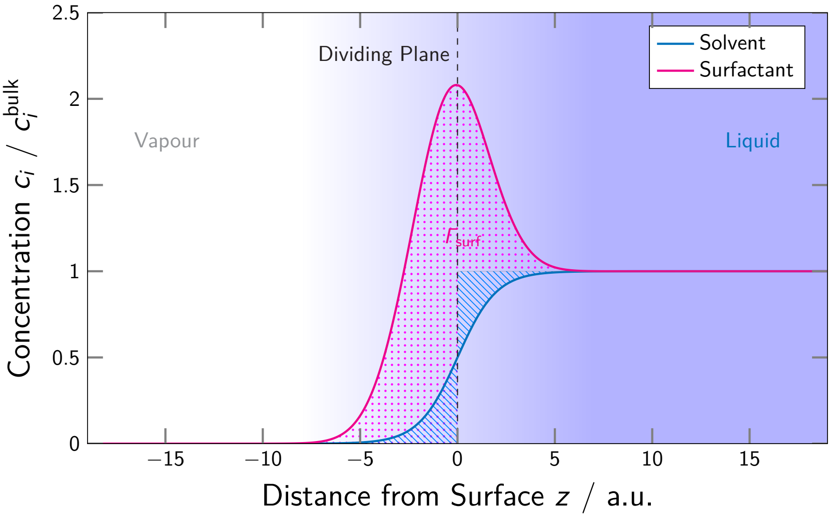

Figure 2.3.: Definition of the dividing surface according to the Gibbs model for a binary mixture of water and a non-ionic surfactant. To maintain clarity, the local concentration c_i is normalized with its asymptotic value in the bulk liquid. The positioning of $z = 0$ yields zero for the surface excess of solvent molecules, as shown by the congruent blue hatched areas. Contrarily, on either side of the dividing plane, $c_{\text{surf}}(z)$ deviates positively from the bulk concentration, which gives a net positive surface excess of surfactant Γ_{surf}. Figure inspired by ref. [22].

per unit area A of the interface. In accordance, Γ_i is obtained by integration of the local concentration excess on either side of the dividing surface.

$$\Gamma_i = \int_{-\infty}^{0} (c_i(z) - c_i^{\text{vap}})\, dz + \int_{0}^{\infty} \left(c_i(z) - c_i^{\text{bulk}}\right) dz \tag{2.4}$$

Per definition, the positioning of the two-dimensional model interface ($z = 0$) has to fulfil the precondition of yielding zero surface excess for the solvent. To derive Γ_i from experimental data, the Gibbs-Duhem relation can be employed. Under isothermal and isobaric conditions it is expressed as:

$$0 = A d\gamma + \sum_i n_i^s d\mu_i. \tag{2.5}$$

In the above equation the chemical potential is then replaced by its activity-dependent expression ($d\mu_i = RTd\ln a_i$). Furthermore, Gibbs' definition of the dividing plane eliminates the term which corresponds to the surface excess of solvent ($\Gamma_1 = 0$). Consequently, the following expression for a binary mixture of solvent 1 and non-ionic surfactant 2 is obtained:

$$\begin{aligned} -d\gamma &= \sum_i \frac{n_i^s}{A} d\mu_i = \Gamma_1 d\mu_1 + \Gamma_2 d\mu_2 \\ &= \Gamma_2 \cdot RTd\ln a_2 = \Gamma_2 \cdot RTd\ln c_2 f_2 \end{aligned} \tag{2.6}$$

Above equation reveals, that the surface excess Γ_2 is accessible by simply determining the derivative of the experimentally measured surface tension plot.

$$\Gamma_2 = -\frac{1}{RT} \cdot \frac{d\gamma}{d\ln a_2} \tag{2.7}$$

However, for a rigorous thermodynamic treatment, the content of surfactant in solution has to be expressed by the activity a_2, which would require further measurements for its determination or the application of certain approximate models. Conveniently, most surfactants need only minimal amounts to significantly lower the surface tension ($< 1 \times 10^{-2}\,\mathrm{mol\,L^{-1}}$). Hence, the activity coefficient f_2 is very close to unity, and a_2 can be replaced by the concentration, i.e. the molarity c_2.

In accordance with the Gibbs model, the kink in the γ vs. c plot and the virtually constant surface tension above the cmc implies that the activity reaches a plateau value at that concentration. This is due to the fact, that the activity of the solution, and thus the surface tension, can mainly be attributed to the residual monomeric species of the dispersed surfactant. Above the cmc, additional solute monomer is integrated into micelles, where its contribution to the activity becomes negligibly small.

2.3. Charged Surfactants and Monolayers

Up to this point, the adsorption process of a surfactant to the interface has proven itself to appear rather straight forward. However, the above considerations are limited to binary mixtures of nonionic surfactants with water. As soon as electrostatic contributions come into play, the situation complicates quite a bit.

In aqueous solution, the ionic surfactant RX dissociates into its respective anionic and cationic counterparts, as any other inorganic salt XY would do. Since adsorption of the surface-active ion R alone would disobey the electroneutrality condition, the establishment of an interfacial layer requires co-adsorption by the per se surface-inactive counterion X. Expressed within the model of Gibbs, this consequently adds a pre-factor n to the above relation.[29]

$$d\gamma = RT \cdot (\Gamma_\mathrm{R} d \ln a_\mathrm{R} + \Gamma_\mathrm{X} d \ln a_\mathrm{X}) = nRT \cdot \Gamma_\mathrm{R} d \ln a_\mathrm{R} \tag{2.8}$$

For the case of a bare binary water/surfactant mixture, n is equal to the number of ions involved in the undissociated salt species. In an extension of the model, which accounts for the presence of indifferent electrolyte XY, n becomes a function of surfactant- and salt concentration with the limiting case of $n = 1$ for swamping amounts of XY. Note, that the presented approach delivers the surface excess as an integral quantity and offers no information about the depth of the surface layer and the ion distribution therein. However, these circumstances might become important for the correct interpretation of experimental data stemming from surface-specific techniques like sum-frequency generation spectroscopy, as shown later on in this work.

To address this issue, multiple models have been developed,[30–35] and

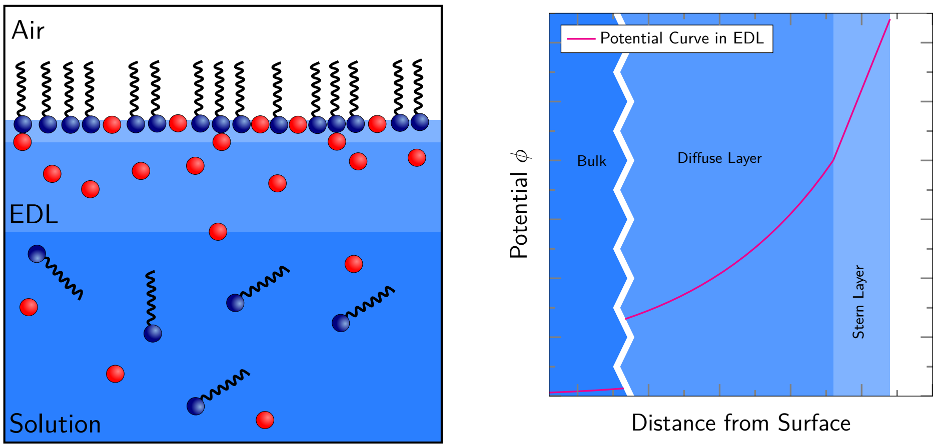

Figure 2.4.: Adsorption model for ionic surfactants as shown in ref. [30]. Left: Schematic drawing of the depth profile of a solution of ionic surfactant (blue heads) and counterions (red spheres) which build up the electrochemical double layer (EDL). Right: Corresponding electric potential curve along the surface normal towards the bulk phase crossing the Stern- and the diffuse ion layer.

exemplarily one of them is sketched in figure 2.4. What all these approaches have in common, is that they build upon the foundations laid down by Gouy and Chapman.[36,37] They proposed the model of an electrochemical double layer (EDL) adjacent to a solid electrode surface (with a certain charge density) when immersed in an aqueous electrolyte solution. The interplay between electrostatic interactions favouring a tightly bound layer of counterions and spatial randomisation by thermal motion establishes a non-uniform distribution of ions in the proximity of the surface. This, in turn, gives rise to an electric potential $\phi(x)$, which vanishes with increasing distance x from the surface. The ion distribution, i.e. the free charge density is given by the Poisson equation:

$$\epsilon_0 \epsilon_\mathrm{r} \frac{d^2\phi}{dx^2} = -\rho(x) \tag{2.9}$$

, where ϵ_0 is the permittivity of free space and ϵ_r is the solution dielectric constant.[29] $\rho(x)$ summarises all free ions i in solution and obeys classical

Boltzmann statistics. In the following expression F refers to the Faraday constant, z_i to the ion valency and $c_{i,0}$ to the bulk concentration of species i, k_B to the Boltzmann factor and e_0 to the elementary charge.

$$\rho(x) = F \sum_i z_i c_{i,0} \cdot \exp\left(-\frac{e_0 z_i \phi(x)}{k_B T} \right) \tag{2.10}$$

Equations 2.9 and 2.10 yield a second-order non-linear differential equation, which can be solved with adequate boundary conditions.

For the estimation of the dimensions of electrostatic interaction in aqueous solution, it might be useful to introduce a set of different characteristic length-scale parameters at this point. The Bjerrum length $\lambda_\mathrm{B} = e_0^2 \cdot (4\pi\epsilon_0\epsilon_r k_B T)^{-1}$ marks the distance at which the thermal energy $k_B T$ becomes equal to the electrostatic interaction between two unit charges.[38] In water at room temperature it is $\simeq 7\,\text{Å}$. For a planar surface with charge density σ, the depth of the diffuse counterion layer is characterised with the Gouy-Chapman length $\lambda_\mathrm{GC} = 2\epsilon_0\epsilon_r k_B T \cdot (e_0|\sigma|)^{-1} = e_0 \cdot (2\pi\lambda_\mathrm{B}|\sigma|)^{-1}$ in absence of added electrolyte.[39] The exponential decay rate of the electric potential near the surface is given via the Debye screening length κ^{-1} if excess salt is present in solution.[40] In the following expression I refers to the ionic strength of the solution and N_A to Avogadros number.

$$\begin{aligned} \kappa^{-1} &= \sqrt{\frac{\epsilon_0\epsilon_r RT}{2N_\mathrm{A}^2 e_0^2 I}} = \frac{1}{\sqrt{8\pi N_A \lambda_\mathrm{B} I}} \\ &\simeq \frac{0.304\,\mathrm{nm}}{\sqrt{I[\mathrm{mol\,L^{-1}}]}} \qquad \text{(aqueous solutions at 293 K)} \end{aligned} \tag{2.11}$$

The major shortcoming of the Gouy-Chapman model is that it treats the ions as point charges, which would in principle allow them to come infinitely close to the interface. Consequently, this may cause unphysical results, especially for high surface potentials (>25 mV) or ion concentrations.[41,42] Therefore, the Gouy-Chapman model was later improved by the approach of Stern.[43] In this particular model, the EDL is augmented by a layer of tightly bound and fully hydrated ions adjacent to the charged surface. This so-called Stern layer leads to partial compensation of the actual surface charge before the diffuse ion cloud finally decreases the potential down to zero at further distances. The specific nature and profile of the Stern layer have been a broad field of debate, and the basic model has been discussed and optimised multiple times in the following decades.[44–47]

The situation becomes even more puzzling when soft gas/liquid or liquid/liquid interfaces with an adsorbed ionic surfactant film, instead of a solid electrode surface, are in the focus of interest.[48–50] One major complication here concerns the ionic surfactant itself. It adsorbs to the interface and thus causes the net surface charge in the first place, but at the same time, it posses mobility between bulk and surface and also within the monolayer. This implies that the distinct layers proposed in the Gouy-Chapman-Stern model somewhat blur into another. Therefore, it appears quite reasonable for an adequate adsorption model to also account for penetration of (hydrated) counterions into the layer of headgroups,[10] as sketched in the above figure. However, size restrictions due to different ion radii and solvation shells may prevent the counterions from entering the headgroup layer entirely.[51]

To conclude, the real architecture of the adsorption layer built up by ionic surfactants is far more complicated, than the simple Gibbs model would initially suggest. Electrostatics and sometimes specific interactions between the involved ions and the solvent lead to a surface layer of a certain finite depth. The distribution of the respective species in that “interphase” has been tackled by numerous authors but still cannot be considered as being solved generally and remains a promising field for future research.[52]

2.4. Mixed Surfactant Systems

Whenever the purpose of a practical application requires surfactants, this formulation very likely contains more than one surface-active species. In many cases, such mixed systems are not designed deliberately, but rather result from impurities in the commercial product. This is because the improvement of purity by intensive treatment of raw materials and crude-product does not necessarily outweigh the associated costs, albeit depending very much on the respective application. Such coarse mixtures can sometimes even outperform the purified compound. Therefore, industrial surfactant often contains unreacted raw product as well as different homologs and isomers of the main product.[25,53]

Reasons for the deliberate preparation of mixed surfactant formulations can be manifold. In some instances, different surfactants are added to serve different purposes - for example in laundry care products, where fabric softening and cleaning power (detergency) can primarily be attributed to cationic and non-ionic amphiphiles, respectively. Other products require surfactant additives to tailor the physical properties and for the maintenance of a stable formulation. Most and foremost, surfactant mixtures are prepared to improve the performance of the individual components. This is the case in many household cleaning formulations where long-chain fatty alcohols are added to the mix to enhance the efficiency of the final product.[53,54]

Such synergistic systems can show superior properties while effectively requiring less of the additive. The extent of the synergy correlates to a great degree with the nature of the involved headgroups and their ability to interact with one another. Therefore, mixtures of two non-ionic surfactants with similar hydrophobic groups reportedly show only minor cooperative effects and behave rather ideally.[55–57] This means that the ratio of the two surfactants in micelles can be sufficiently predicted from the γ vs. c dependence of the individual surfactant solutions. The same holds for the monolayer composition since both can be treated as pseudo-phases separated from the solution phase. Assuming ideal surfactant behaviour, the cmc and the respective partitioning between bulk and micelle could be easily simulated, as shown in figure 2.5.

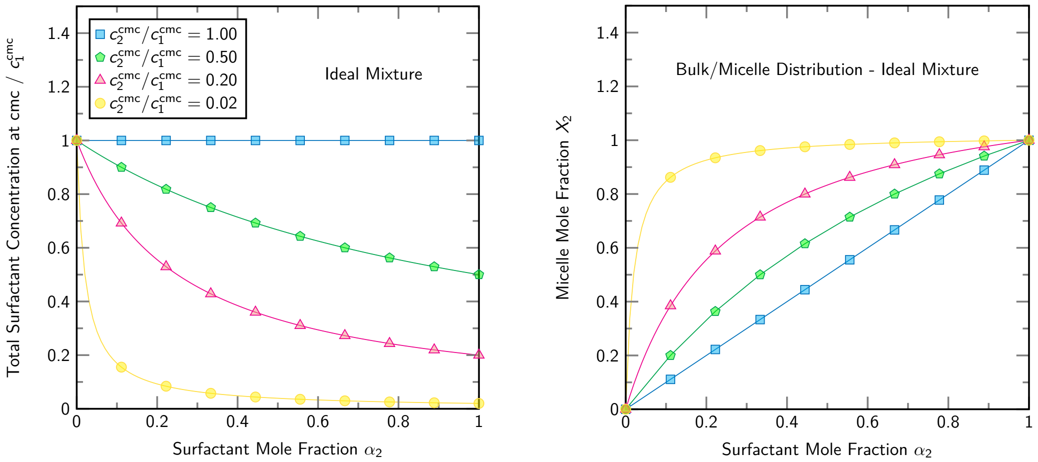

Figure 2.5.: Simulated mixing behaviour of an ideal binary mixture of surfactants 1 and 2 according to ref. [54]. Left: Total surfactant concentration at the cmc. Right: Corresponding partitioning of surfactant 2 between micelle (X_2) and bulk (α_2).

The graph not only displays the basic dependences of cmc and micelle composition in a mixed system but also illustrates the importance of purification for surfactant science, in contrast to commercial applications where only the final result, e.g. the cleaning efficiency, matters. As shown above, the presence of only minor amounts of surface-active impurities might become an issue if they exhibit a substantially higher surface affinity than the actual compound of interest. As a consequence, these impurities tend to enrich in micelles as well as in the adsorption monolayer, even if the respective combination is free of any synergistic effect.

However, if some sort of synergistic interaction between the involved surfactant species is present, it manifests as preferential mixing in micelles and monolayer. This implies that the total required amount of surfactant to achieve a given surface pressure or the cmc, respectively, is reduced with respect to the ideal system. Furthermore, the pseudo-phase composition tends towards the inclusion of both species. As a rule-of-thumb, the synergism can be expected to increase with the charge difference between the involved headgroups.[58]

For the quantification of the non-ideality of a surfactant mixture Rubingh and Rosen[59–61] developed a model based on the regular solution theory. Therein, a new dimensionless parameter β is introduced to capture the interaction W_{xy} between the surfactant species 1 and 2, which allows accounting for activity deviations in the pseudo phases.

$$\beta = \frac{N_A \left(W_{11} + W_{22} + 2W_{12}\right)}{RT} \tag{2.12}$$

For vanishing net interaction (β=0) the mixture behaves ideally as discussed above. Negative values of β correspond to a synergistic surfactant combination, whereas a net repulsion between the two species is found for $\beta > 0$. Latter case is rather rare but has been observed for mixtures involving fluorinated surfactants.[62] To demonstrate the implications of surfactant interactions on the mixture, simulations of a binary system with different cmc's and a number of β-values are given in figure 2.6. Due to the severe effect of a negative β on the cmc, logarithmic scaling was chosen for the ordinate in the left plot to properly display all calculated curves.

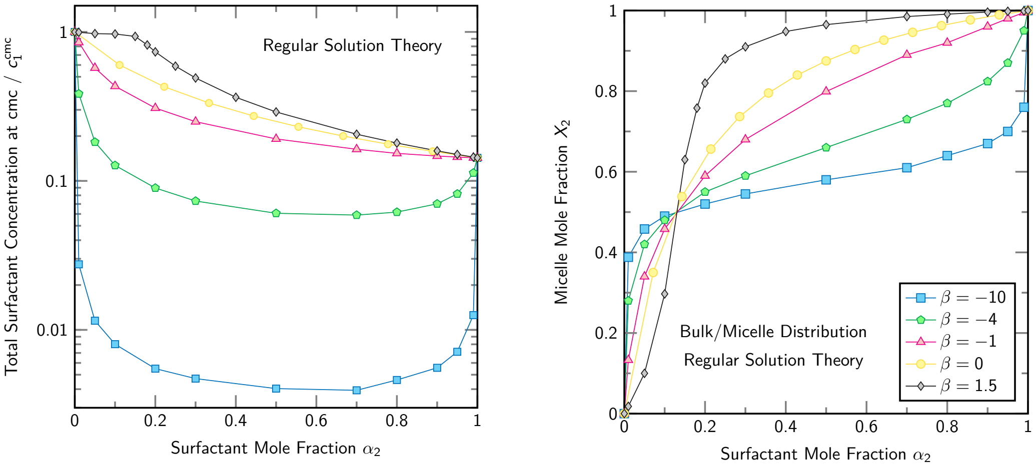

Figure 2.6.: Simulation of the mixing behaviour of surfactants 1 and 2 with the regular solution model. Calculations were conducted according to refs. [54] and [62]. Left: Total surfactant concentration at the cmc. Right: Corresponding partitioning of surfactant 2 between micelle (X_2) and bulk (α_2).

A medium extent of attractive interactions (-4 $< \beta <$ 0) has been reported for many mixtures, if a non-ionic species is added to a solution of ionic surfactant.[63–66] The driving force behind the synergism is believed to be the mitigation of electrostatic repulsive forces by the integration of uncharged headgroups into the aggregated structures. Thus, the centres of charge, i.e. the ionic headgroups, are further separated from another which is energetically more favourable. Besides that, the ionic/non-ionic mixture may also benefit from net attractive ion-dipole interactions and possibly hydrogen bonding.[59]

By far the most significant synergistic effect has been reported for mixtures of oppositely charged ionic surfactants.[12,58,67–70] The physicochemical properties of these kinds of mixtures are so extraordinary, that special designations have been established for them: “ion pair amphiphile” (IPA) or “catanionic surfactant/mixture”.[71] Note that in the most stringent sense, the latter term refers to any mixture of two oppositely charged surfactant species, whereas IPA should only be used for stoichiometrically mixed systems, whose counterions have been completely removed.

Due to the electrostatic attraction between the respective headgroups, catanionic mixtures behave vastly different than their parent compounds in terms of surface activity, aggregation behaviour and solubility. To achieve the same effect, concerning the interfacial tension and the threshold for aggregation, catanionic mixtures usually require orders of magnitude less amount than the respective surfactants alone. Depending on the actual combination of surfactants and their ratio, intermolecular interactions might even be so strong, that combined solutions precipitate at concentrations below the critical aggregation concentration (cac).[72] The term cac, instead of cmc, has been deliberately used here. It is a well-known fact, that catanionic mixtures can spontaneously form vesicular aggregates and a variety of other meso-scaled structures, which can be tailored via the composition in solution.[58,73] Certain practical applications take advantage of that, for instance in pharmaceutics, where catanionic vesicles can act as capsules for drug delivery purposes.[74]

Since in the regular solution model the presence of solvent and dissociation is not accounted for, its applicability on ionic surfactant mixtures is at least questionable.[25,75–77] For such mixtures, methods which do not depend on an oversimplified model appear to be more appropriate. An approach reported by Aratono et al.[78,79] allows retrieving the monolayer and micellar compositions from direct measurement of the surface tension. That particular approach will be discussed and applied later on in this work for the analysis of mixtures of anionic and cationic surfactants.

3. Experimental Techniques

3.1. Vibrational Sum-Frequency Generation Spectroscopy

3.1.1. Scientific Background

When an electromagnetic wave propagates through matter, it induces an oscillating dipole in the molecules of the respective medium. This is due to the displacement of the electron cloud by the external electric field. The sum of all dipole moments per unit volume is described by the bulk polarisation $\vec{P}$. For weak electrical fields $\vec{E}$ this quantity obeys a linear relationship.[80]

$$\vec{P} = \epsilon_0 \chi^{(1)} \vec{E} \tag{3.1}$$

Here, ϵ_0 refers to the vacuum permittivity and $\chi^{(1)}$ to the macroscopic linear susceptibility. Consequently, the induced dipoles adopt the oscillation frequency of the incident wave and, in turn, act as an emitting source of light with that particular wavelength. For higher field strengths the linear approximation is no longer valid, and higher-order terms have to be taken into account via a series expansion.

$$\vec{P} = \epsilon_0 \left(\chi^{(1)} \vec{E} + \chi^{(2)} \vec{E}^2 + \chi^{(3)} \vec{E}^3 + ... \right) = \vec{P}^{(1)} + \vec{P}^{(2)} + \vec{P}^{(3)} + ... \tag{3.2}$$

The tensors $\chi^{(2)}$ and $\chi^{(3)}$ are the higher-order, non-linear susceptibilities. Since they are considerably smaller than the first-order susceptibility, non-linear effects require high electrical fields, comparable to the field between electrons and nuclei within a molecule. An oscillating electric field can be expressed as a function of amplitude $\vec{E}_1$, time t and angular frequency ω.

$$\vec{E} = \vec{E}_1 \cos(\omega t) \tag{3.3}$$

According to equation 3.2 such an incident wave induces a polarisation of the form:

$$\vec{P} = \epsilon_0 \left(\chi^{(1)} \vec{E}_1 \cos(\omega t) + \chi^{(2)} \vec{E}_1^2 \cos^2(\omega t) + \chi^{(3)} \vec{E}_1^3 \cos^3(\omega t) + ... \right) \tag{3.4}$$

, which can be rewritten using trigonometric formulas:

$$\begin{aligned} \vec{P} = \epsilon_0 \chi^{(1)} \vec{E}_1 \cos(\omega t) + \frac{\epsilon_0}{2} \chi^{(2)} \vec{E}_1^2 \left(1 + \cos(2\omega t)\right) \\ + \frac{\epsilon_0}{4} \chi^{(3)} \vec{E}_1^3 (3 \cos(\omega t) + \cos(3\omega t)) + ... \end{aligned} \tag{3.5}$$

This representation reveals that the non-linear terms are responsible for the emission of light with an integral multiple of the incident frequency. This process is referred to as second, third, etc., harmonic generation. In the special case of two incident waves with wavelengths ω_1 and ω_2, the resulting field can be written as:

$$\vec{E} = \vec{E}_1 \cos(\omega_1 t) + \vec{E}_2 \cos(\omega_2 t) \tag{3.6}$$

For this constellation the first non-linear term of $\vec{P}$ is given by:

$$\begin{aligned} \vec{P}^{(2)} &= \epsilon_0 \chi^{(2)} \left(\vec{E}_1 \cos(\omega_1 t) + \vec{E}_2 \cos(\omega_2 t) \right)^2 \\ &= \epsilon_0 \chi^{(2)} (\vec{E}_1^2 + \vec{E}_2^2 \\ &\qquad + \vec{E}_1^2 \cos(2\omega_1 t) + E_2^2 \cos(2\omega_2 t) \\ &\qquad + \frac{1}{2} \vec{E}_1 \vec{E}_2 \cos((\omega_1 - \omega_2) \cdot t) \\ &\qquad + \frac{1}{2} \vec{E}_1 \vec{E}_2 \cos((\omega_1 + \omega_2) \cdot t)) \end{aligned} \tag{3.7}$$

The terms in brackets (from top to bottom) correspond to the phenomena of optical rectification (a DC field without any time dependence), second-harmonic generation (SHG), difference-frequency generation (DFG) and sum-frequency generation (SFG). The latter process is sketched in figures 3.1 and 3.4.

In a typical SFG experiment the electromagnetic fields of a visible ($\vec{E}_{\mathrm{VIS}}$) and an infra-red beam ($\vec{E}_{\mathrm{IR}}$) are spatially and temporally overlapped at a sample, resulting in the generation of a third beam, whose frequency is determined by the law of energy conservation ($\omega_{\mathrm{SFG}} = \omega_{\mathrm{VIS}} + \omega_{\mathrm{IR}}$).

During that process, momentum parallel to the surface is also conserved (cf. figure 3.2), which implies that the angle of the emitted SFG signal (β) is determined by the angles and the wave vectors (β_i and k_i) of the two incident beams.

$$k_{\mathrm{SFG}} \sin(\beta) = k_{\mathrm{VIS}} \sin(\beta_1) + k_{\mathrm{IR}} \sin(\beta_2) \tag{3.8}$$

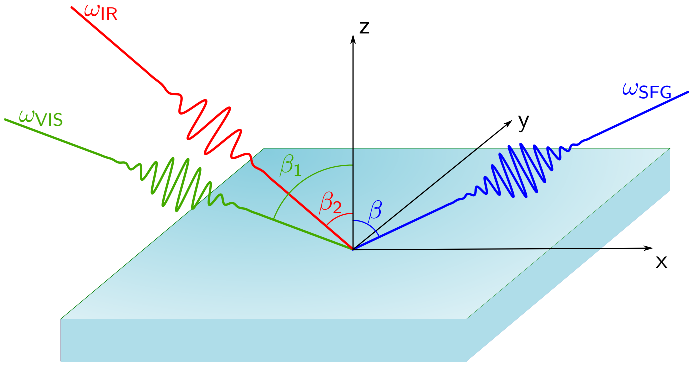

Figure 3.1.: Schematic drawing of the SFG experiment. Two co-propagating beams, one in the visible (ω_{VIS}) and the other in the infra-red regime (ω_{IR}), are temporally and spatially overlapped at an interface (equal to the xy-plane) with incident angles β_1 and β_2 relative to the surface normal z. Among others, a signal at the sum-frequency (ω_{SFG}) is generated as a result. To maintain clarity only the relevant beams are shown.

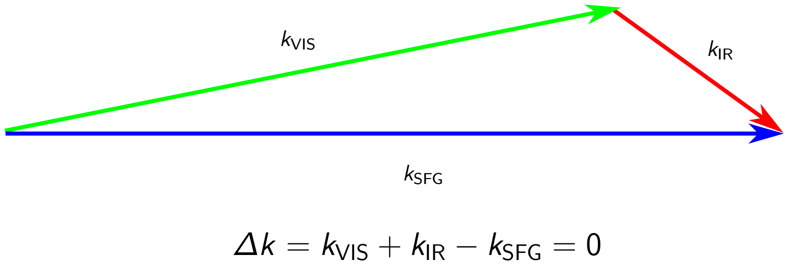

Figure 3.2.: Conservation of momentum and phase matching in the SFG-experiment. k_i refers to the wave vector of the respective beam.

At the sample-surface, the induced non-linear polarisation is given by:

$$\vec{P}^{(2)} = \chi^{(2)} \vec{E}_{\mathrm{VIS}} \vec{E}_{\mathrm{IR}} \tag{3.9}$$

Upon inversion of the incident fields' respective signs, the induced polarisation must change its sign as well. Contrarily, in media with inversion symmetry $\chi^{(2)}$ maintains its sign, which yields:

$$-\vec{P}^{(2)} = \chi^{(2)}(-\vec{E}_{\mathrm{VIS}})(-\vec{E}_{\mathrm{IR}}) \tag{3.10}$$

This implies, that SFG is a forbidden process in centrosymmetric media, since equation 3.9 and 3.10 can not be fulfilled simultaneously, unless $\chi^{(2)}$ equals zero.[81] At interfaces, inversion symmetry is inherently broken, which gives rise to a non-zero second-order susceptibility. These simple considerations reveal the unique potential of this technique, i.e. its ability to specifically probe an interface without contributions from the bulk media. The intensity of light generated by SFG is related to the parent beams according to the following manner:

$$I_{\mathrm{SFG}} \sim |\vec{P}^{(2)}_{\mathrm{SFG}}|^2 \sim |\chi^{(2)}_{\mathrm{eff}}|^2 I_{\mathrm{VIS}} I_{\mathrm{IR}} \tag{3.11}$$

$$\chi^{(2)}_{\mathrm{eff}} = \chi^{(2)}_{\mathrm{R}} + \chi^{(2)}_{\mathrm{NR}} \tag{3.12}$$

The term $\chi^{(2)}_{\mathrm{eff}}$ is the effective second-order non-linear susceptibility tensor of the interface. It contains all the measurable information on the response of the investigated system to the incident optical fields at the sum frequency.[82,83] $\chi^{(2)}_{\mathrm{R}}$ and $\chi^{(2)}_{\mathrm{NR}}$ refer to the resonant and non-resonant contributions to $\chi^{(2)}_{\mathrm{eff}}$. If the IR frequency is far from any resonant frequency of the sample, only the frequency-independent $\chi^{(2)}_{\mathrm{NR}}$-term will contribute to the generation of SFG light. Contrarily, when the IR beam can excite a vibrational transition q, the SFG response will be significantly enhanced. The corresponding amplitude is dependant on the orientally averaged hyperpolarizability $\langle\beta_q\rangle$ and the number N of SFG-active sites,[84] according to

$$\chi^{(2)}_{\mathrm{R,q}} = \frac{N}{\epsilon_0}\langle\beta_q\rangle \tag{3.13}$$

Considering equation 3.11, this implies a direct proportionality between the measured SFG intensity and N^2. Due to its sensitivity towards molecular orientation, SFG does not only provide a vibrational fingerprint of an interface, but it also allows one to study the interfacial arrangement of molecules and functional groups in great detail. To do so, the macroscopic susceptibility $\chi^{(2)}_{ijk}$ in the surface coordinate system x, y, z must be related to the molecular hyperpolarizability β_{lmn}.[85] The indices l, m, n represent the molecular inertial coordinates a, b, c and can be transformed into i, j, k via a rotation formalism by Euler, as sketched in figure 3.3.

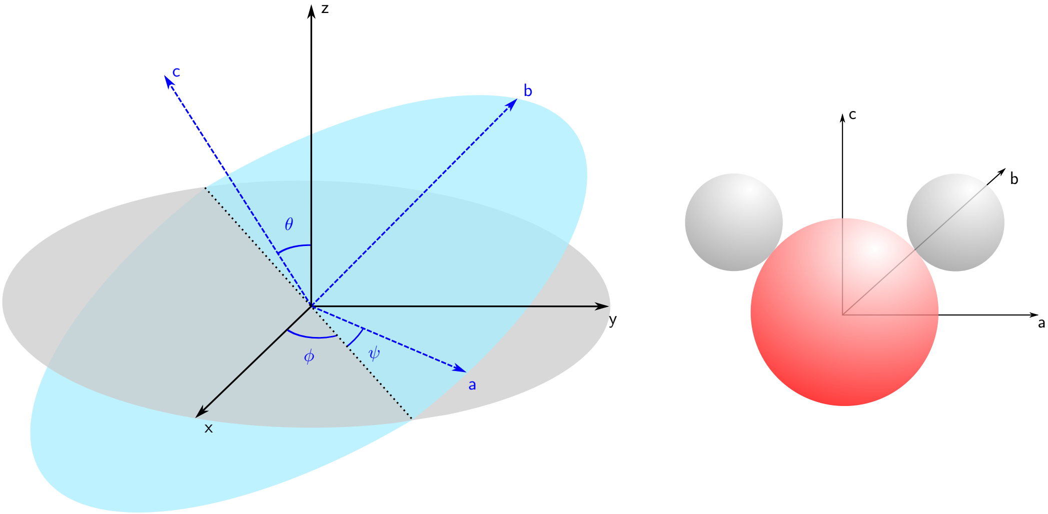

Figure 3.3.: Left: Schematic description of the coordinate transformation using Euler angles θ, ϕ, ψ to express the relationship between the surface coordinates x, y, z and the molecular coordinate system a, b, c. Right: Water molecule in inertial coordinate frame.

For a particular vibrational mode q the corresponding hyperpolarizability β_{lmn} is given by:[86]

$$\beta_{lmn,q} = \frac{\langle g|\alpha_{lm,q}|v\rangle\langle v|\mu_{n,q}|g\rangle}{\omega_{\mathrm{IR}} - \omega_q + i\Gamma_q} \tag{3.14}$$

$\alpha_{lm,q}$ and $\mu_{n,q}$ represent the Raman and dipole vibrational transition elements for a certain vibrational mode q with ground state $|g\rangle$ and vibrational excited state $|v\rangle$. An energy diagram with the corresponding transitions is given in figure 3.4. Equation 3.14 contains this technique's decisive selection rule: For a vibrational mode to be visible via SFG spectroscopy, it has to be simultaneously Raman and IR active, which is not possible for probes with an inversion centre. Subsequently, only molecules with absent internal centrosymmetry contribute to the SFG light.

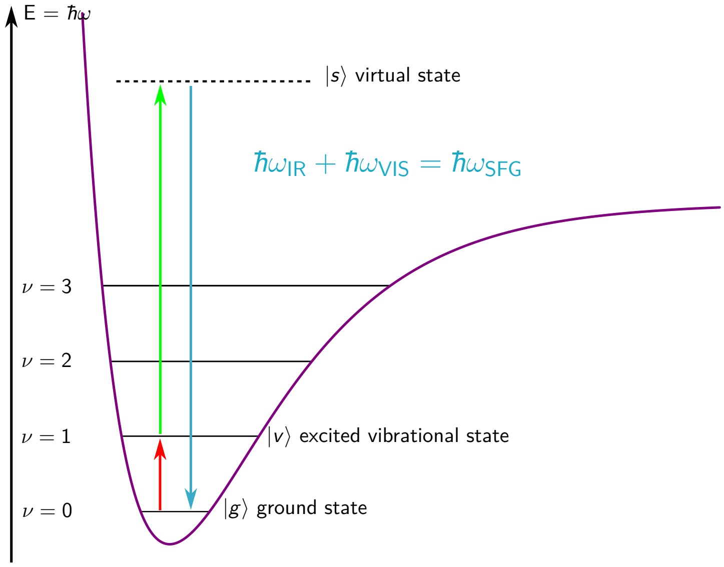

Figure 3.4.: Sketch of the energy diagram for the SFG-process. The excitation from the ground state $|g\rangle$ to the first vibrational state $|v\rangle$ is followed by an anti-Stokes-Raman process, which includes the transition to a virtual state $|s\rangle$ and the subsequent emission of a photon corresponding to the sum-frequency of the incident waves $\omega_{\text{SFG}} = \omega_{\text{IR}} + \omega_{\text{VIS}}$.

From a macroscopic point of view, the effective second-order non-linear susceptibility can be expressed with the following relation.

$$\left|\chi^{(2)}_{\text{eff}}\right|^2 = \left|\chi^{(2)}_{\text{NR}} + \sum_q \chi^{(2)}_{\text{R},q}\right|^2 = \left|\chi^{(2)}_{\text{NR}} + \sum_q \frac{A_q}{\omega_{\text{IR}} - \omega_q + i\Gamma_q}\right|^2 \tag{3.15}$$

Here A_q is the amplitude, ω_q is the center-frequency and Γ_q is the bandwidth of the resonant mode q and i is the imaginary number ($i^2 = -1$). Above equation will be used in the succeeding chapters for the deconvolution of the experimentally obtained SFG spectra.

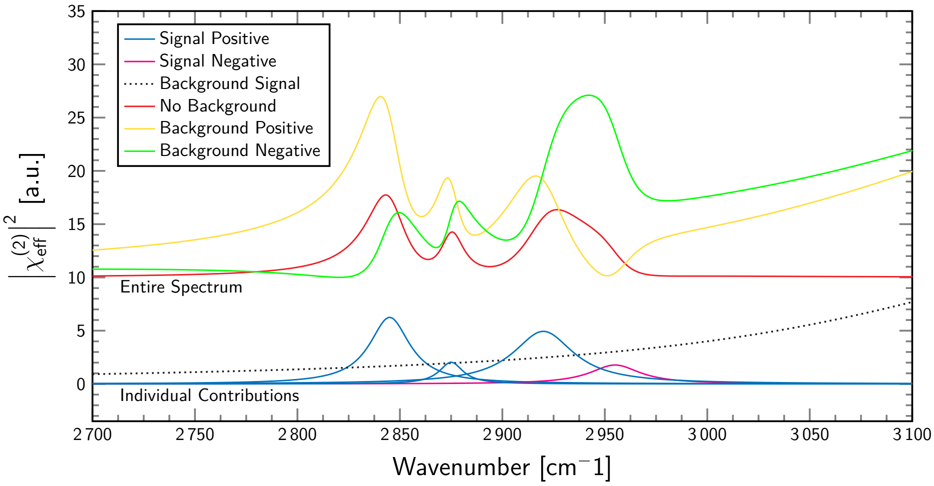

Figure 3.5.: Simulation of a typical SFG-spectrum in the region of CH-vibrations according to equation 3.15. The lower group of plots shows the individual contributions, namely signals with positive (blue) or negative (magenta) amplitude A_q and a variable background (dotted). The upper group displays the resulting spectra. The presence of background signals with equal absolute amplitude, but either positive (yellow) or negative (green) sign dramatically distorts the actual spectrum (red). As a result, observed peak wavenumbers and intensities are modified significantly.

As an example, figure 3.5 depicts three simulated SFG-Spectra in the CH-vibrational regime and the deconvolution into the individual components. The shown spectra all consist of the same set of vibrational modes. To display the implications of interference, the background signal amplitude was multiplied by factors +1, 0 and -1. With no underlying signal, the shape of the SFG-spectrum appears rather straight-forward. However, if a noteworthy background is introduced, dramatic changes in the overall profile are obtained. Not only are the peak intensities influenced heavily, but also the peak positions are shifted in one or the other direction, depending on the sign of the background amplitude.

As shown later on, this phenomenon sometimes complicates the evaluation of SFG-spectra, but can also offer additional information about the investigated systems.

It is necessary to consider that two SFG-signals may not exhibit equal peak broadening. Therefore, instead of A_q, the respective peak area $\tilde{A}_q$ is used in this work for the comparison of different signals q. Since for an isolated vibrational mode q without background signal, expression 3.15 yields a common Lorentzian line shape, $\tilde{A}_q$ is given by:

$$\tilde{A}_q = \int_{-\infty}^{+\infty} \frac{A_q^2}{(\omega_{\mathrm{IR}} - \omega_q)^2 + \Gamma_q^2} \, \mathrm{d}\omega_{\mathrm{IR}} \sim \frac{A_q^2}{\Gamma_q} \tag{3.16}$$

The second-order non-linear susceptibility $\chi^{(2)}$ is a third-rank tensor with $3^3 = 27$ elements. However, after considerations concerning the symmetry of the given experimental geometry, most of the elements vanish. For an isotropic surface, which is rotationally invariant along the z axis, only 7 non-zero elements remain:[87]

$$\chi^{(2)}_{zzz} \quad ; \quad \chi^{(2)}_{xxz} = \chi^{(2)}_{yyz} \quad ; \quad \chi^{(2)}_{xzx} = \chi^{(2)}_{yzy} \quad ; \quad \chi^{(2)}_{zxx} = \chi^{(2)}_{zyy}$$

These elements can be probed separately, by exploiting different linear polarisation combinations of the involved beams. In this context, the polarisation of an electromagnetic wave is denoted as p if the electric field vector is aligned parallel to the z-axis, and s (short for german word “senkrecht”) if it is aligned perpendicular. The element $\chi^{(2)}_{xxz} = \chi^{(2)}_{yyz}$ becomes significant for vibrations, which have an IR transition dipole oriented in z-direction. It can be accessed experimentally by combining an s-polarised SFG-beam, an s-polarised VIS beam and a p-polarised IR beam, in the following referred to as *ssp*-configuration. Accordingly, vibrations with transition modes parallel to the surface can be probed via *sps* configuration due to the non-zero element $\chi^{(2)}_{xzx} = \chi^{(2)}_{yzy}$. Therefore, by comparing SFG intensities obtained under different polarisation combinations, it is possible to get at least semi-quantitative information about the orientation of certain SFG-active molecular sites.

3.1.2. SFG Instrumentation and Experimental Procedure

A sketch of the general setup of the SFG spectrometer (EKSPLA, Vilnius, Lithuania) is given in figure 3.6. The entire set-up, described in this section is mounted on an optical table (Model RS4000TM, NEWPORT, Irvine, USA) which is located in a room tempered to 22 °C.

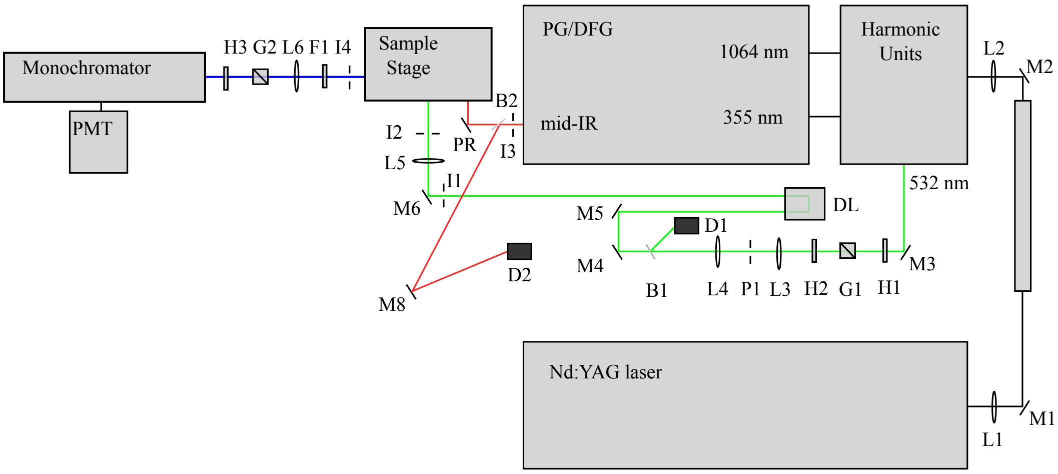

Figure 3.6.: Schematic description of the SFG-setup. L: lens; M: mirror; G: glan prism, H: half-wave plate; D: photodiode; B: beam splitter; P: pinhole; PMT: photomultiplier tube; PR: polarisation rotator; DL: delay line

A pulsed Nd:YAG-Laser (Model PL2143) with a wavelength of 1064 nm, a pulse width of ≃ 20 ps and a repetition rate of 10 Hz serves as light source. This fundamental beam is frequency-doubled in the harmonic unit by the generation of the second harmonic with a KH_2PO_4-crystal (532 nm) and is split up in two separate beams afterwards by a beam splitter. One proportion of the beam is sent through a delay line, is being linear polarized via the aid of a Glan prism and is focussed onto the sampling stage. The other proportion passes another frequency-doubling crystal to generate the third harmonic with a wavelength of 355 nm. In the parametric generator PG401/DFG this beam is again split up and is passed through a crystal of $\mathrm{LiB_3O_5}$. Thus, two new beams (idler and signal) are generated, whose wavelengths are dependant on the temperature (which is fixed in the present case) and the angle of incidence between light and crystal. By rotating the crystal the output wavelength can be tuned to the desired value. This process is referred to as optical parametric generation (OPG). Its working principle is sketched in figure 3.7.

The newly generated signal beam is blocked and the idler, exhibiting a significantly broadened frequency distribution, is narrowed down by the use of a diffraction grating. After that, the beam is once again passed through the lithium borate crystal, where it overlaps with the second proportion of the 355 nm beam. This results in an amplification of the narrow-band signal. During that process, an additional signal at the difference frequency is emitted. The corresponding process is called optical parametric amplification (OPA) or difference frequency generation (DFG), respectively (cf. figure 3.7). This set-up can generate tunable light in the visible/ultra-violet regime. To obtain a beam in the mid-infra-red region, the tunable beam is met with light of the fundamental beam (1064 nm) in a silver gallium sulfide $\mathrm{AgGaS_2}$ crystal to undergo DFG, finally yielding the desired result.

The tunable IR-beam runs through a polariser and is then directed to the sampling stage by a series of mirrors. At the surface of interest, the beam is temporally and spatially overlapped with the visible beam (532 nm) to give rise

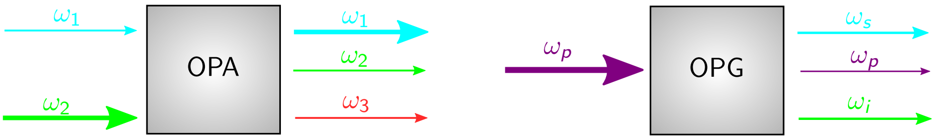

Figure 3.7.: Schematic drawing optical parameter amplification (OPA) and optical parameter generation (OPG) with a non-linear crystal. The arrow heads correspond to the respective intensity. Left: A low intensity beam ω_1 overlaps with a second beam (ω_2) under phase matching conditions. Thus, beam 1 experiences an amplification, while a third, less intense beam (ω_3) is emitted. Right: A pump beam ω_p generates two new beams (ω_i and ω_s).

to a new signal at the sum-frequency of the two incident beams. The intensities of the mid-IR (I_{IR}) and the visible beam (I_{VIS}) are continuously monitored via two photo-diodes to account for fluctuations in the beam intensities. This is required since the output intensity is proportional to both input intensities (cf. equation 3.11). Subsequently, the reflected incident beams are blocked and the signal at the sum-frequency is directed to the detection unit. A notch filter helps to remove all residual interfering signals. After being linear-polarized by another Glan prism, the beam enters the detection unit, where it is filtered by a monochromator (Model SP-2150i, PRINCETON INSTRUMENTS, Trenton, USA) and analysed with a photomultiplier tube (Model R7899, HAMAMATSU, Herrsching, Germany).

Samples were measured in a flat Teflon vessel which was slowly rotated throughout the entire duration of the measurement via a rotating plate. This ensures that every laser pulse hits a new spot and prevents local heating of the sample. All sample vessels and other glassware used in the context of SFG-measurements were soaked for several hours in a 3:1 (v/v) mixture of sulfuric acid and hydrogen peroxide (Caro's acid) to remove all organic contaminations. Afterwards, the oxidising solution was washed-off by heavy rinsing with Millipore water.

To obtain smooth curves, each data point in the SFG-spectrum was collected by averaging of at least 50, but sometimes even up to 200 individual measurements. Thus, the acquisition time of a single spectrum could take 30 min to one hour, depending on the spectral regime investigated. Adjustment of the set-up was required to change the polarisation of the involved laser beams. This could lead to subtle variations in the detected absolute SFG-intensity due to non-optimal positioning of the involved optical components. In the following, spectra will therefore be only compared directly, if taken with the very same adjustment.

3.2. Methods for Determining Interfacial Tension

3.2.1. Pull-Force Methods

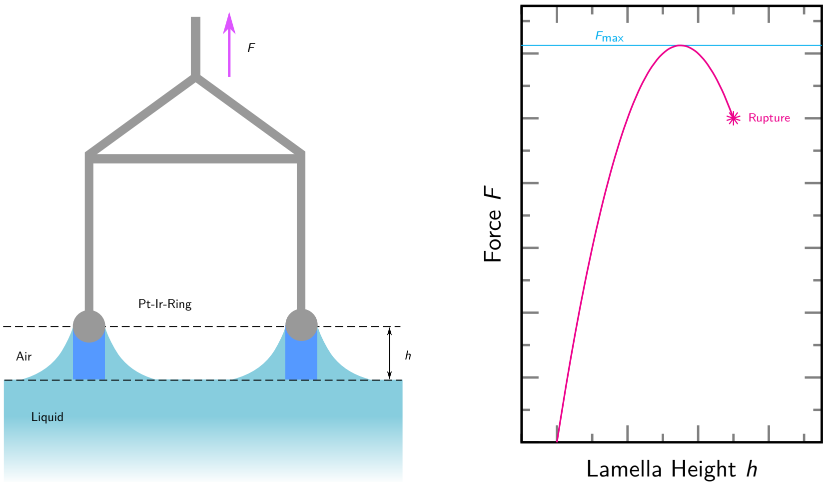

Figure 3.8.: Left: Cross-sectional representation of the Du Noüy Ring method for determining interfacial tension. A Pt/Ir-alloy ring is slowly pulled out of the liquid sample. An equipped balance measures the force corresponding to the volume of the water column between the ring and the flat liquid surface (shaded area). Right: The actual surface tension can be calculated from the global maximum of the force-against-height plot $F(h)$.

Common methods to determine the interfacial tension of a liquid are the so-called pull-force methods.[88] The first example of this family is the Du Noüy ring method,[89] sketched in figure 3.8. For this technique, a wire ring with radius R, usually composed of a noble metal alloy like Pt/Ir, is used. It is first immersed in a liquid sample and is then slowly pulled upwards. Simultaneously, an equipped balance measures the sum of forces acting on the ring. Upon crossing the flat liquid surface a small lamella forms below the ring, which exerts an additional force. The maximum force F_{max} is established when the lamella is aligned perpendicular to the ring plane. In a first-order approximation ($f = 1$) that maximum correlates with the interfacial tension according to the following relation.

$$\gamma = \frac{F_{\mathrm{max}}}{4R\pi f} \tag{3.17}$$

For extremely precise measurements a semi-empirical correction term f has to be introduced to account for the contact angle and the differences in the inner and outer perimeter of the ring. It has also to be noticed, that this method is only a quasi-static method since it requires a net movement of the ring. Therefore, in order to get accurate results, the adsorption equilibrium has to be established within the time frame of the set-up's movement.

Another widely used example of a pull-force method is the Wilhelmy technique,[90,91] which is sketched in figure 3.9. Instead of a ring-shaped wire, this method probes the surface tension by immersing a thin plate into the sample solution and measuring of the exerted force. Suitable materials for the plate can be manifold as long as they provide good wetting properties, e.g. platinum, glass or paper. Adsorption of surfactant molecules onto the plate may render the wetting properties. For that reason, this technique fails for

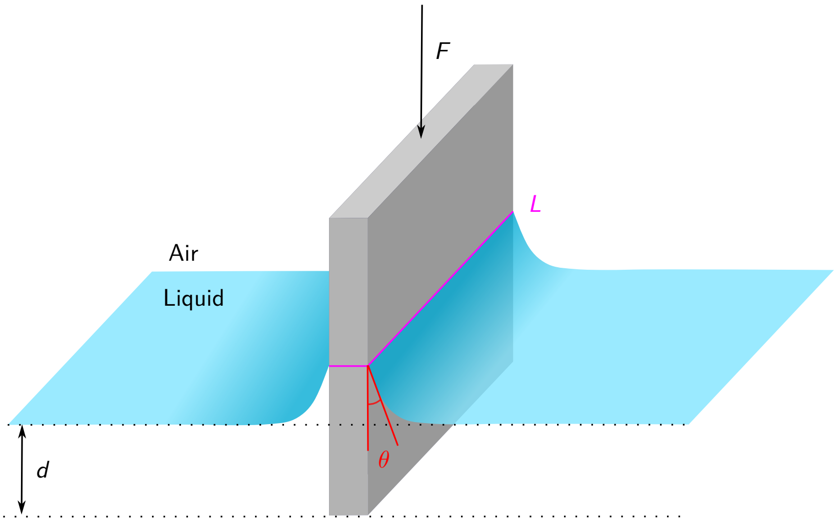

Figure 3.9.: Schematic representation of the Wilhelmy plate measuring geometry. A plate with a three-phase contact angle θ is immersed in in a liquid sample by a depth d. In addition to the gravitational force and buoyancy a pulling force F acts on the set-up, which is given by the length of the contact line L and the surface tension γ of the liquid interface.

special combinations of plate material and sample, e.g. a metal plate plus a cationic surfactant solution. Using the static technique, the surface tension can be calculated via the following relation.

$$\gamma = \frac{F}{L \cdot \cos(\theta)} \tag{3.18}$$

Here, F refers to the total force acting on the plate minus the gravitational force and buoyancy, L is the length of the air/liquid contact line and θ is the contact angle.

Among other techniques, the Wilhelmy plate, and the Du Noüy ring method, can be applied with the K100 Tensiometer (KRÜSS, Hamburg, Germany), which was also used in the framework of this thesis. This device is equipped with a thermostat to enable temperature control. In this work, all samples were measured at 25 °C. Additionally, a dosing unit by Metrohm

(Herisau, Switzerland) allows fully automated measurement of the surface tension as a function of the surfactant concentration. The used glassware was cleaned by soaking in a basic solution of isopropanol and heavy rinsing with Millipore water. The metal plate or the wire frame were heated via the flame of a bunsen burner to remove organic contaminants. All dilution series were conducted by pouring 40 mL of the sample stock solution in the measuring cell and starting of the automated modus after allowing the temperature to equilibrate for a few minutes. Since the measuring procedure takes several minutes to record a number of datapoints (5-10) for each dilution step, surface tension can be expected to be close to the equilibrium value.

3.2.2. Profile Analysis Tensiometry

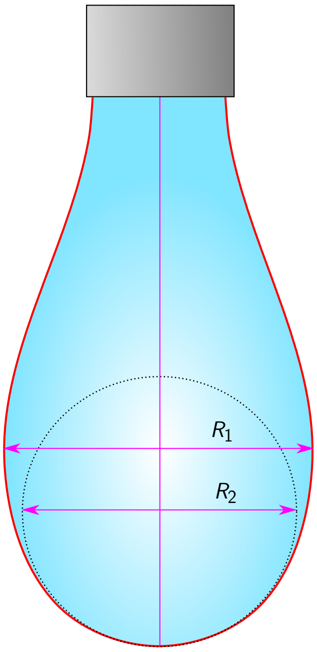

Figure 3.10.: Schematic representation of the pendant drop measuring geometry. The axis symmetric shape of the drop (red), defined by the radii of curvature R_1 and R_2, results from competing forces of curvature and gravity.

An elegant way to determine the surface tension of a liquid is axis-symmetric drop shape analysis. A detailed description of the method can be found in the literature.[92] In the framework of this thesis, a PAT-1M tensiometer (SINTERFACE Technologies, Berlin, Germany) was used, which utilises the pendant-drop technique. This method provides surface tension values according to the Young-Laplace equation:

$$\gamma(R_1^{-1} + R_2^{-1}) = \Delta P_0 + \Delta\rho g h_v \tag{3.19}$$

, where γ represents the equilibrium surface tension, R_1 and R_2 the respective radii of curvature, ΔP_0 the pressure difference in a reference plane, $\Delta\rho$ the difference in mass density of air and aqueous phase, g the gravitational acceleration and h_v the vertical height from the reference plane. A scheme of the measuring geometry is given in figure 3.10. A camera captures images of the hanging drop which are analysed by an algorithm for contour tracing. The computer software is employing polar coordinates to fit the Young-Laplace equation using γ as a fit-parameter to obtain a curve corresponding to the experimentally determined shape of the drop meniscus. An equipped thermostat allows adjustment of the temperature. Drop volume is controlled by a syringe pump connected to a stainless steel capillary of 1-3 mm in diameter. This technique requires only small amounts of solution ($\simeq$ 1 mL) and is therefore suited for the investigation of expensive or weakly surface-active compounds. Furthermore, it can determine the surface tension as a function of time, as long as the drop exhibits a Laplacian shape. Thus, the ageing of a liquid surface can be investigated, which offers information about the adsorption process. Due to uncertainties in the dead-time for drop formation and non-Laplacian deformation, the time resolution of these experiments is limited to seconds.

By computer-controlled sinusoidal oscillation of the drop, this set-up is also able to measure the dilatational rheology of adsorption layers for oscillation frequencies smaller than $\simeq 1\,\mathrm{Hz}$.

To avoid the influence of evaporation effects, drops were monitored for no longer than ten minutes when determining the surface tension equilibrium value. This duration was sufficient for most of the studied solutions to maintain a stable value ($\pm\ 0.1\,\mathrm{mN\,m^{-1}}$) over one minute, which was regarded as the criterion for equilibrium in this work.

3.3. Further Methods

3.3.1. Foam Analysis

Shaking a sealed, sample-filled vessel mechanically and monitor the foam decay visually is a method that certainly works for a rough characterisation of foam systems. However, that technique lacks reproducibility when it comes to the determination of foamability and foam stability. Foams are rather complex systems whose properties depend on a variety of different system variables. In order to characterise foam networks, and even compare them to others, as many parameters as possible have to be kept constant during and between the measurements. Therefore the foam-analyser DFA100 (KRÜSS, Hamburg, Germany) was used in the framework of this thesis.

To prepare a reproducible foam network, a defined volume of sample liquid is poured into the column-shaped glass vessel of the device. Upon starting the experiment, a certain amount of air is pumped through the porous glass frit at the bottom of the column. Computer software precisely controls the process of foam formation and monitors the foam evolution as a function of time. For

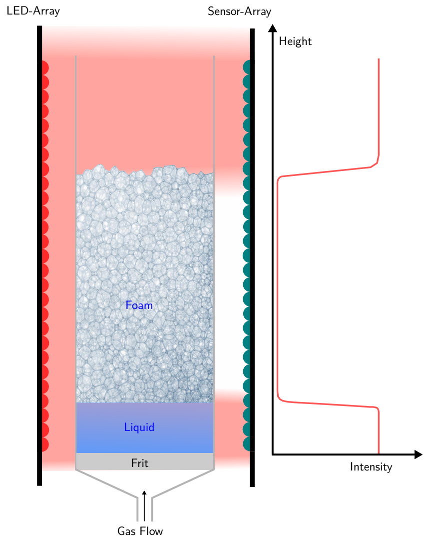

Figure 3.11.: Left: Schematic representation of the foam analysing set-up. Right: The foam height is determined by an abrupt change in the detected light intensity due to the diffuse scattering by the foam column.

the determination of the foam's boundaries to the gaseous and liquid phase, the device takes advantage of the scattering of light within a foam network, as sketched in figure 3.11. All measurements were conducted in a tempered room at 22 °C.

3.3.2. Dynamic Light Scattering

Dynamic light scattering (DLS) is a method which measures the light scattered by dispersed particles or aggregates in solution. The latter are subjected to Brownian motion, which causes fluctuations in the detected light intensity. The time-frame of these variations correlates with the speed of the scatter-centres in the sample. Thus, the hydrodynamic radius can be obtained from DLS via the aid of the Stokes-Einstein relation. Note that this approach assumes spherical particles, which might not always be the case in reality.

Dynamic light scattering measurements were performed at 25° using a CGS-

3 goniometer system from ALV. It consists of an ALV-7004/FAST Multiple Tau digital correlator and a vertical-polarized 22 mW HeNe laser with a wavelength of 632 nm. The solutions were filtered with a PTFE filter before transferring approximately 3.5 mL of the sample into cylindrical light scattering tubes with 10 mm outer diameter. The latter was cleaned and placed in a toluene bath, serving to control the temperature. Each sample was measured for 5 min with the laser set to an angle of 90° relative to the detector.

4. Results

4.1. Bolaamphiphiles and their Mixtures with Conventional Surfactant

4.1.1. Introduction to the System

Bolaamphiphiles, or short bolas, are a special class of surface-active substances. In contrast to conventional surfactants, these kinds of molecules bear two polar or ionic headgroups on both ends of a (linear) hydrophobic backbone, which is why they are also referred to as edge amphiphiles.[93,94] Due to the second headgroup bolas are less surface-active than their one-headed counter-parts with the same number of carbon atoms in the alkyl unit.[95,96] Nevertheless, their unique molecular architecture makes them attractive for several special applications, for example as an artificial membrane building block, as disrupting agent for biological membranes or in catalysis.[97–99] In aggregated structures within the bulk phase, such as vesicles or membranes, bolas can often maintain the stretched-out, dumbbell-like shape.[100,101] However, when it comes to interfacial adsorption, an all-trans conformation of the alkyl spacer is rather unfavourable from an energetic point of view. Provided that the molecule possesses a certain degree of spatial and rotational freedom it is forced into a bent geometry at air/water or oil/water interfaces, as shown in figure 4.1.[102] Thus, the alkyl chain conformation of bolaamphiphiles in an adsorbed monolayer can be investigated via vibrational SFG-spectroscopy, as explained later on. In this section different systems containing bolaamphiphiles are discussed and compared to their conventional surfactant analogon via means of tensiometry and SFG. The same methods were also employed to study the interactions between the bolaamphiphiles and an oppositely charged surfactant and its implications for the adsorption to the air-water interface.

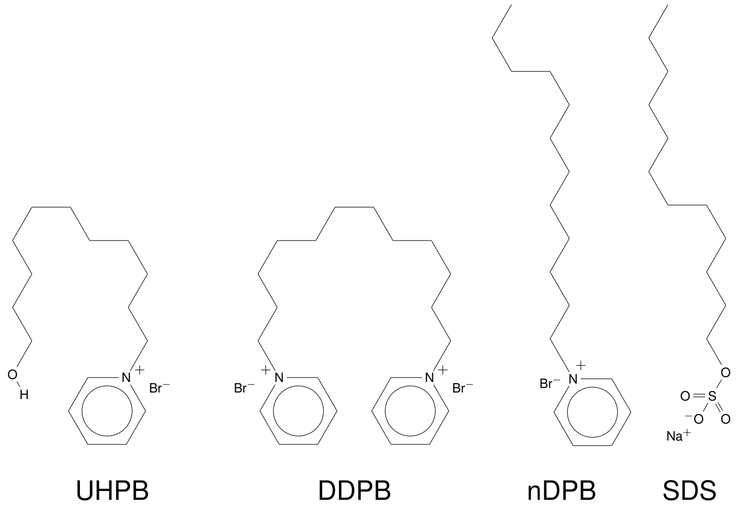

Figure 4.1.: Surfactants important for the context of this section: Undecyl-1-hydroxy-11-*N*-pyridinium bromide (UHPB), Dodecyl-1,12-bis-*N*-pridinium bromide (DDPB), n-dodecyl-1-pyridinium bromide (nDPB) and sodium dodecylsulfate (SDS). The presented structures should exemplarily illustrate possible molecular geometries in the air-water adsorption layer (bottom of the figure towards solution phase, top towards gas phase).

4.1.2. Sample Preparation

4.1.2.1. Synthesis of Pyridinium Surfactants

The pyridinium compounds nDPB, DDPB and UHPB, synthesised in the framework of this thesis, were synthesised by a substitution reaction of pyridine with the corresponding alkylbromides 1-Bromododecane, 1,12-Dibromododecane, or 1-Bromo-11-hydroxyundecane, respectively. All the synthesis followed the same route: One equivalent alkylbromide was dissolved in acetonitrile (800 wt%). An excess of pyridine (five equivalents for each bromide leaving group) was added and the solution was refluxed at 90 °C for one day. After cooling to room temperature the mixture was concentrated under vacuum until solid crystals began to form. The precipitate was filtered off, washed with diethyl ether, dried under vacuum and recrystallised twice from an acetonitrile/methanol mixture to yield the final product. Analytic data for each compound are listed below and the corresponding NMR-spectra are given in the appendix (cf. section A.1).

Dodecyl-1,12-bis-*N*-pyridiniumbromide (DDPB):

^{1}**H-NMR** (400 MHz, D_2O, δ[ppm]): 8.74 (d, $^{3}J_{H}$=5.5 Hz, 4H), 8.44 (t, $^{3}J_{H}$=7.9 Hz, 2H), 7.97 (t, $^{3}J_{H}$=7.1 Hz, 4H), 4.51 (t, $^{3}J_{H}$=7.3 Hz, 4H), 2.06-1.75 (m, 4H), 1.21-1.43 (m, 16H).

^{13}**C-NMR** (100 MHz, D_2O, δ[ppm]): 145.5, 144.2, 128.2, 62.0, 30.5, 28.6, 28.5, 28.1, 25.2.

Elemental analysis: wt% found (calculated). C: 53.5 (54.3); H: 7.0 (7.1); N: 5.4 (5.8); S: 0.0 (0.0).

Undecyl-1-hydroxy-11-*N*-pyridiniumbromide (UHPB):

^{1}**H-NMR** (400 MHz, D_2O, δ[ppm]): 8.74 (d, ^3J_H=5.7 Hz, 2H), 8.44 (t, ^3J_H=7.7 Hz, 1H), 7.96 (t, ^3J_H=7.2 Hz, 2H), 4.50 (t, ^3J_H=7.3 Hz, 2H), 3.48 (t, ^3J_H=6.6 Hz, 2H), 2.07-1.77 (m, 2H), 1.53-1.32 (m, 2H), 1.21-1.07 (m, 14H)

^{13}**C-NMR** (101 MHz, D_2O, δ[ppm]): 145.5, 144.2, 128.2, 62.0, 61.9, 31.3, 30.5 28.6, 28.5, 28.5, 28.4, 28.0, 25.1, 25.0

Elemental analysis: wt% found (calculated). C: 57.4 (58.2); H 8.3 (8.5); N: 3.9 (4.2); S: 0.0 (0.0).

***n*-Dodecyl-1-pyridiniumbromide (nDPB):**

^{1}**H-NMR** (400 MHz, D_2O, δ[ppm]): 8.91 (d, ^3J_H=5.6 Hz, 2H), 8.49 (t, ^3J_H=7.8 Hz, 1H), 8.10-7.89 (m, 2H), 4.61 (t, ^3J_H=7.4 Hz, 2H), 2.05-1.74 (m, 2H), 1.37-0.90 (m, 18H), 0.62 (t, ^3J_H=6.7 Hz, 3H).

4.1.2.2. Purification of Sodium Dodecylsulfate

Sodium dodecylsulfate (SDS) is known to undergo hydrolysis if stored in contact with water for longer periods of time. The product of this reaction dodecanol is very surface-active and has been proven to dominate the adsorption properties of SDS solutions.[103–105] For the removal of residual dodecanol, commercially available SDS (AppliChem, $>$ 99%) was recrystallised several times from ethanol. To check for successful dodecanol removal, the surface tension was measured around the cmc. If surface-active impurities are present in non-micellar surfactant solutions, they co-adsorb at the interface and lower the interfacial tension further than SDS alone. This effect is most recognisable around the cmc. At even higher concentrations, the hydrophobic impurities are rather incorporated into the core of the micelles, than in the surface film.

Thus, the surface tension gradually rises to the level of pure solution. Solutions of multiple recrystallised SDS exhibited a monotonous γ vs. c graph, which verified a satisfactory level of purity.

4.1.3. Analysis of Surface Layer with Tensiometry Data

Figure 4.2 displays the surface tension isotherms of three pyridinium surfactant systems investigated in this work. Compared to the rather conventional amphiphillic compound nDPB, the bolaform surfactants DDPB and UHPB are less surface-active. A noticeable decrease in equilibrium surface tension does not occur until the total concentration exceeds $1 \times 10^{-2}\,\mathrm{mol\,L^{-1}}$. Breakpoints in the curve, indicating the critical aggregation concentration of DDPB and UHPB, were found at 168 and $273\,\mathrm{mmol\,L^{-1}}$, respectively, which is over one order of magnitude higher than for the aforementioned n-dodecyl surfactant ($14\,\mathrm{mmol\,L^{-1}}$). Additionally, the corresponding surface tension γ_{cmc} is significantly higher (54 and $49\,\mathrm{mN\,m^{-1}}$) - nDPB, however, shows a value around $38\,\mathrm{mN\,m^{-1}}$.

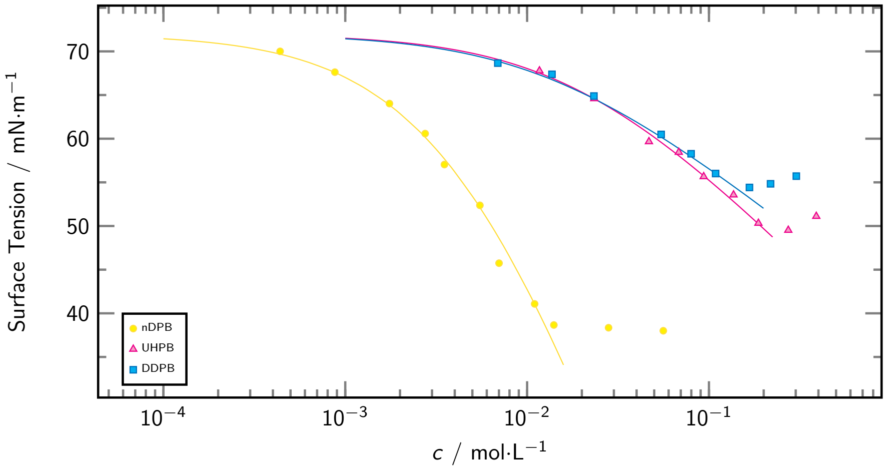

Figure 4.2.: Surface tension isotherms of aqueous solutions of nDPB, UHPB and DDPB. Data was fitted with a Frumkin-type function (solid lines).

When combining solutions of the cationic pyridinium surfactants with the anionic surfactant SDS, a dramatic increase in surface-activity is observed, which is indicative for synergistic interaction. The extent of that increase is most pronounced when cat- and anionic surfactant are present in stoichiometric amounts.[106] Catanionic mixtures benefit from the mutual cancellation of headgroup charge, resulting in a quasi-uncharged surfactant complex.[67] That strong attractive force between the oppositely charged surfactant species may also be responsible for precipitation, which was observed in the experiment for mixtures containing nDPB and UHPB. Thus, in order to get experimental curves, unaffected from concentration alteration due to precipitation, ternary mixtures of water, SDS and nDPB or UHPB, respectively, had to be diluted to a concentration below their cmc. Contrarily, catanionic mixtures of DDPB and SDS, did not show precipitation in the investigated concentration range.

In figure 4.3 surface tension isotherms of the binary mixtures of cat- and anionic surfactant are shown for different compositions. Here the abscissa refers to the concentration of SDS in the total mixture. This representation yields almost parallel curves, where a higher SDS content in the mixture apparently also produces a higher cmc, only considering SDS. The onset of micellisation is observed for all studied compositions of DDPB. Except for the heavily unsymmetrical composed mixtures, all samples show a similar γ_{cmc}. Contrarily, mixtures of SDS and UHPB precipitated before a kink in the surface tension isotherms was detectable.

Although that representation gives a good overview, the extent of the synergistic effect between the two surfactant species is not easily discernibly. This issue can be overcome by plotting the total concentration as a function of the mixture's composition. In doing so, one may only consider selected

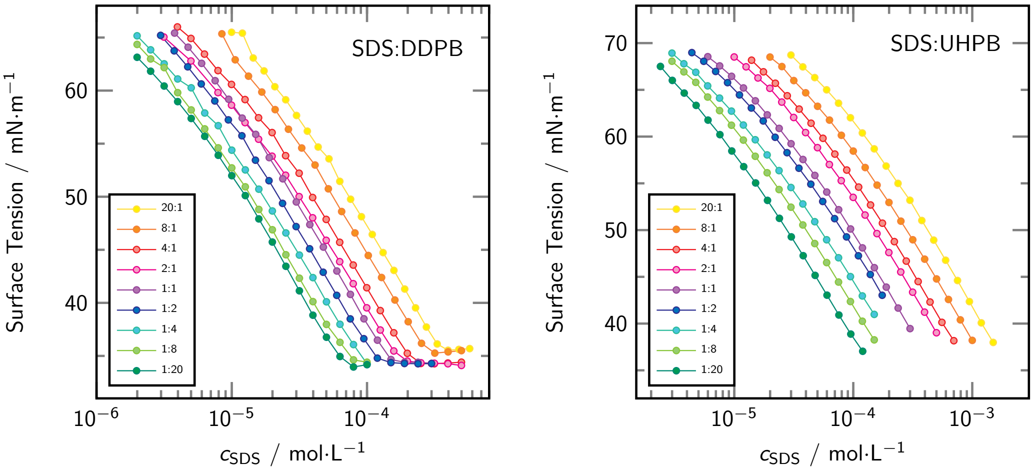

Figure 4.3.: Equilibrium surface tension isotherms of mixtures of SDS with DDPB (left) and UHPB (right) in various concentration ratios. To maintain clarity surface tension is plotted against the SDS concentration.

points on the graphs: either the cmc or the concentration at a fixed surface tension value. This kind of representation is shown in figure 4.4. Therein the composition of the binary surfactant mixture is given by the SDS proportion $\alpha_{\mathrm{SDS}} = c_{\mathrm{SDS}} \cdot (c_{\mathrm{SDS}} + c_{\mathrm{Bola}})^{-1}$.

The model of Clint (equation 4.1) relates the mixed system's cmc $c_{\mathrm{tot}}^{\mathrm{cmc}}$ to the mole fraction α_i of the binary surfactant mixture and either cmc of pure the surfactant c_i^{cmc} under the assumption of ideal mixing.[55]

$$\frac{1}{c_{\mathrm{tot}}^{\mathrm{cmc}}} = \frac{\alpha_1}{c_1^{\mathrm{cmc}}} + \frac{\alpha_2}{c_2^{\mathrm{cmc}}} \tag{4.1}$$

Analogously, concentrations yielding equal surface tension instead of $c_{\mathrm{tot}}^{\mathrm{cmc}}$ can be used to deduce the monolayer composition of an ideal mixture. Figure 4.4 shows that the presented mixed systems do not behave ideally, which again confirms the strong synergism between the two surfactant species. The curves of both, cmc and constant surface tension, exhibit a minimum in total concentration. In general, required concentrations are over one to two orders

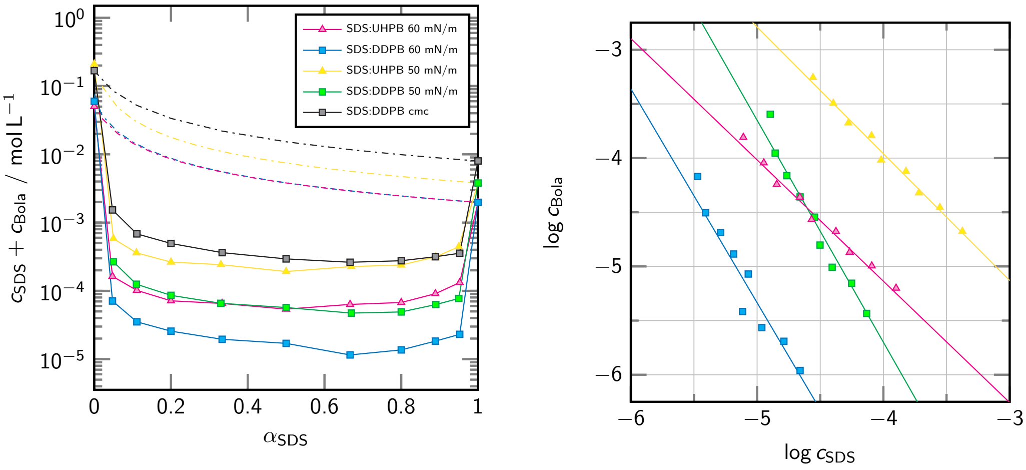

Figure 4.4.: Left: Total surfactant concentration required to yield a surface tension of 50 and 60 mN m^{-1} or the cmc, respectively, as a function of the bulk mole fraction α_{SDS}. Additionally, plots assuming ideal behaviour are given as broken lines. Right: Bi-logarithmic representation of the respective surfactant concentrations corresponding to the plots on the left.

of magnitude lower than in the ideal case for all the studied mixtures.

The composition of the interface can be analysed via the approach reported by Aratono et al.[107] for a mixture of two ionic surfactants 1 and 2, which are also strong electrolytes. In aqueous solution both compounds dissociate into their ionic components and therefore the total ion concentration $\hat{c}$ is given as:

$$\hat{c} = c_a + c_b + c_c + c_d = \nu_1 c_1 + \nu_2 c_2 \tag{4.2}$$

Indices a, b represent the surfactant ions and c, d the corresponding counterions. The stoichiometry factors ν_1, ν_2 correspond to the number of separable ions in the neutral surfactant salt molecules 1 and 2. Analogous, the total surface excess $\hat{\Gamma}$ can be expressed as sum of the individual components.

$$\hat{\Gamma} = \Gamma_a + \Gamma_b + \Gamma_c + \Gamma_d \tag{4.3}$$

The mole fraction of surfactant 2 in the monolayer $\hat{X}_2^\sigma$ and bulk $\hat{X}_2$ are given by:

$$\hat{X}_2^\sigma = \frac{\Gamma_b + \Gamma_d}{\hat{\Gamma}} \qquad \hat{X}_2 = \frac{c_b + c_d}{\hat{c}} \tag{4.4}$$

Since both, surfactant and counterion, are included in the expression for the composition, $\hat{X}_2$ may differ from the mole fraction (as used in figure 4.4) depending on the surfactant stoichiometry. Note that in the present case the electroneutrality condition, which considers the charge z_j of the respective ion j, simply reads:

$$\sum_j z_j X_j^\sigma = 0 \tag{4.5}$$

This relation implies that the surface composition can not be solved with respect to the separate ions. Therefore, the miscibility of the surfactant in the surface layer is expressed via $\hat{X}_2^\sigma$, which includes surfactant and counter-ion, according to the following relation:[78]

$$\hat{X}_2^\sigma = \hat{X}_2 - \frac{\hat{X}_2 \hat{X}_1}{\hat{c}} \left(\frac{\partial \hat{c}}{\partial \hat{X}_2} \right)_{T,p,\gamma} = \hat{X}_2 - \left(\hat{X}_2 - \hat{X}_2^2 \right) \cdot \left(\frac{\partial \ln \hat{c}}{\partial \hat{X}_2} \right)_{T,p,\gamma} \tag{4.6}$$

This means effectively, that $\hat{X}_2^\sigma$ can be obtained by plotting $\ln \hat{c}$ as a function of $\hat{X}_2$ and subsequent fitting of the data with a suitable function. Catanionic systems are reported to exhibit uniform values for $\hat{X}_2^\sigma$ within a broad window of different surfactant compositions.[79] With that in mind, a reasonable fitting function $\ln \hat{c}(\hat{X}_2)$ can be derived from equation 4.6 via the following approach.

$$\begin{aligned} \ln \hat{c}(\hat{X}_2) &= \left[\int \frac{\hat{X}_2 - \hat{X}_2^\sigma}{\hat{X}_2 - \hat{X}_2^2} \cdot d\hat{X}_2\right]_{\hat{X}_2^\sigma=\text{const.}} \\ &= (\hat{X}_2^\sigma - 1) \cdot \ln\left(1 - \hat{X}_2\right) - \hat{X}_2^\sigma \ln \hat{X}_2 + C \end{aligned} \tag{4.7}$$

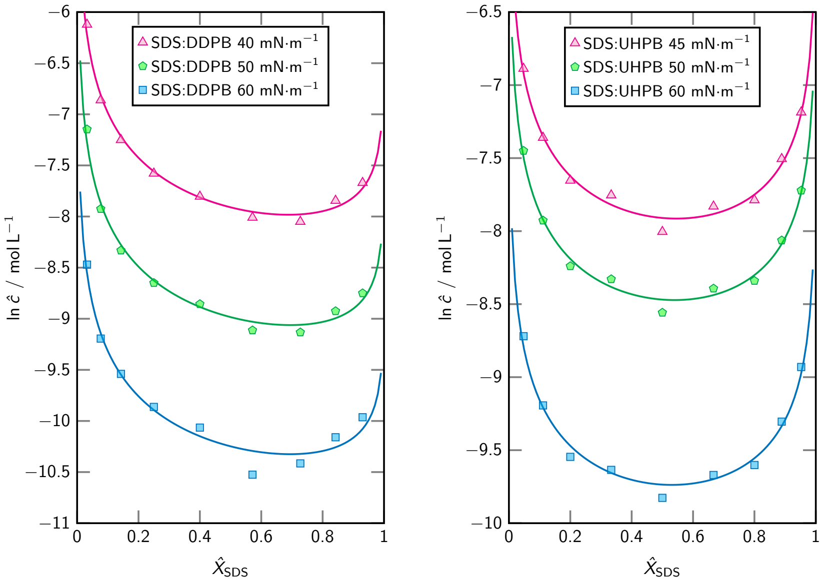

Figure 4.5.: Plot of the total ion concentration $\ln \hat{c}$ for mixed ionic surfactant systems as a function of the bulk composition expression $\hat{X}_{\text{SDS}}$ at fixed surface tension values. The solid lines represent fitting curves according to equation 4.7. Left: SDS:DDPB-mixture; Right: SDS:UHPB-mixture.

Figure 4.5 displays the corresponding curves for SDS:UHPB and SDS:DDPB mixtures. The data can be fitted to a satisfactory degree with the above equation. This implies a nearly constant surface composition for the entirety of the investigated mixtures for both systems. $\hat{X}^\sigma_{\text{SDS}}$ is found to be 0.54 ± 0.01 for SDS:UHPB mixtures and 0.69 ± 0.01 for SDS:DDPB mixtures for all the shown curves. $\hat{X}^\sigma_{\text{SDS}}$ is similar to the electroneutral stoichiometry of bola- and dodecyl sulfate ions with a slight excess of the more surface-active component SDS.

The results from the surface composition analysis agree with what can be seen in figure 4.6. It displays again the surface tension data of the catanionic mixtures SDS:UHPB, SDS:DDPB plus the results of the mixture SDS:nDPB. This time the abscissa refers to the corresponding ionic product of surfactants a and c, which for the presented 1:1- or 2:1-systems is given by:

$$c^*_{ac} = (c_a \cdot c_c)^{\frac{1}{2}} \qquad \text{or} \qquad c^*_{a2c} = (c_a^2 \cdot c_c)^{\frac{1}{3}} \tag{4.8}$$

All surface tension graphs from figure 4.3 collapse onto one single curve when plotted as a function of the surfactant-only ionic product c^*.[108] This observation also explains the linear slopes close to one or two in the double logarithmic plots of figure 4.4.[67,109] The surface tension is given by the ionic product, regardless of the mixture's composition, which effectively makes c^* a constant considering a fixed surface tension value. Therefore, taking the logarithm of both sides of equation 4.8 yields a linear relationship between the logarithms of the individual surfactant concentrations, where the negative slope equals the surfactant stoichiometry.

$$\log c_c = -{}^1\!/\!_1 \cdot \log c_a + \text{const.} \qquad \text{or} \qquad \log c_c = -{}^2\!/\!_1 \cdot \log c_a + \text{const.} \tag{4.9}$$

The dependency on the surfactant-only ionic product is based on the fact that the adsorption is almost entirely dominated by the electroneutrality of the surfactants and the influence of counterion adsorption can be neglected. With the classical Frumkin formalism the adsorption isotherm and the equation of state are described by two fundamental expressions:[110–113]

$$bc^* = \frac{\theta}{1-\theta} \exp(-2a\theta) \tag{4.10}$$

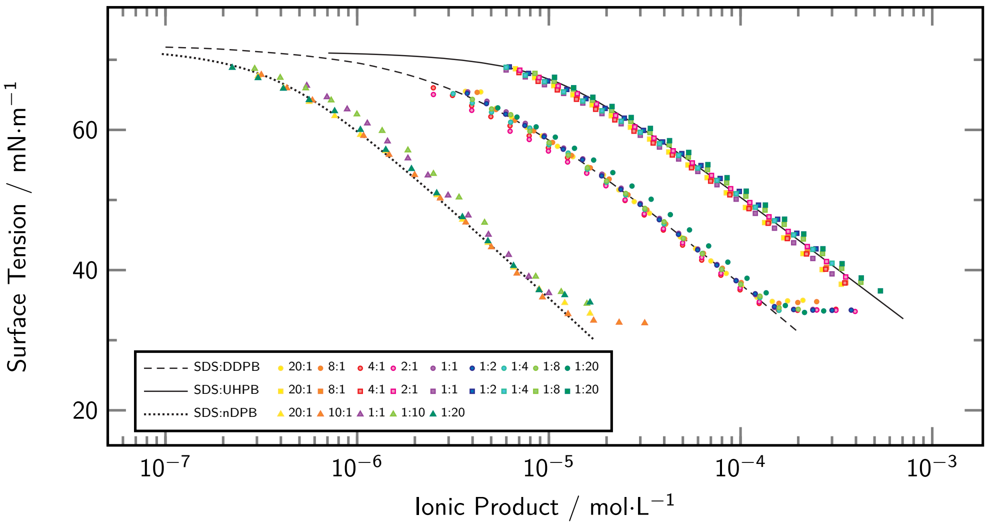

Figure 4.6.: Data from figure 4.3 re-plotted as function of the surfactant-only ionic product $(c_{\mathrm{SDS}} \cdot c_{\mathrm{UHPB}})^{\frac{1}{2}}$, $(c_{\mathrm{SDS}} \cdot c_{\mathrm{nDPB}})^{\frac{1}{2}}$ or $(c_{\mathrm{SDS}}^2 \cdot c_{\mathrm{DDPB}})^{\frac{1}{3}}$, respectively. Frumkin-type fitting functions given as black lines.

Table 4.1.: Fitting parameters according to the basic Frumkin model for the curves shown in figure 4.6. (*a*) Literature data from ref. [108].

Surfactant	n	ω [10^5 m^2 mol^{-1}]	b [m^3 mol^{-1}]	a
SDS^a	2	2.9	0.16	1.44
SDS:UHPB	2	5.3	58	0.55
SDS:DDPB	3	7.8	228	0.59
SDS:nDPB	2	4.4	939	1.0

$$\Pi = \frac{nRT}{\omega}\left[\ln(1-\theta) + a\theta^2\right] \tag{4.11}$$

Here, a refers to the mean-field interaction parameter, b to the surface-to-solution distribution coefficient, Π to the surface pressure, ω to the partial surfactant area, n to the stoichiometry parameter and θ to the surface coverage, which is related to the surface excess via $\Gamma\omega = \theta$. The best-fit parameters to the experimental data are given in table 4.1. The extent of the surface-activity of the catanionic mixture is expressed by a large value of b and values $a > 0$ represent attractive interactions between the surfactants in the monolayer.

Regarding the molecular architecture, nDPB and UHPB differ solely by the terminus of their alkyl backbone (Methyl- for nDPB and hydroxy-terminus for UHPB). However, their surface-activity shows some dramatic difference. The same observation holds for the mixtures with SDS. Between both mixtures, b differs by a factor of $\simeq 20$. The huge increase in surface-activity after the combination of nDPB with the oppositely charged surfactant SDS comes from the mutual cancellation of headgroup charge, which allows the molecules to arrange closer to each other within the monolayer. This, in turn, yields a double-tail-type surfactant complex, with an increased overall hydrophobicity.

Although a similar headgroup attraction between SDS and UHPB takes place, this mixture does not produce such nicely parallel aligned alkyl-tails, since the hydroxy-terminus of UHPB is driven towards the water phase, which prevents SDS:UHPB from achieving a comparable hydrophobicity level. The SDS:DDPB mixture is located in between the 1:1 catanionic systems. The mean hydrophobicity can be explained by the formation of a trimeric complex which resembles the structure of a double-tailed gemini-surfactant. Here, the alkyl-backbone acts as a flexible spacer unit, which again prevents a compact tail-alignment, resulting in the medium hydrophobicity and surface-activity, consequently.

Evaluation of the Frumkin isotherms with respect to the adsorbed amount of surfactant is shown in figure 4.7. All three curves exhibit an asymptotic behaviour, approaching a plateau value at higher surface pressures. The 2:1 system appears to have the smallest surface excess of the investigated solutions, followed by the SDS:UHPB mixtures, and SDS:nDPB has the highest surface density, which is almost twice of the value of SDS:DDPB. This appears reasonable since for both surfactant complexes each sulfate headgroup is compensated

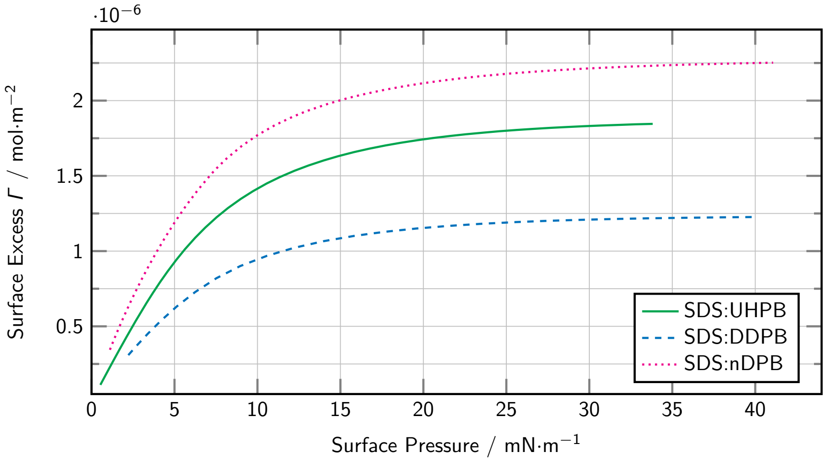

Figure 4.7.: Total surface excess of the catanionic mixtures SDS:nDPB, SDS:UHPB and SDS:DDPB as a function of the surface pressure according to the Frumkin fit (cf. figure 4.6).

by one pyridinium headgroup. SDS:UHPB, however, has an additional hydroxy group, which also demands some surface area and explains the intermediate value of Γ.

4.1.4. Adsorption Kinetics of Mixed SDS:DDPB solutions

While examining the equilibrium adsorption properties of differently composed mixed solutions of SDS and DDPB, significant deviations in the kinetics of droplet surface tension became obvious. The origin of these deviations will be discussed in this section. Figure 4.8 displays the time dependency of solutions approaching the same equilibrium interfacial tension as determined by the Du Noüy method within the margin of experimental error.

All shown curves exhibit a comparable overall appearance in logarithmic representation. Starting from $72\,\mathrm{mN\,m^{-1}}$, the surface tension first decreases very rapidly, which then transitions into a very slowly decreasing region at longer adsorption times. Despite these similarities, at different bulk compositions, the curves appear to be shifted along the time axis. The composition equal to

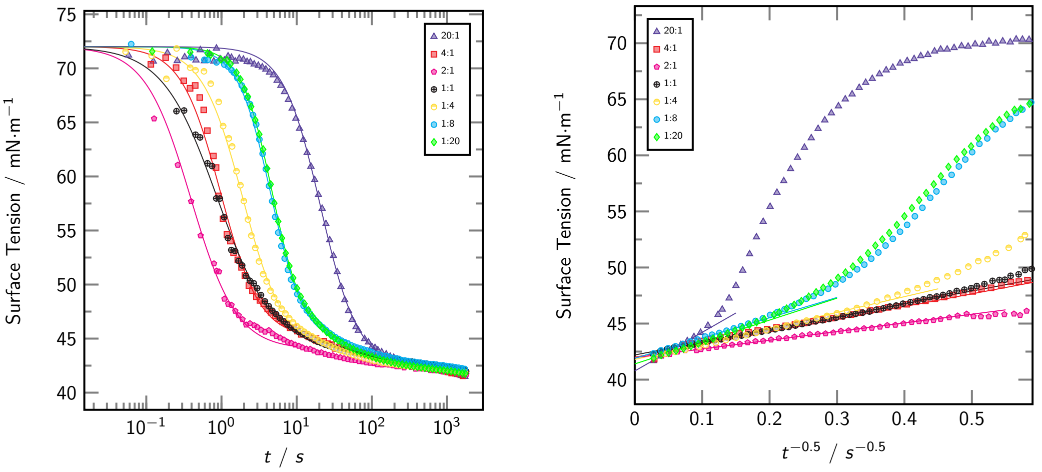

Figure 4.8.: Dynamic surface tension of mixed SDS:DDPB systems. Left: Data fitted with the empirical model of Rosen and Hua. Note that fitting functions are shown only in the valid regions. Right: Data rescaled with $t^{-0.5}$. Solid lines indicate the linear regions for long adsorption times.

the electroneutral stoichiometry requires the least amount of time to undergo the transition into the small-slope-regime. In turn, the greater the excess of either one compound in the mixture is, the longer it takes. The delay is more pronounced for the SDS-enriched mixtures than for the excess DDPB mixtures. To quantify the steep decrease experimental data were fitted with the empirical model of Rosen and Hua.[114]

$$\gamma(t) = \frac{\gamma_{\mathrm{H_2O}} - \gamma_{\mathrm{m}}}{1 + \left(\frac{t}{t^*}\right)^l} + \gamma_{\mathrm{m}} \tag{4.12}$$

In this relation t^* and l are fitting parameters, which usually mirror the rapidity of surfactant diffusion from the bulk to the subsurface in the early stages of adsorption and the ease of adsorption to the surface at advanced times, respectively.[115] γ_{m} refers to the surface tension at the so-called meso-equilibrium, which can be regarded as the endpoint of the rapidly decreasing region. It can be speculated, that at this point the surface layer has established

Table 4.2.: Dynamic surface tension fitting parameters of mixed SDS:DDPB solutions. Corresponding curves are shown in figure 4.8.

	Rosen & Hua Fit			Ward & Tordai $t \to \infty$	
Comp	t^* [s]	γ_m [mN m^{-1}]	l	grad [mN m^{-1} s$^{0.5}$]	γ_∞ [mN m^{-1}]
1:20	4.72	45.10	2.10	19.55	41.4
1:8	4.52	44.53	1.96	18.10	41.9
1:4	1.91	44.13	1.61	14.01	41.8
1:1	0.87	44.20	1.20	11.4	42.2
2:1	0.39	44.00	1.43	7.75	42.0
4:1	0.97	45.07	1.66	11.3	42.0
20:1	20.7	42.50	1.75	34.47	40.8

a near-stoichiometric surface composition. Results from the fitting procedure are given in table 4.2.

Despite yielding an adequate fit for surface tension values above the meso-equilibrium the present model is not able to capture the slowly decreasing region at long adsorption times. Rescaling of the data reveals a linear $^1/\sqrt{t}$-dependency of the surface tension for that particular region, as shown in figure 4.8. Such behaviour is a feature of a diffusion-controlled adsorption mechanism, as pointed out in numerous publications.[116–118] The corresponding mathematical relationships can be expressed by the famous equation of Ward and Tordai,[119] which connects the surface excess Γ with the surface age t, the diffusion coefficient of the surfactant D, and the bulk- and subsurface concentrations c_0 and c_s:

$$\Gamma(t) = 2c_0\left(\frac{Dt}{\pi}\right)^{\frac{1}{2}} - 2\left(\frac{D}{\pi}\right)^{\frac{1}{2}}\int_0^t c_\mathrm{s}(t-\tau)\mathrm{d}\tau^{\frac{1}{2}} \tag{4.13}$$

Here, τ serves as a dummy variable for the integration process. This equation can be solved analytically for two limiting cases: a freshly formed interface ($t \to 0$) and at very long adsorption times ($t \to \infty$). For short adsorption times, the proper determination of $t = 0$ is a puzzling issue and therefore the adsorption kinetics are only analysed near the equilibrium in this work. According to the asymptotical solution approach of Joos and Rillaerts[120] for adsorption layers close to the equilibrium coverage Γ_∞, the dynamic surface tension is given by:

$$\left(\frac{d\gamma}{dt^{-\frac{1}{2}}}\right)_{t\rightarrow\infty} = \frac{nRT\Gamma_\infty^2}{c_0} \cdot \left(\frac{\pi}{4D}\right)^{\frac{1}{2}} \tag{4.14}$$

Here, n serves as stoichiometry coefficient for ionic surfactants. In the previous section, the 2:1 complex formed by SDS and DDPB was shown to be dominating the adsorption layer within a broad window of different compositions with a little possible excess of the more surface-active anionic surfactant, which suggests n to equal 3. Additionally, the amount of adsorbed species, determined via the method of Gibbs, can be approximated by a single value independent of the respective composition, since all experimental data can be adequately fitted with the same function after rescaling of the abscissa.

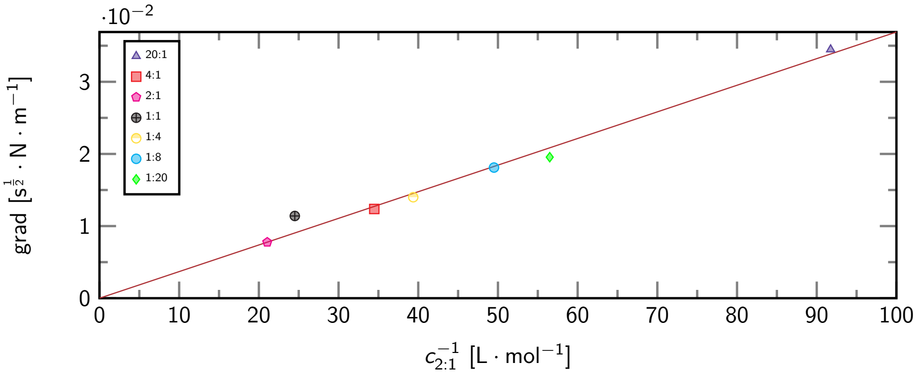

Figure 4.9.: Slopes of the linear decreasing regions from figure 4.8 as function of the inverse effective concentration of catanionic complex $c_{2:1}^{-1}$.

According to equation 4.14, the slope of the rescaled dynamic surface tension plot is inversely proportional with respect to the bulk concentration of the respective surfactant in solution. Figure 4.9 indicates that the adsorption process for $t \to \infty$ is dominated by the diffusion of the electroneutral complex, even though one of either compounds in the mixture might be present in excess. This fact manifests in a linear relationship between the surface tension gradient and the inverse effective concentration of the catanionic complex $c_{2:1}^{-1}$. Latter quantity equals c_{DDPB} for mixtures with $X_{\mathrm{SDS}} \geq 0.667$ and $0.5c_{\mathrm{SDS}}$ for $X_{\mathrm{SDS}} < 0.667$.

In conclusion, the 2:1 composition was found mirrored not only in the equilibrium surface tension of the solutions, but also in the evolution of γ over time for near saturation adsorption. For an excess concentration Γ_∞ of $1.24\,\mathrm{mol\,m^{-2}}$ the found mean effective diffusion coefficient D thereby is $0.84 \times 10^{-10}\,\mathrm{m^2\,s^{-1}}$. In comparison, the diffusion coefficient of SDS is reported to be around $5 \times 10^{-10}\,\mathrm{m^2\,s^{-1}}$.[30,121,122] This discrepancy is indicative for an adsorption barrier at higher surface pressures. Similar to that, Eastoe et al.[123] postulated an adsorption barrier for the ion pair amphiphile *n*-hexylammonium *n*-dodecylsulfate, which lead, depending on the bulk concentration, to experimental diffusion coefficients of only 7-55% of the expected value $4.1 \times 10^{-10}\,\mathrm{m^2\,s^{-1}}$. They argued that the high surface pressure and the dense surface packing may be responsible for an additional amount of work which is required for the surfactant to insert itself into the monolayer.

4.1.5. Analysis of the Surface Layer with Sum-Frequency Generation Spectroscopy

4.1.5.1. Pure Pyridinium Surfactants

It has been shown that ionic surfactants create an electric double layer at the interface.[124,125] According to the model of Stern, Gouy and Chapman the electric potential ϕ_0 at a charged surfactant layer depends on the charge density of the interface σ and the ionic strength I of the bulk solution.[22,126]

$$\phi_0 = \frac{2k_BT}{ze_0} \cdot \sinh^{-1}\left(\sigma\left(\frac{1}{8\epsilon_0\epsilon_r k_B T I}\right)^{1/2}\right) \qquad (4.15)$$

k_B refers to the Boltzmann constant, e_0 to the elementary charge, ϵ_0 to the dielectric constant, ϵ_r to the relative permittivity, z to the sign of the surface charge. Within the framework of this model, the depth of the double-layer region is represented by the Debye length κ^{-1}, which for relevant ionic surfactant concentrations (100 to 0.1 mmol L^{-1}) lies in the range between 1 and 30 nm. As a consequence, water molecules, since they possess a permanent dipole moment, are aligned within the proximity of the charged surface. This, in turn, gives rise to a signal in the SFG-spectrum located at the greater spectral region around 3300 cm^{-1}. It has been postulated, that these contributions to the effective susceptibility are not solely due to second-order terms $\chi^{(2)}$ by directly bound water molecules, but also come from a third-order susceptibility contribution $\chi^{(3)}$ by ordered water in the extended double layer region. The extent of the SFG-response is depending on surface potential and bulk ionic strength I and can be expressed as follows:[127,128]

$$I_{\mathrm{SFG}} \sim \left| E_{\mathrm{VIS}} E_{\mathrm{IR}} \left(\chi^{(2)} + \frac{\kappa(I)}{\kappa(I) + i \cdot \Delta k_z} \chi^{(3)} \phi_0 \right) \right|^2 \tag{4.16}$$

Δk_z represents the phase mismatch along the surface normal z. Accordingly, for high electrolyte concentrations, the SF-intensity increases together with the surface charge density and decreases together with the screening length. For a finite surface potential and very dilute electrolyte solutions ($\kappa^{-1} \ll 1\,\mathrm{mmol\,L^{-1}}$), above model suggests that the depth of the SFG-active region is no longer negligible concerning the SFG coherence length Δk^{-1}.[127,129] Thus, the effective $\chi^{(3)}$ contribution vanishes due to destructively interfering water layers. In the medium concentration range, the third-order contribution is modulated by the interplay between wave vector mismatch and Debye screening length.[130]

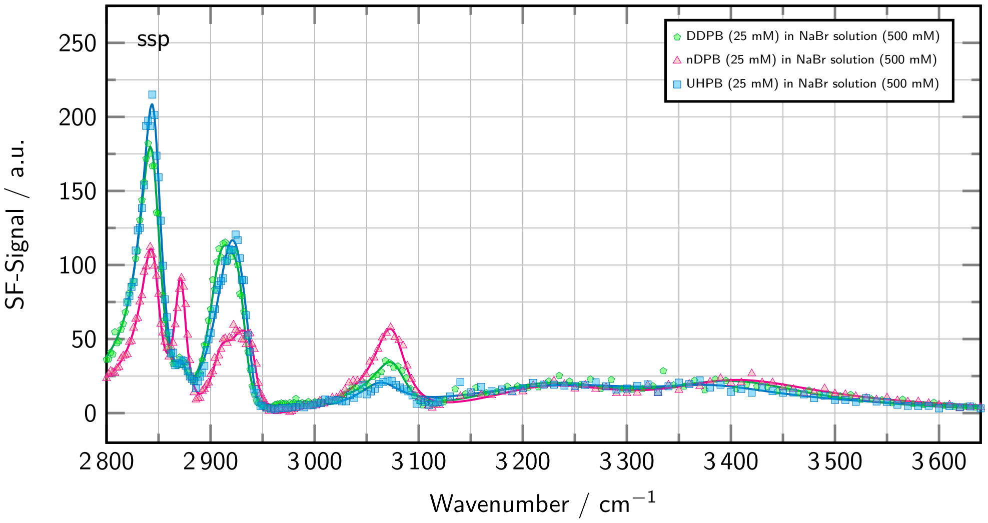

Figure 4.10.: SFG-Spectra (*ssp*) in the overlapping spectral range of CH- and OH vibrational modes. Samples were prepared identically: $25\,\mathrm{mmol\,L^{-1}}$ surfactant in an aqueous NaBr solution ($0.5\,\mathrm{mol\,L^{-1}}$). Data is superposed to highlight the differences and similarities between the individual spectra.

To facilitate the evaluation of signals originating from different CH groups it is beneficial to diminish the contribution of OH vibrational modes. Accordingly, a swamping amount of electrolyte (0.5 mol L^{-1} NaBr) was added to the samples shown in figure 4.10. It compares the SFG-spectra of equally concentrated DDPB, UHPB and nDPB in aqueous electrolyte solutions. In the following, peak assignment coincides with data reported in the literature.[80,126,131] All three spectra show a spectral feature with a maximum at 2840 cm^{-1}, which can be ascribed to the symmetric stretch of methylene units, referred to as d^+ mode. The spectrum of nDPB shows an additional peak at 2872 cm^{-1}, nearly absent in the spectra of bola solutions, which belongs to the vibrational mode of a methyl group symmetric stretch (r^+).

All spectra exhibit a signal located in the region between 2885 and 2950 cm^{-1}. These features are usually ascribed to the so-called Fermi resonances $d^+_{\mathrm{FR}}/r^+_{\mathrm{FR}}$, which originates from symmetric stretching combined with a bending overtone. At 3075 cm^{-1} one observes a signal which can be attributed to unsaturated CH stretching modes in the pyridinium ring.[132–135] Adjacent to that either spectrum exhibits a more or less identical profile, in which a non-zero intensity extends beyond 3600 cm^{-1}, although no sharp peaks are present. This feature is due to two stretching modes of interfacial water, which are usually found as two rather broad bands at around 3200 and 3450 cm^{-1}.[126] By the addition of excess electrolyte alignment of water was reduced down to the first few water layers below the surfactant monolayer resulting in rather weak signals from OH vibrational modes.

In the bola spectra, one observes a small residual peak from r^+ resonances at 2870 cm^{-1}. This signal may originate from trace amounts of surfactant impurities. However, these traces are hard to eliminate entirely, but also only show minor contributions to the SFG-spectrum, and are therefore tolerated in the context of this work. A spectral feature, which is barely visible without a fitting routine is a signal in the Fermi resonance region at around 2945 cm^{-1}. It interferes destructively with the other signals in the spectrum, resulting in a small overall SFG-intensity around the peak centre.

A peculiarity of d^+ modes in SFG experiments is their sensitivity towards the conformation of the alkyl backbone. Since in an all-trans geometry every methylene unit shares an inversion centre with its immediate neighbours (cf. figure 4.11), these groups do not contribute to the SFG-signal. By the introduction of so-called Gauche-defects inversion symmetry is partially broken and the corresponding signal is now visible in the SFG-spectrum.

The d^+ intensity in the spectrum of the bolaamphiphiles significantly exceeds the one of nDPB. This may be due to two different circumstances, both illustrated in figure 4.1. First, DDPB is forced into a bend at the interface, which inherently requires the backbone to deviate from the all-trans conformation at several positions in the alkyl spacer. Secondly, in *ssp* polarisation, vibrational modes show a maximum contribution to the SFG signal when their dipole moment is oscillating parallel to the surface normal.[83] This scenario is more likely to be found in a monolayer of reversely U-shaped alkyl moieties than in somewhat disordered, yet more or less upright positioned hydrophobic tails. The larger oscillator strength of the aromatic CH stretch for nDPB suggests a higher number density of pyridinium headgroups in the surface at equal surfactant concentrations, which coincides with tensiometry results.

For linear surfactant species, comparison of the oscillator strengths of d^+ with r^+ of the terminal methyl unit, which is SFG active regardless of the intramolecular conformation, allows estimating the degree of order in the monolayer. According to that, the spectrum of nDPB, which features both,

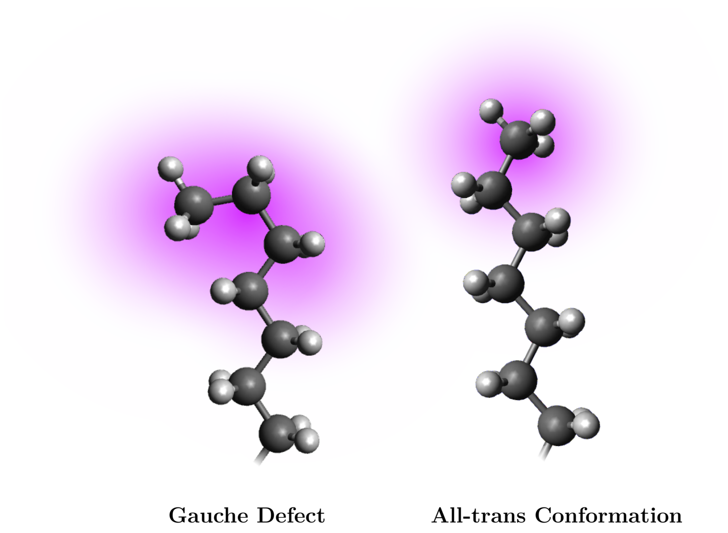

Figure 4.11.: Ball-and-stick model of different possible alkyl conformations in a surfactant monolayer. Molecular sites where internal centrosymmetry is broken, and thus are SFG-active, are indicated by a shaded region.

d^+ and r^+ signals with comparable magnitude, implies a slightly disordered monolayer, in agreement with previously reported studies about ionic soluble surfactant adsorption layers.[124,136,137]

Figure 4.12 shows a concentration study of the linear alkyl pyridinium surfactant from 100 to 0.1 mmol. All four spectra display the same spectral features as mentioned previously. Additionally, a significant drop in intensity around 2945 cm^{-1} can be observed now, due to the destructive interference of the asymmetric methyl stretching mode with the background intensity. Comparing the different spectra to each other reveals two main observations. First, the alkyl signals are increasing with concentration and level off above the cmc. This trend appears reasonable, since the number of molecules increases until the cmc is reached, and remains more or less constant afterwards. Similar to the spectrum with added NaBr, within the whole concentration series the methylene-mode exhibits a greater intensity, as compared to the methyl-symmetric stretch,

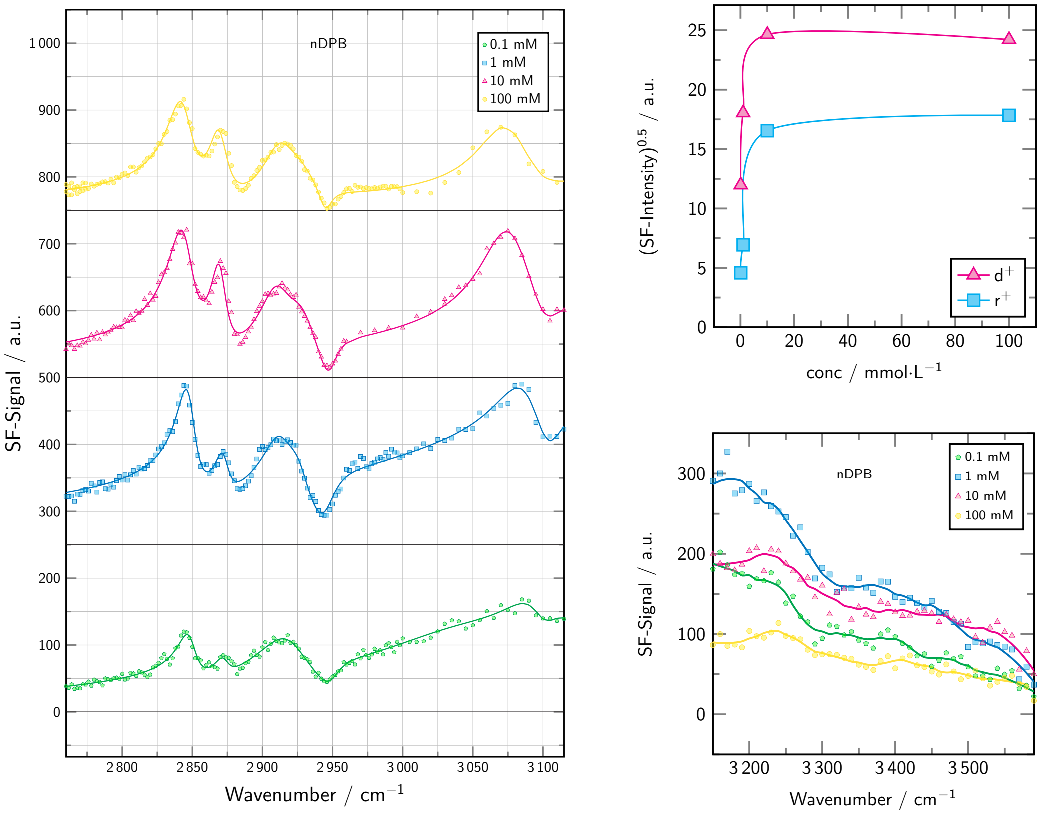

Figure 4.12.: left: SFG-spectra (*ssp*) of nDPB solutions varying in concentration within the spectral regime of CH-modes. Fitted data is given as solid lines. Right top: SFG-intensity square root of the symmetric stretching modes of methyl- and methylene groups as function of the surfactant concentration. Right bottom: SFG-Intensity in the spectral region of water modes. Solid lines obtained by a Savitzky-Golay smoothing routine.

even at concentrations far beyond the cmc. A little compression effect, i.e. a decrease of the relative amount of contributing methylene stretching modes, can be observed since the intensity ratio r^+/d^+ increases from 0.38 in the dilute system to 0.73 at high concentrations.

The second observation concerns the intensity caused by the water bands on the right side of the spectrum. It exhibits a non-monotonous trend, which is maximum at 1 mmol L^{-1}. This trend is also displayed in the inset of figure 4.12, where the greater water mode region from 3200 to 3600 cm^{-1} is shown.

As already mentioned, increasing the surfactant concentration below the cmc elevates the number of adsorbed molecules. Due to the ionic nature of nDPB this should also increase the net surface charge and therefore the intensity of the water signal, due to water dipole alignment. Such behaviour has been reported for the ionic model surfactants SDS and dodecylammoniumchloride.[126]

However, after a signal increase from 0.1 to 1 $\mathrm{mN\,m^{-1}}$ the signal drops down again with further concentration increase, even though the alkyl intensities follow the expected trend. A similar behaviour has been presented in the literature for the cationic surfactant cetyltrimethylamoniumbromide.[138] The authors argue, that with increasing surface concentration the resulting surface charge is compensated by the reduced screening length. Furthermore, it has been reported that for certain combinations of ionic surfactant and counterions at the interface, the electrochemical double layer is appears to be more compact, as one would expect disregarding ion specific effects.[124,139,140] The combination of a pyridinium headgroup with bromide ions here may lead to a certain degree of counterion condensation on the positively charged surfactant monolayer. Thus, the penetration depth of the electric field is reduced, yielding a net reduction of the water signal.

Figure 4.13 displays the SFG-spectra in the overlapping spectral range of CH and OH vibrational modes of aqueous DDPB solutions with concentrations of 25, 50, 100 and 200 $\mathrm{mmol\,L^{-1}}$, which corresponds to the regime with considerable adsorption as verified via surface tension measurements. No electrolyte was added here. All four samples reveal the spectral features previously analysed. As mentioned above, minor contributions from methyl vibrations which are caused by trace impurities had to be added to obtain a good fit.

Curiously, at first glance, the trend points to the opposite direction as

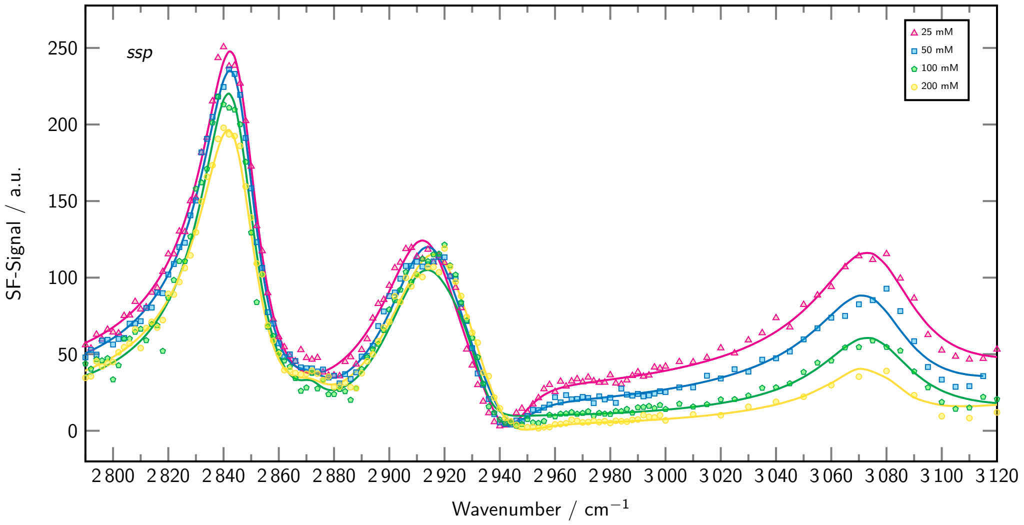

Figure 4.13.: SFG-spectra (*ssp*) of DDPB solutions varying in concentration within the spectral regime of CH-modes. Fitted data is given as solid lines.

one would initially expect. In concrete terms, the peak intensities of the d^+ band and the region above 2950 cm^{-1} are decreasing with increasing bulk concentration, whereas the intensity of around 2920 cm^{-1} remains almost the same. As discussed before, in the pre-micellar regime surface excess in general increases with bulk concentration, however, one observes a decrease in the peak maxima of the d^+ mode.

This paradox is due to interference with the peak tails of the water signal lying underneath, as described by Gragson et al.[126] for a series of SDS solutions. Below the cmc ($\simeq$ 170 mmol L^{-1}), fitting the spectra to equation 3.15 reveals that the peak integral square roots of the shown curves deviate only within a small interval (40.3 ± 1.6) which is less than the expected experimental error. This might indicate that the surface layer has already achieved near saturation adsorption even for the least concentrated solution in this series. An alternative explanation for the stagnant intensity might be a balance between an increasing amount of adsorbed surfactant and a simultaneous decrease in Gauche-defects.

However, this scenario is not very likely, considering the quadratic relationship between SF-intensity and number density. Since both ionic headgroups are anchored in the aqueous phase, transition towards a stretched out dumbbell-like geometry does not appear, as evidenced by the comparably high intensity of the $\nu_\mathrm{s}(\mathrm{CH}_2)$, even at the highest surface pressures observed for DDPB.

The right-hand side features arising with lower concentrations can be attributed to the weak surface-activity of DDPB. A comparably high amount of surfactant is required to produce a considerable surface tension reduction. As a consequence, also a high concentration of counterions is present in solution, which in turn reduce the penetration depth of the cationic monolayer's electric field due to electrostatic screening or even counterion condensation. Accordingly, SFG contributions of interfacial water, whose peak tails also reach far into the spectral region of CH vibrations are reduced for higher DDPB concentrations. Another aspect to be addressed here is the constructive or destructive character of signal interference. Both scenarios are present in that particular spectral region, most obvious in the least concentrated sample. The dip in intensity around $2950\,\mathrm{cm}^{-1}$ is frequently ascribed to destructive interference between an OH stretching and a CH-resonance mode.[126] Contrarily, the aromatic CH stretching experiences an enhancement due to constructive interference. As will be shown later, this trend gets inverted when the monolayer charge switches from positive to negative.

For the solution of the compound UHPB the picture is quite the same as for DDPB (cf. figure 4.14). Increase in the bulk concentration of a factor eight leaves the d^+ contribution nearly unaffected but at the same time has a severe influence on the intensity of the water modes. This is explicitly displayed for the two compounds in figure 4.15. Both surfactants show a reduction of the

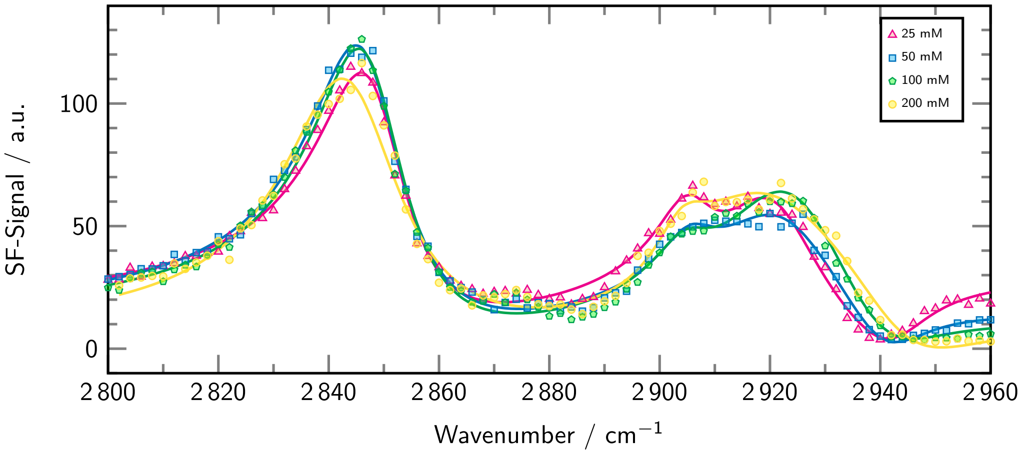

Figure 4.14.: SFG-spectra (*ssp*) of UHPB solutions varying in concentration within the spectral regime of CH-modes. Fitted data is given as solid lines.

water signal when diluted from 200 to 25 mmol L^{-1}. This is in accordance with what has been observed for the nDPB solutions, i.e. a decrease in the intensity for concentrations greater than millimolar. Since all the measurements of the water region, have been performed with the same adjustment, intensities could be directly compared. Assuming a similar amount of adsorbed surfactant, the difference in the absolute value of the SFG response can be explained by the stoichiometry of the ionic surfactants. With respect to the bulk concentration, the ionic strength of a solution of the 1:1 electrolytes UHPB and nDPB is equivalent, whereas for the 2:1 compound DDPB it scales with factor three. Therefore, the penetration depth of the surface electrical field in DDPB solutions is reduced due to increased screening effects, which explains the lower signals for equal concentrations in the regime between 3100 and 3600 cm^{-1}.

4.1.5.2. Mixed Surfactant Systems

As previously shown, interference with signals originating from water modes vastly influences the SFG-spectrum of CH-modes. In fact, high levels of

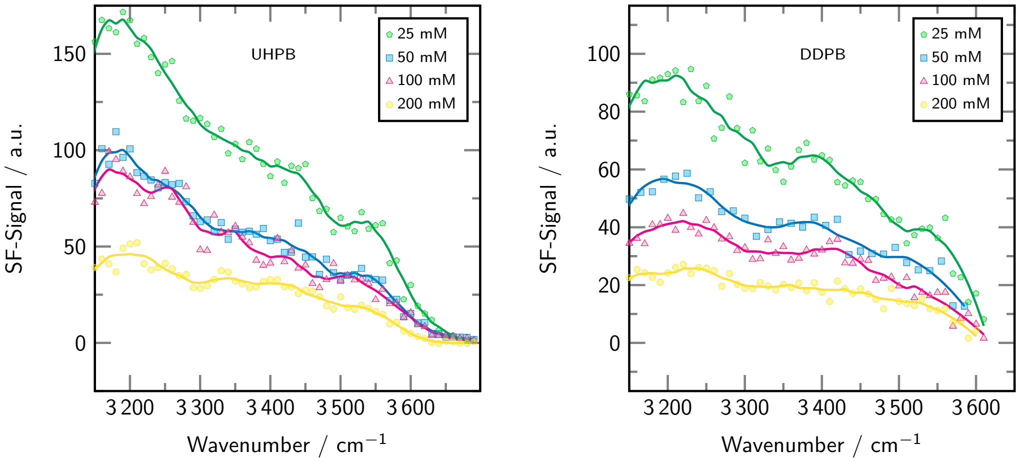

Figure 4.15.: SFG-spectra (*ssp*) in the spectral regime of OH-modes. For each surfactant several bulk concentrations were measured. Data was smoothed via the Savitzki-Golay method. Left: UHPB; Right: DDPB.

background signal can make the evaluation and modelling of SFG-spectra quite puzzling. To illustrate that, spectra of an 8 mmol L^{-1} solution of SDS in conventional water and in perdeuterated water D_2O were measured and analysed with respect to their d^+ and r^+ vibrational modes (cf. figure 4.16).

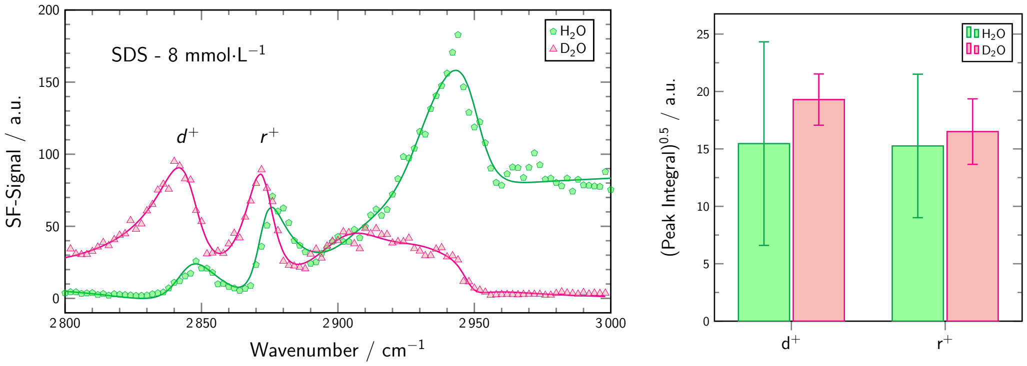

Figure 4.16.: Left: SFG-Spectra (*ssp*) in the spectral range of CH vibrational modes with corresponding fits for the air-water-interface of SDS solutions in regular or perdeuterated water. Right: Peak intensities of symmetric stretching vibrations with corresponding error bars.

The outcome spectra differ a lot in their overall shape. This is due to the displacement of the interfering solvent vibrational signals caused by the isotope exchange. The higher reduced mass of the OD group shifts its peak maxima further away from the CH-stretching region and subsequently results in a less significant influence on the CH-signal intensity.[126] Whereas H_2O contributes to a lot of the overall SFG-intensity, especially on the right side, spectra of the sample in D_2O appear only moderately elevated on the left side of the CH-region.

Additionally, the interference with the water background leads to a relative blue-shift in the peak maximum wavelengths for samples in H_2O. The high level of background signal also causes some ambiguity in the best-fit parameters for methyl- and methylene vibrational modes. This manifests as comparably huge errors of the peak integral, as can be seen in the bar chart in figure 4.16. For this reason, in the following chapter, quantitative analysis is exerted only for the spectra in D_2O. Nevertheless, spectra of the sample in water are presented as well to estimate the effect of surface charge on the structuring of interfacial water.

For a first impression, the SFG-spectra of the two electroneutral mixed SDS:Bola systems in perdeuterated water D_2O are shown in figure 4.17. The *ssp* spectra will be discussed in more detail later on and only the main observations will be pointed out here. For the perdeuterated mixtures of both systems, i.e the ones which contain h_{25}-SDS as co-surfactant, very large d^+ signals, as compared to the spectra of bare SDS, are found, which tower over the entire spectrum and especially the r^+ vibrational mode. The spectrum of SDS:UHPB possesses a slightly higher d^+ intensity maximum.

By the use of deuterated SDS as mixture partner, its contribution, in analogy to D_2O, can be hidden, and only the spectral contribution of the

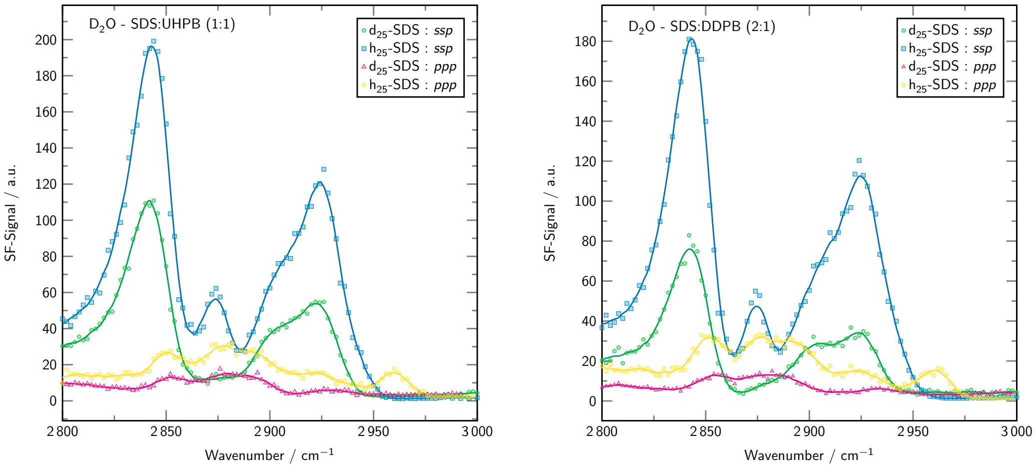

Figure 4.17.: SFG-Spectra (*ssp*, *ppp*) of the stoichiometric SDS:DDPB (right) and SDS:UHPB (left) mixtures in D_2O in the spectral range of CH-modes. Data was smoothed via the Savitzki-Golay method (solid lines). The mixed solutions yield a surface tension of $40\,\mathrm{mN\,m^{-1}}$, according to tensiometry.

cationic surfactant becomes visible. For both d_{25}-SDS:bola systems, the *ssp* intensity is considerably reduced and the r^+ contribution disappears completely. In accordance, the signal around $2965\,\mathrm{cm^{-1}}$ in *ppp* polarisation also vanishes, which belongs to the asymmetric methyl vibrational mode r^-. This verifies the absence of surface-active impurities bearing methyl groups in the surface layer. It can be argued, that the high surface-activity of the mixed systems, now repels any possible impurities from the surface layer. In comparison, the d^+ signal of the SDS:DDPB mixture loses a bit more in relative intensity upon partial deuteration. Unfortunately, the *ppp* spectra, which in theory should display vibrational modes from symmetric and asymmetric stretching vibrations, are not very intense and rather poorly resolved, which makes this polarisation combination unsuitable for quantitative analysis of the present systems.

Figure 4.16 shows SFG-spectra of differently composed SDS:DDPB mixtures in H_2O (left panel) ad D_2O (right panel), each yielding a surface tension of approximately $40\,\mathrm{mN\,m^{-1}}$ according to results from tensiometry. The usage of perdeuterated co-surfactant d_{25}-SDS instead of conventional h_{25}-SDS enables identifying the origin and extent of a spectral contribution, since the CH and CD vibrational modes are located in different spectral regimes. Comparing the spectra of the mixtures in H_2O, unaffected of which SDS species is used, one observes a non-vanishing intensity in the high wavenumber region, increasing together with the SDS:DDPB ratio. In contrast to the pure DDPB, SFG-spectra of the respective mixtures exhibit a dip at $3080\,\mathrm{cm}^{-1}$ as well as a relatively high intensity for the Fermi resonance signal and a lack of a dip at $2950\,\mathrm{cm}^{-1}$. This implies a now constructive interference between OH and CH resonances and a destructive relationship between OH and aromatic CH modes. All these features can be ascribed to the inverted sign of the overall surface charge.

By the addition of SDS to the system, monolayers are obtained which contain a slight excess of the anionic dodecyl sulfate ion due to its superior surface affinity. Note that the excess refers to the headgroup charges, which implies surface compositions $\geq$ 2:1 for the shown mixtures. The water alignment appears to be most pronounced for the SDS rich mixture and least pronounced for the DDPB-rich mixture, with the stochiometric 2:1-composition located somewhere in between. On their high-wavenumber-end corresponding spectra do not differ much for mixtures with d_{25} and h_{25}-Co-surfactant. This confirms that the structuring of the water sub-layer is not affected by the perdeuteration of one of its components since both spectra exhibit an identical extent of the water peak tail.

The peak wavenumber of the d^+ mode in spectra of mixtures containing perdeuterated SDS shifts from 2845 to $2848\,\mathrm{cm}^{-1}$ with increasing SDS content, whereas for the d_{25}-Co-surfactant maxima are located between 2848 and $2855\,\mathrm{cm}^{-1}$. The signal corresponding to the r^+ vibration is located at

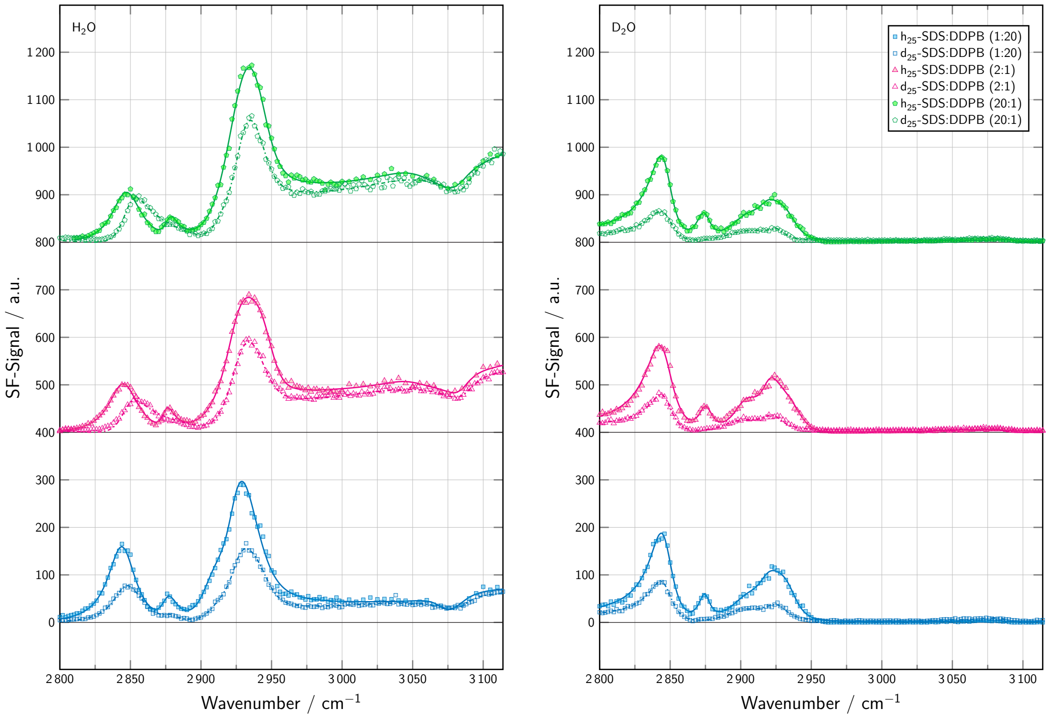

Figure 4.18.: SFG-Spectra (*ssp*) in the overlapping spectral range of CH- and OH vibrational modes with corresponding fits for selected compositions of SDS and DDPB. Filled symbols and solid lines correspond to the normal surfactant mixtures, open symbols and dotted lines to the mixtures with perdeuterated surfactant d$_{25}$-SDS. Normal (left) and deuterated (right) water was used as solvent. Spectra are offset for clarity.

2877 cm^{-1} in the mixed h$_{25}$-SDS:DDPB spectra. Fermi resonances are responsible for the large signals at 2930 cm^{-1}, whereby the fully protonated mixtures always produce a higher SFG-intensity. This is quite reasonable since both, methylene and methyl units contribute to the signal and SDS is masked when using the d$_{25}$-species. When it comes to the interpretation of the symmetric CH$_2$,CH$_3$ and Fermi resonance modes one has to be careful, because interference phenomena appear to be crucial for the signal shape and position here. It has been shown that signal interference can alter peak position and shape in SFG-spectroscopy.[136,141,142] As stated earlier I_{SFG} is proportional to the square of the absolute value of the complex quantity $\chi^{(2)}$. By varying the surfactant composition and/or by perdeuteration of one component, contributions to the overall second-order susceptibility are altered, or suppressed, respectively. As a result, different peak maxima in the SFG-intensity spectrum are observed.

Performing the same study in D_2O, allows suppressing the huge water peak tails in the CH-spectral region. As can be seen in figure 4.18, all three investigated surfactant mixtures produce very similar SFG-spectra, which in accordance to the results from tensiometry, suggests a rather constant composition of the adsorbed surfactant monolayer within a broad regime of different bulk compositions.

In analogy to the spectra of the sample in H_2O, the intensity of the d^+ mode of the perprotonated mixture significantly exceeds the intensity of the r^+ mode, again followed by a broad feature between 2890 and 2950 cm^{-1} which contains the methyl- and methylene Fermi resonance modes and also possible contributions from the corresponding asymmetric stretching modes. By contrast, from there on, no intensity can be observed up to 3100 cm^{-1}, except for a now very weak contribution around 3080 cm^{-1} from the aromatic CH stretching modes, as compared to the clear dip in intensity using H_2O as the solvent. This again showcases the significant influence of interference effects for the observed signal intensity in SFG-experiments. Perdeuteration of the dodecyl sulfate co-surfactant leads to a significant reduction of the SFG-intensity for all the aliphatic CH-vibrational modes. This time, no noteworthy shift between the peak maxima for the two different solvents can be detected. Analysis of the fitted spectra and comparison to the other two mixed systems will be discussed later on.

Figure 4.19 displays the SFG-spectra of the previously discussed d_{25}-SDS:DDPB mixtures in the spectral range from 2000 to 2200 cm^{-1}, which

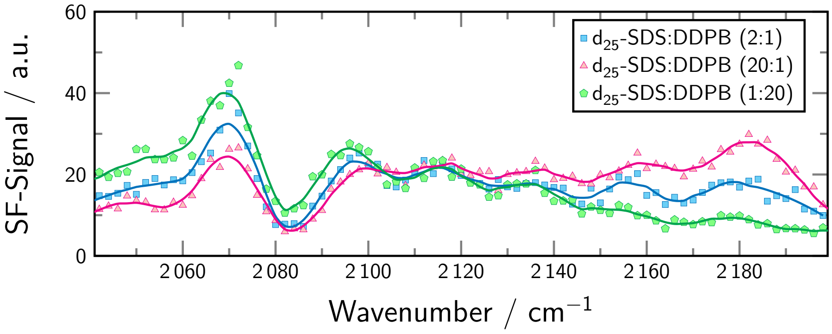

Figure 4.19.: *ssp* spectra of the d_{25}-SDS:DDPB mixture in the spectral range of CD vibrations. Savitzky-Golay smoothed curve given as guide to the eye.

corresponds to the CD-vibrations in accordance to the higher reduced mass of the CD-bond. The assignment of the peaks was made in agreement with the literature.[143–146] Note that variations in the Fermi interactions are believed to alter the peak sequence and cause different relative peak intensities in comparison to the CH-spectrum. Most prominently, the r^+ mode (2070 cm^{-1}) here appears further red-shifted than the d^+ vibration (2100 cm^{-1}). Other peaks can be ascribed to the d^+ Fermi mode (2115 cm^{-1}) and the asymmetric stretching mode d^- (2180 cm^{-1}).

Unfortunately, the signals are not as good resolved as in the CH region and obviously show a lot of interference effects. Thus, quantitative analysis via peak fitting was omitted. However, comparison of the overall shape of the spectra, especially for the asymmetrically composed samples, reveals similarities with two different types of monolayers. With the negligible intensity on the right side of the spectrum, the bola-rich mixture yields a profile which resembles the one of charge-neutral deuterated lipid monolayers in the liquid-expanded state.[144,145] In contrast, the spectral shape of the d_{25}-SDS-rich mixture appears to be quite similar to the spectrum of pure d_{25}-SDS on water. In ref. [143], the authors speculate about the origin of the elevated signal around 2160 cm^{-1}.

They propose a combination between the bending and libration modes of water that might be responsible. This is in agreement with what has been shown so far. The 1:20 mixture has only a small electric field present at the interfacial region, due to headgroup charge cancelling. Therefore, one could assume a relatively unperturbed behaviour of the surfactant monolayer. Contrarily, a considerable signal intensity above 3100 cm^{-1} indicates that SDS excess creates layers of aligned water molecules. In turn, this apparently gives rise to a contribution from water molecules, which additionally elevates the SFG-signal in the region of CD modes. Note, that due to the apparent signal overlap in the CD spectral regime, it offers only limited and ambiguous information, and thus its presentation for the SDS:UHPB mixture will be omitted.

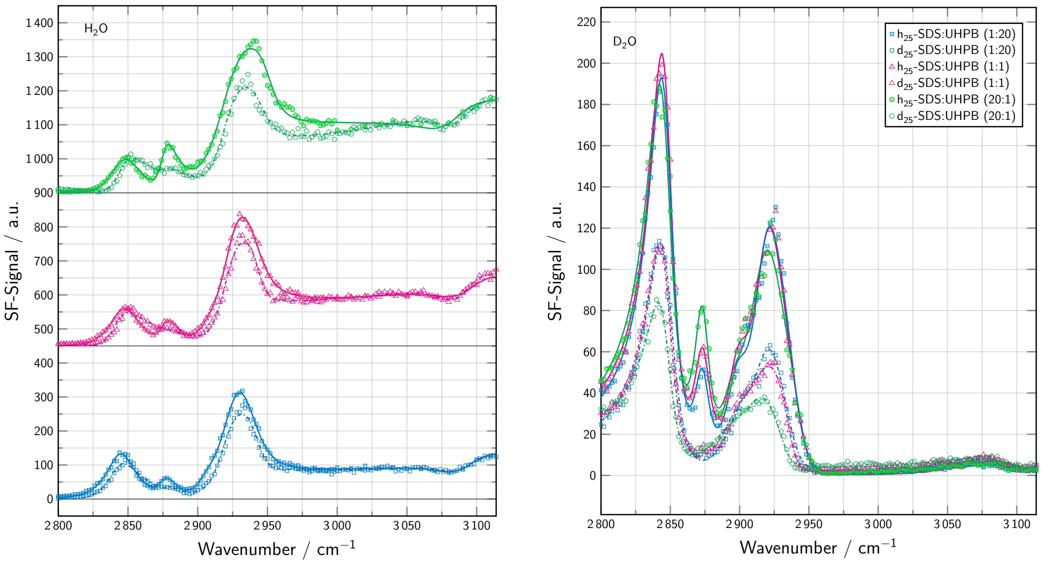

Figure 4.20.: SFG-Spectra (*ssp*) in the overlapping spectral range of CH- and OH vibrational modes with corresponding fits for selected compositions of SDS and UHPB. Filled symbols and solid lines correspond to the normal surfactant mixtures, open symbols and dotted lines to the mixtures with perdeuterated surfactant d$_{25}$-SDS. Normal (left) and deuterated (right) water was used as solvent. Spectra are offset for clarity.

Figure 4.20 displays a study of the mixed system SDS:UHPB similar as discussed before for SDS:DDPB. Bulk concentrations were again chosen to achieve a surface tension value of 40 mN m^{-1}, according to the tensiometry results. For the systems using conventional water as the solvent, one can observe a similar trend as found for the 2:1 mixed system. The influence of water modes is most pronounced for the SDS-rich mixture and gradually decreases with increasing DDPB content. Again, its extent is not affected by the deuteration of the anionic surfactant. Despite the similar trend for the background water interference, there are clear differences to the SDS:DDPB-spectra, regarding the CH-vibrational modes.

First of all, the dip in intensity around 3080 cm^{-1} is not as pronounced as for the 2:1 system, which suggests a smaller coverage with pyridinium headgroups, or a significant difference in the average orientation of the headgroup. Additionally, the region between 2960 and 2900 cm^{-1} does not exhibit an as pronounced intensity difference between the perprotonated and the mixture containing d$_{25}$-SDS as observed for the SDS;DDPB-mixture. This can be rationalised, considering the differences in stoichiometry. Whereas DDPB marks only around 33 % of the surfactant molecules in the monolayer, the UHPB-content is around 50 %, and therefore it contributes a bit more to the total SFG-Signal. The spectra in water are also indicating, that the r^+ signal is more obviously influenced by the variation of the mixture than for the SDS:DDPB-mixtures. However, the frequency shifts of the observed peak maxima of the d^+ mode upon partly deuteration of the surfactant mixture are not as pronounced in comparison.

Spectra of samples in D$_2$O also display a trend which is in accordance with observations discussed above. While the maximum intensity of the d^+ mode of the perprotonated surfactant mixture appears to not be affected by composition variation, the partially deuterated mixture exhibits a reduced d^+ mode for the SDS-rich mixture. The same observation holds for the region between 2900 and 2960 cm^{-1}. Additionally, the r^+ signal also increases with increasing SDS fraction. These three observations indicate an increasing content of dodecyl sulfate molecules in the monolayer. The higher sensitivity of the 1:1 system towards the variation of the composition might be due to the differences in stoichiometry. With respect to the mixtures electroneutral composition, a 20:1 mixture implies a more significant excess for a 1:1 system than for a 2:1 system, which can result in a more significant deviation from the electroneutral equilibrium composition.

That being said, none of the investigated SDS:Bola mixtures in H_2O show vanishing of the SFG-intensity above 3000 cm^{-1}. This implies compositions above the electroneutral composition since the interference pattern is not indicative of inversion of sign of the water mode. The latter was found to be opposite to the symmetric CH-stretching modes, which means destructive interference. The deviation from the electroneutral composition might be due to the higher surface-activity of SDS as compared to the bola surfactants. Nevertheless, tensiometry results suggested a near 2:1 / 1:1 composition. In order to understand the high signal contribution of water, a model, as shown in figure 4.21, will be proposed.

Therein, regions with aligned water molecules are depicted by dark blue shading. Gauche-defects in the alkyl-backbone are highlighted in violet. The proposed structure explains the high d^+ signal with respect to the r^+ mode in SDS:bola mixtures, which is represented by the comparably high number of SFG-active methylene groups. One has to keep in mind, that surface layers of aqueous ionic surfactant solutions, have been reported to already have a significant degree

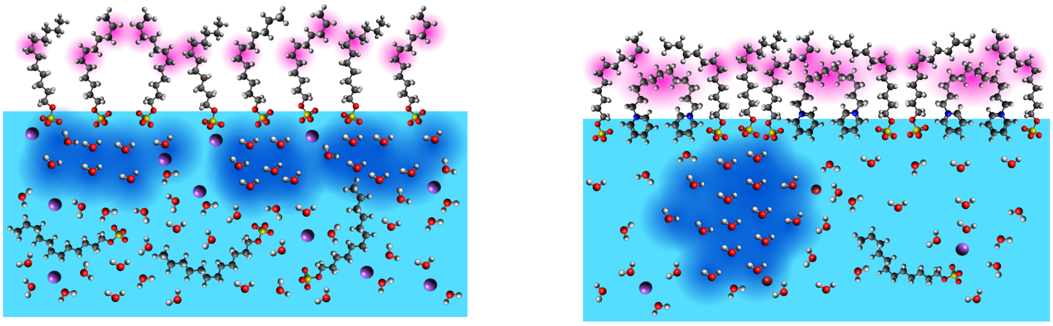

Figure 4.21.: Left: Schematic model of ionic surfactant (mixture) adsorption layers (not to scale). See text for detailed explanation. Left: SDS; Right: SDS:DDPB mixture.

of counterion binding of around 90 %.[35,108,127,147] A hypothetical replacement of the bound counterions by oppositely charged surfactants can be expected to leave the SFG contribution by aligned water molecules in the deeper layers nearly unaffected. Thus a near electroneutral composition of surfactants in the monolayer might be present despite a significant SFG contribution from $\chi^{(3)}$ terms.

Also note, that the total ionic strength in the catanionic aqueous mixture is fairly low, which enables the electric field of the surface layer to penetrate relatively deep into the bulk phase, due to the lack of ions in the volume phase, capable of charge screening (cf. figure 4.21). Thus, thanks to the higher value of κ^{-1}, a small effective surface charge may cause a considerable SFG-signal above $3000\,\mathrm{cm^{-1}}$. For comparison, κ^{-1} in the shown SDS sample ($I = 8\,\mathrm{mmol\,L^{-1}}$) amounts to 3.4 nm, whereas for the 2:1 mixture of SDS and DDPB ($I = 0.25\,\mathrm{mmol\,L^{-1}}$) it is 19.2 nm. Therefore, the high SFG-intensity on the right side of the spectrum may be caused by only a slight excess of dodecyl sulfate ions in the monolayer.

Figure 4.22 displays the peak area square roots, as determined from spectra deconvolution with equation 3.15, for the d^+ and r^+ vibrational modes of the SDS:bola mixtures. The exponent of 0.5 compensates the quadratic relationship between SFG-intensity and surface concentration and enables a direct comparison of the individual signals. In order to account for interference from D_2O vibration peak tails, a quasi non-resonant background intensity $\chi^{(2)}_{\mathrm{NR}} = A_{\mathrm{NR}} \cdot e^{i\phi}$ (with phase angle ϕ) was considered during the fitting process.

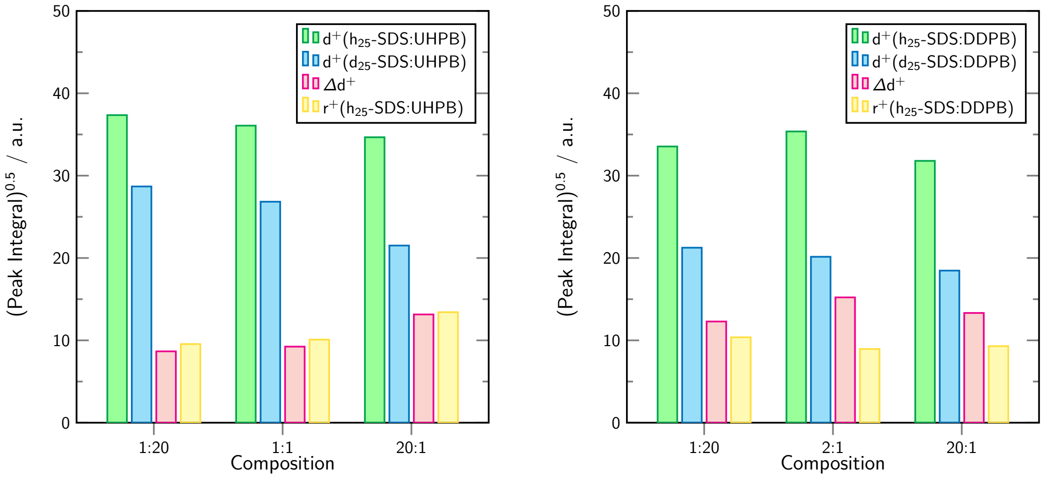

Figure 4.22.: Area square root of the deconvoluted peaks for the mixed systems SDS:Bola in D_2O.

Between the differently composed SDS:UHPB mixtures, a trend can be observed. Whereas the d^+ signal of the perprotonated mixture almost maintains its height, the SDS-masked spectrum does exhibit a decrease in the d^+ mode with increasing SDS content. In accordance, the r^+ intensity increases, which indicates enrichment in dodecyl sulfate content. However, as the bulk composition is ranging from 5 to 95 % of SDS, SFG-spectroscopy could show that the catanionic mixture does only slightly vary its surface stoichiometry. Assuming, that the signal difference between d_{25}-SDS:UHPB and SDS:UHPB spectra can be assigned to the alkyl tail of the anionic surfactant, a near-constant ratio $r^+/\Delta d^+ \geq 1$ is found for the investigated mixtures. This implies an equally-to-slightly-better aligned dodecyl sulfate backbone in the mixed monolayer, as compared to pure SDS solutions yielding similar surface tension.

The three investigated SDS:DDPB mixtures yield almost identical intensity distribution of d^+ and r^+ signals, which again shows the surface stoichiometry to be rather stable. The d^+ intensity of the SDS-masked spectrum is lower as compared to the SDS:UHPB mixtures, which agrees with the bolaamphiphile proportions of $^1/_2$ and $^1/_3$ in the electroneutral complex. The 2:1-surfactant complex apparently induces few more Gauche-defects in the *n*-dodecyl tails, which is indicated by the intensity ratio $r^+/\Delta d^+ < 1$.

The tendency towards more order in dodecyl sulfate for SDS:UHPB might be due to the smaller required area for the hydroxy head group of UHPB, thus enabling a more dense packing of the monolayer. Another possibility might be partial straightening of the alkyl backbone in UHPB, which could induce better alignment of the dodecyl sulfate tails. Similar behaviour has been reported for mixed adsorption layers of SDS and dodecanol.[148] According to the authors, the mixture adsorbs as complex, where the hydroxy group is pointing towards the gas phase. However, for the presented system, such a mechanism is not very likely, as verified by the significant overall d^+ intensity.

Neglecting the influence of the individual angular distribution on the SFG output of methyl and methylene groups, the relative intensity relations between those signals can also be used for the rough estimation of the monolayer composition and the degree of bending in the bolaamphiphiles. Figure 4.23 displays the according normalised area square roots of SFG-spectra evaluation from figure 4.22. As discussed earlier, SDS:DDPB monolayers are not very sensitive towards composition variation in the investigated interval. The according signal quotients $\mathrm{d}^+(\mathrm{h}_{25}\text{-SDS:DDPB}) : \mathrm{d}^+(\mathrm{d}_{25}\text{-SDS:DDPB})$ and $\mathrm{d}^+(\mathrm{d}_{25}\text{-SDS:DDPB}) :$

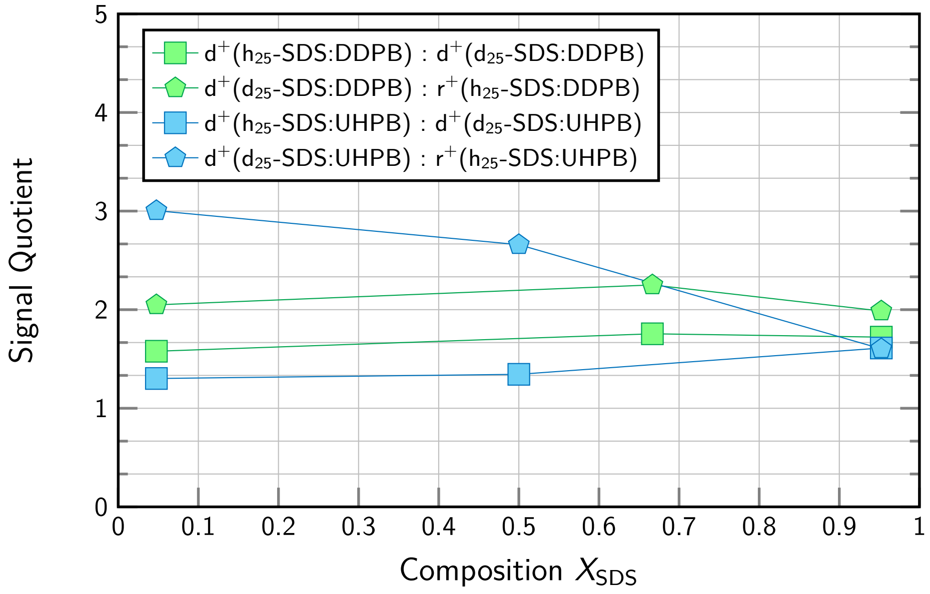

Figure 4.23.: Normalised area square roots corresponding to figure 4.22. Solid lines given as guide to the eye.

r$^+$(h$_{25}$-SDS:DDPB) amount to approximately $^5/_3$ and 2.

The SDS:UHPB surface layer, apparently varies a bit more with the bulk composition. However, the 1:20 mixture presumably produces a monolayer which is nearly equimolar. For that mixture, the above relations yield approximately $^4/_3$ and 3. Considering the respective complex stoichiometry, this implies that each bola molecule in the mixed adsorption layer contributes around three times as much to the total of the d^+ signal as the co-surfactant SDS. The relation between the bola d^+ and the SDS r^+ vibrational mode could also be used as a parameter for the composition if the geometry of the involved molecules does not change with composition. The values of 2 and 3 do not fit perfectly to the 2:1 and 1:1 stoichiometry, which might indicate a different angular distribution of the terminal methyl group in the mixtures. These considerations justify the postulated molecular geometry for the bolaamphiphiles, as shown in figures 4.21 and 4.1. Therein the average two-headed surfactant deviates at three separate sites from the all-trans geometry in its alkyl backbone, whereas the linear co-surfactant exhibits not significantly more than one Gauche-defect per molecule.

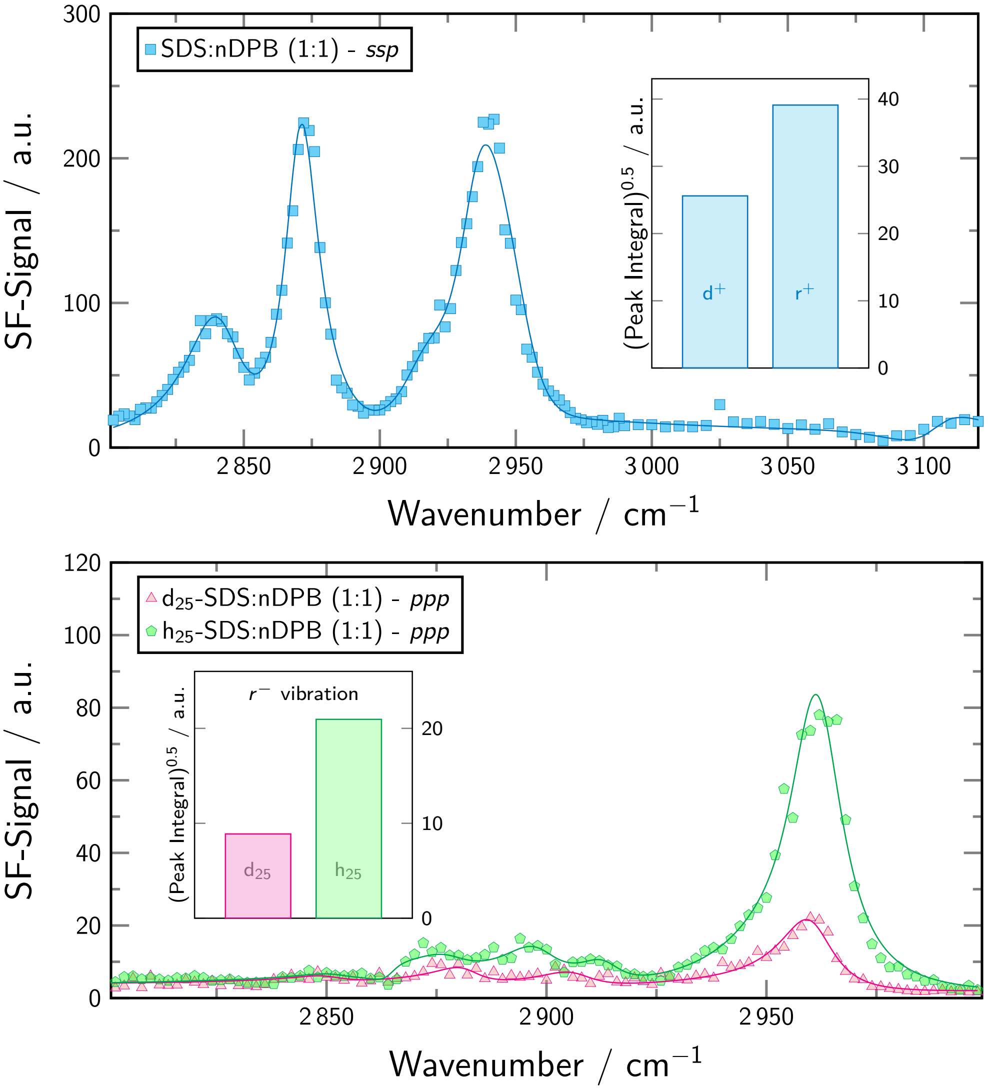

Figure 4.24.: SFG-Spectra of the SDS:nDPB (1:1) mixture in H_2O in the spectral range of CH-modes. Best fit functions given as solid lines. Results from the spectra deconvolution are displayed via bar chart insets. Top panel: *ssp* spectrum with comparison of the symmetric methyl and methylene stretching mode. Bottom panel: *ppp* spectra of mixtures containing either normal or perdeuterated SDS and the corresponding peak area square roots of the asymmetric methyl vibration.

For a complete picture, the mixed catanionic system of SDS and the linear cationic surfactant nDPB will be discussed briefly as well. Figure 4.24 exhibits the *ssp* and *ppp* SFG-spectra of a 1:1 mixture of SDS and nDPB in H_2O at a surface tension of $40\,\mathrm{mN\,m^{-1}}$. As can be seen by the low background intensity on the right side of the *ssp* plot, the surface charge is almost completely removed by mutual headgroup charge cancellation. The aromatic CH vibration at $3085\,\mathrm{cm^{-1}}$ manifests as a small dip in SFG-intensity, which is indicative for an excess of the anionic surfactant due to the destructive interference pattern. However, considering the small background intensity and the fairly low ionic strength of the solution ($I \simeq 1.4 \times 10^{-5}\,\mathrm{mol\,L^{-1}}$), this excess is most likely not significant.

The r^+ mode at $2870\,\mathrm{cm^{-1}}$ now towers over the less intense d^+ signal at $2840\,\mathrm{cm^{-1}}$. Accordingly, the r^+ Fermi resonance is the main feature in the region between 2900 and $2980\,\mathrm{cm^{-1}}$, with the d^+ Fermi resonance appearing only as peak shoulder around $2920\,\mathrm{cm^{-1}}$. The reversal in the rank order of r^+ and d^+ peak intensities, with respect to the previously discussed systems, is caused by close packing of the surfactant molecules in the mixed monolayer. As a consequence, alkyl tails are well aligned with only a few Gauche-defects. In addition, terminal methyl groups and their respective tilt angles are less randomly oriented, which also contributes to a high SFG-response.[149,150] As a result, the r^+ intensity increases and the d^+ mode decreases. The extent of that process is illustrated in the bar chart inset of figure 4.24. Spectra deconvolution revealed a r^+:d^+ relation that considerably leans towards the methyl side, which agrees well with the previous explanation.

For both mixtures shown in the bottom panel of figure 4.24, the *ppp* spectrum displays the asymmetric r^- mode as clearly resolved peak at approximately 2960 cm^{-1}, and only minor contributions from the r^{+}, d^{-} and Fermi resonance as weak signals at their usual centre frequencies. Upon deuteration of the mixture component SDS, the quadratic relationship between SFG-response and surface concentration causes the signal intensity to severely shrink down across the entire range of aliphatic CH vibrations. Spectra deconvolution revealed a relation between the respective r^{-} peak areas, which well agrees with the expected equimolar composition of the mixed SDS:nDPB monolayers, within the margin of experimental error.

4.2. Surface-active Adamantane Derivatives

4.2.1. Introduction to the system

Adamantane is the smallest example within the class of diamondoids. It consists of three cyclohexane chairs fused together to form a tricyclic molecule, where the carbon atoms are interconnected in the fashion of the diamond lattice. This rigid but at the same time strain-free cage-like structure leads to special physicochemical properties. Examples are low volatility, a high melting point, good thermal stability, and a pronounced hydrophobicity.[151,152] A great amount of work has been put into the functionalisation of adamantane in order to exploit its unique properties for different applications, especially in fields like material science, nanotechnology, supramolecular sciences and especially in pharmacy.[153–156] Concerning the latter, derivatives of adamantane are used as an antiviral agent or in the treatment of Parkinsonism or Alzheimer's disease.[157,158] Part of the pharmaceutical potency is expected to be due to their ability to interact with lipid membranes. However, the corresponding mechanism is not fully understood yet.[159–161] According to that, the characterisation of the adamantyl derivatives' amphiphilicity and their incorporation into self-assembled monolayers may be of great scientific interest. Until now, few studies focus on the surfactant properties of adamantyl derivatives.[162–164] In this work, amphiphilic compounds bearing an adamantyl cage as their main hydrophobic unit (cf. figure 4.25) are synthesised and investigated with respect to their surfactant character. Furthermore, mono-functionalised adamantyl derivatives are mixed with oppositely charged conventional surfactants. These catanionic mixtures are studied via means of tensiometry and vibrational SFG spectroscopy.

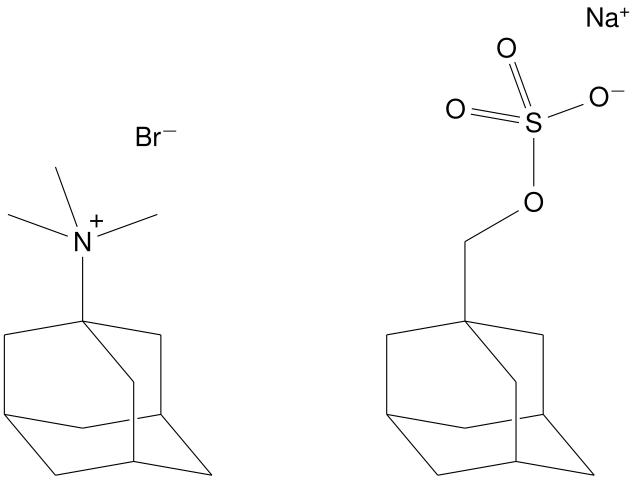

AdTAB SAdMeS

Figure 4.25.: Adamantane derivatives used in the context of this work.

4.2.2. Anionic Adamantane Amphiphile

4.2.2.1. Syntesis of Sodium 1-Adamantylmethylsulfate

1-Adamantanemethanol (99 %, Sigma) was dissolved in dry diethyl ether under nitrogen atmosphere. 1.1 equivalents of chlorosulfonic acid (99 %, Sigma) were first diluted with diethyl ether and subsequently added dropwise to the solution via a syringe through a rubber septum at 0 °C. During the reaction, a stream of nitrogen was lead through the liquid to remove evolving hydrochloric acid gas. After completion of the addition, the mixture was stirred for 30 min, allowing the solution to warm up to room temperature. The solvent was removed under vacuum and the solid sulfate ester was immediately neutralised with aqueous NaOH solution. The white precipitate was filtered off and recrystallised several times from water/ethanol to obtain highly pure product Sodium 1-Adamantylmethylsulfate (SAdMeS). Analytical data are listed below. For NMR-spectra cf. section A.1.

Sodium 1-Adamantylmethylsulfate (SAdMeS):

^{1}**H-NMR** (D_2O, 300 MHz, δ[ppm]): 3.46(s, 2H), 1.8(br-s, 3H), 1.53(dd, $^3J_H = 25.7, 12.4$ Hz, 6H), 1.38(s, 6H).

^{13}**C-NMR** (D_2O, 101 MHz, δ[ppm]): 78.9, 38.4, 36.4, 32.8, 27.8.

Elemental analysis: wt% found (calculated) for $C_{11}H_{17}SO_4Na \cdot 1.5\,H_2O$: C 44.7 (44.86), H 6.8 (6.795), S 10.8 (10.42).

4.2.2.2. Surfactant Properties of Sodium 1-Adamantylmethylsulfate

The concentration-dependent surface tension of an aqueous SAdMeS solution, together with two other curves, is given in the left panel of figure 4.26. The endpoint of the experimental data-set lies fairly close to the limiting solubility of the surfactant. In contrast to solutions of conventional surfactants, no breakpoint in the γ vs. $\log c$ curve can be observed before the onset of precipitation. This indicates the absence of micellar structures in solution. A possible explanation for that might be the rather short in length, albeit bulky structure of the alkyl residue, which prevents sufficient aggregation of the adamantyl moieties.

Another unexpected feature is its rather weak surface-activity, despite the eleven carbon atoms in the hydrophobic part of the molecule. To underline this finding, the graph of a conventional linear sodium alkylsulfate surfactant with the same number of carbon atoms in its alkyl tail (SUndS) is also given. The difference in surface-activity is expressed via the b parameter of the Frumkin fit or the pC_{20} value (cf. table 4.3). Latter is an empiric parameter for quantification of the surfactant efficiency, i.e. the amount of substance required to reduce the solvents surface tension by 20 mN m^{-1} (C_{20}) scaled as $-\log_{10} C_{20}$.[25] Due to the high concentration of SAdMeS, its activity in solution can be expected to deviate significantly from the concentration. Therefore, to obtain valid thermodynamic properties, a relation between the two quantities is needed.

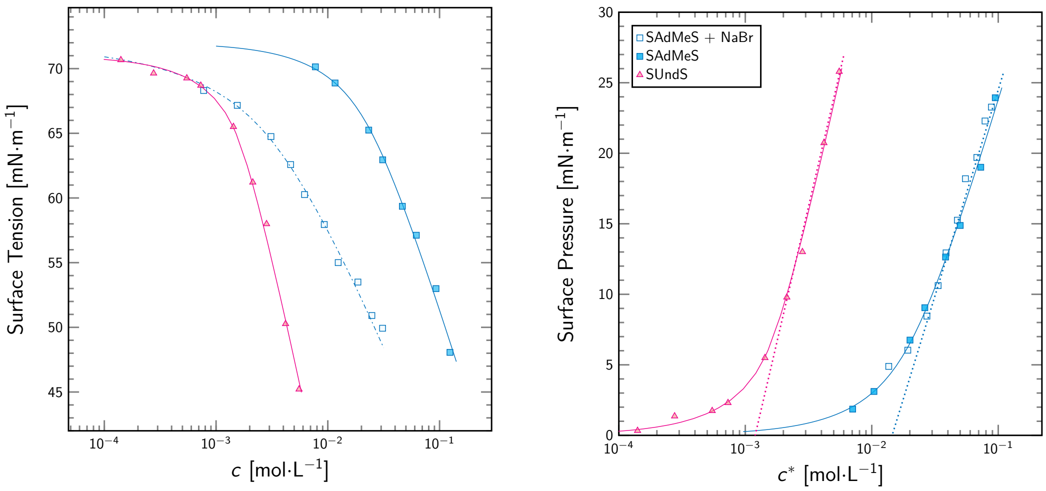

Figure 4.26.: Left: Surface tension of a SAdMeS solution in water and 0.5 mol L^{-1} NaBr (aq.) and Sodium undecylsulfate (SUndS) as a function of bulk surfactant concentration. Right: Both SAdMeS data sets coincide within experimental error, when plotted in terms of the surface pressure as function of the mean ionic activity c^*. Frumkin-type fitting functions are given as solid lines. Linear regression of the concentrated region given as dotted lines.

The adsorption of monovalent ionic surfactant RX in a solution of 1:1 electrolyte XY is reportedly governed by the mean ionic activity c^*, which is given by the following expression:

$$c^{*} = f_{\pm} \cdot (c_{\mathrm{R}^{\pm}} \cdot c_{\mathrm{X}^{\pm}})^{\frac{1}{2}} = f_{\pm} \cdot (c_{\mathrm{RX}} \cdot (c_{\mathrm{XY}} + c_{\mathrm{RX}}))^{\frac{1}{2}} \tag{4.17}$$

The mean activity coefficient $f_{\pm}$ in salt solutions up to a concentration of approximately $1\,\mathrm{mol\,L^{-1}}$ at room temperature (25 °C) can be calculated according to the extended Debye-Hückel model.[108,110]

$$\log f_{\pm} = \frac{0.5155 \cdot I^{\frac{1}{2}}}{1 + 1.316 \cdot I^{\frac{1}{2}}} + 0.055 \cdot I \tag{4.18}$$

I refers to the ionic product of the solution, which accounts for the individual ion concentrations c_i and the corresponding ion charge z_i.

$$I = \sum_{i} c_i \cdot z_i^2 \tag{4.19}$$

Only for values $I < 1\,\mathrm{mmol\,L^{-1}}$ the activity coefficient converges to 1, and thus c^{*} can be replaced by the bulk concentration c. In the above relations, the ionic activity linearly depends on the ionic product of the respective pair of surfactant and counterion rather than the concentration. Thus, the model not only allows to describe the binary mixture of surfactant RX and solvent but also solutions with additional electrolyte XY. The applicability of the model to the presented system can be checked by measuring a second solution with a swamping amount of added electrolyte ($500\,\mathrm{mmol\,L^{-1}}$ NaBr).

Upon the addition of salt, the overall slope of the SAdMeS curve is significantly flattened and shifted to the left. This is due to the salting-out effect of the indifferent electrolyte. When replotted as a function of the mean ionic activity c^{*} according to equation 4.17, the experimental data-sets collapse onto one master curve (cf. right panel of figure 4.26) in agreement with the

Table 4.3.: Fitting parameters according to the Frumkin model of ionic surfactants and the surfactant efficiency parameter pC_{20} for the curves shown in figure 4.26.

Surfactant	ω_0 [10^5 m^2 mol^{-1}]	b [m^3 mol^{-1}]	a	pC_{20}
SUndS	2.60	0.153	1.44	2.40
SAdMeS	3.58	0.020	1.00	1.05

above model. Note, that for high electrolyte concentrations, as in the present case, it is recommended to plot the surface pressure instead of the surface tension, to also account for the effect of the bare salt on the interfacial tension of the solvent.

From the limiting slope of the modified graphs, the minimum headgroup area can be estimated with the aid of Gibbs's relation. For SUndS it amounts to $0.49\,\mathrm{nm}^2$ and for SAdMeS to $0.65\,\mathrm{nm}^2$. This can be rationalised by the differences in length and cross-sectional area of the respective hydrophobic parts. On the one hand, if positioned upright, the branching within the adamantyl cage demands more space in the horizontal plane, as compared to the *n*-alkyl rest in all-trans geometry. On the other hand, the linear alkylsulfate molecules experience cohesive interactions along the entire length of their tails, which partially compensates the headgroup repulsion and helps to pack the molecules more densely within the monolayer. In contrast, the alkyl tail of the SAdMeS molecule can be regarded as an interconnected coil, which results in a less intense hydrophobic attraction between neighbouring molecules in the monolayer.

Another important parameter, when it comes to the performance of surfactants, are the foaming properties. Two exemplary systems of the previously discussed compounds with the same equilibrium surface tension are compared in figure 4.27. The conventional surfactant SUndS forms a rather stable foam

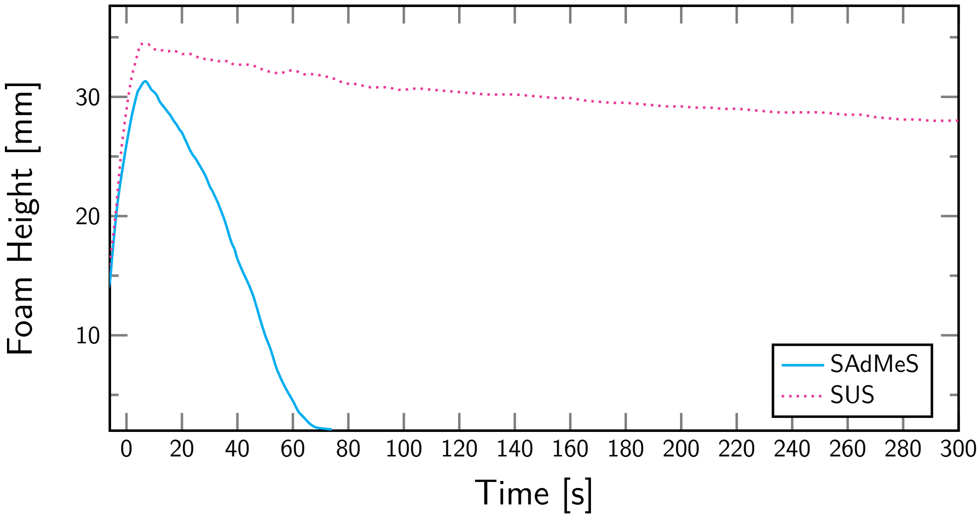

Figure 4.27.: Foam height of surfactant solutions as function of the time. The concentrations of SAdMeS (76 mN m^{-1}) and SUndS (5 mN m^{-1}) are chosen to yield a surface tension value of 52 ± 1 mN m^{-1}
.

network with a decrease of 20 % in foam height (in comparison to the maximum value) after 5 min effective life-time. The maximum foam height of SAdMeS solutions is only slightly smaller than for SUndS, but its foam stability, on the other hand, is dramatically weaker, which results in a complete collapse of the foam column within one minute. Considering the total ionic strength in the solutions, these differences may appear reasonable, since high concentrations of ions are reported to have a destabilizing effect on foam lamellae of ionic surfactant.[165,166] Repulsive forces between the two opposing charged monolayers of a foam lamella are diminished by the greater number of ions in the liquid volume, which allows the lamella to become thinner, leading to more fragile foam networks. However, it is questionable, if this is the only effect responsible for SAdMeS's weak foam stability. Another important factor might be the structure of the alkyl residues, allowing for different energy dissipation mechanisms during lamella disturbances.

4.2.2.3. Mixtures between Anionic Cage-like Sufactant and Cationic Linear Surfactant

As shown above, SAdMeS alone is an inferior surfactant compared to its straight chain analogue. However, in combination with the oppositely charged surfactant dodecyltrimethylammonium bromide (DTAB), a significant synergistic effect can be observed. DTAB (Sigma, >99%) was recrystallised twice from water/ethanol prior to usage to remove possible contaminants from the commercial product. Figure 4.28 displays the surface tension isotherms of the mixed catanionic systems of linear plus cage-like surfactant. In the left panel, the abscissa refers to the concentration of the linear component instead of the total concentration to maintain clarity.

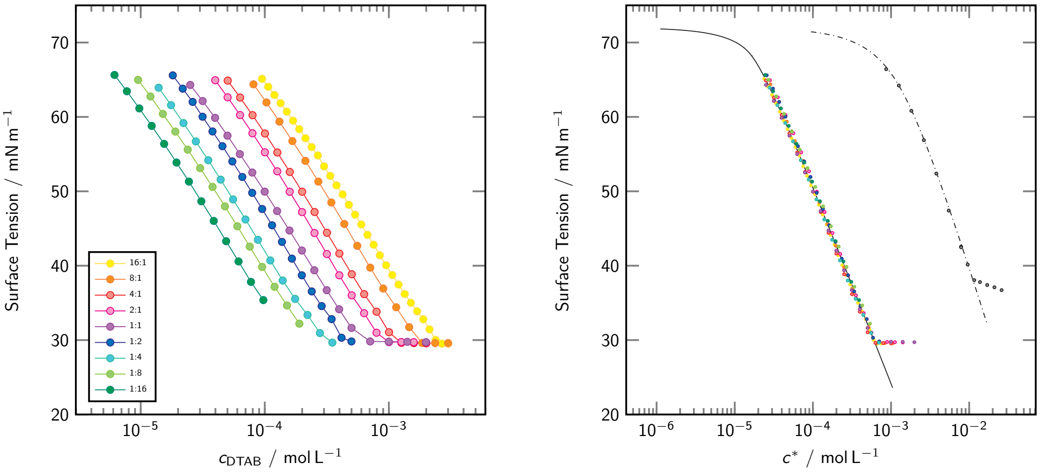

Figure 4.28.: Left: Isotherms of DTAB:SAdMeS mixtures in different bulk compositions. Note that the abscissa refers to the DTAB concentration. Right: Data rescaled with respect to the mean ionic product $c^* = (c_{\mathrm{DTAB}} \cdot c_{\mathrm{SAdMeS}})^{\frac{1}{2}}$. For comparison data of pure DTAB is also given as function of $c^* = f_{\pm} c_{\mathrm{DTAB}}$. Frumkin-type fitting functions given as solid line.

To start with, the SAdMeS-rich mixtures (1:16, 1:8, 1:4) reached the solubility limit before a kink in the graph could be observed. Beyond their respective cmc, mixtures with an equimolar composition or excess DTAB achieved a plateau value of $\gamma_{cmc} \simeq 30\,\mathrm{mN\,m^{-1}}$. Additionally, all shown γ_e vs. $\log(c_{\mathrm{DTAB}})$ curves are nearly parallel to each other and exhibit a more or less linear dependence below a value of $60\,\mathrm{mN\,m^{-1}}$ until the cmc is reached. Similar to the catanionic mixtures presented in the previous chapter, the surface tension curves collapse onto one curve when plotted as a function of the surfactant-only ionic product c^*. Comparison with the isotherm of sole DTAB (cf. right panel of figure 4.28) reveals a significant synergistic effect in the surfactant mixtures, represented by a difference in the Frumkin parameter b of factor 25 and a 1.71-fold increase of the surfactant efficiency parameter pC_{20} (cf. tables 4.4 and 4.5) for the stoichiometric 1:1 mixture. Additionally, the surface tension at the cmc is significantly shifted to lower values by almost $8\,\mathrm{mN\,m^{-1}}$ for the catanionic mixtures compared to the bare DTAB solution. All these criteria speak for a strong complex formation between DTAB and SAdMeS. Its implications for the surface layer are discussed below.

Table 4.4.: Fitting parameters according to the Frumkin model for the curves shown in figure 4.28. Data corresponds to c^* for the 1:1 mixture and to the real concentration c for DTAB. a: Literature data taken from ref. [110] for comparison.

Surfactant	ω_0 [10^5 $\mathrm{m^2\,mol^{-1}}$]	b [$\mathrm{m^3\,mol^{-1}}$]	a
DTAB	3.3, 3.6^a	0.38, 0.21^a	0.80, 1.3^a
DTAB:SAdMeS	4.2	9.75	1.8

Table 4.5.: Characteristic parameters for the surfactant systems shown in figure 4.28. Data corresponds to c^* for the 1:1 mixture and to the real concentration c for DTAB.

Surfactant	pC_{20}	cmc [$\mathrm{mol\,L^{-1}}$]	γ_{cmc} [$\mathrm{mN\,m^{-1}}$]	$A_{\min}$ [$\mathrm{nm^2}$]
DTAB	2.39	$1.16 \cdot 10^{-2}$	38.1	0.63
DTAB:SAdMeS	4.10	$5.87 \cdot 10^{-4}$	30.3	0.72

As indicated by the collapse of the surface tension isotherms onto a single curve upon rescaling to c^* (cf. figure 4.28), the double-logarithmic plot of the surfactant concentrations, required to produce a given surface pressure, delivered slopes very close to -1 (cf. right panel of figure 4.29). This implicates, that within the examined compositional regime, γ is almost entirely determined by the ionic product of an- and cationic surfactant, with a minor influence from the NaBr, or even the respective surfactant:counterion pairs.

In the left panel of figure 4.29), the total ion concentration as a function of the DTAB mole fraction in the binary mixture is shown for three different surface tension values. All curves exhibit a more or less symmetric course around the minima at the equimolar composition $\hat{X}_{\mathrm{DTAB}} = 0.5$, where the synergism appears to be strongest. To deduce the surface layer composition from the experimental data, the method of Aratono[78] was exerted with these data-sets. The findings agree with the results so far. A fit to equation 4.7, as discussed in the previous section, assuming a constant surface composition could satisfyingly describe the experimental data. Thus, $\hat{X}^{\sigma}_{\mathrm{DTAB}}$ was found to be constant within experimental error at 0.51 ± 0.01 for the mixtures between 16:1 and 1:16.

The foaming behaviour of the stoichiometric surfactant composition 1:1 was investigated with respect to the bulk concentration (cf. figure 4.30). The samples in the sub-micellar concentration regime contained surfactant amounts to yield 60, 50 and 40 $\mathrm{mN\,m^{-1}}$ in surface tension, according to the tensiometry results. Additionally, a sample with 1.5 × cmc was investigated as well. For the sub-micellar samples, the foamability, i.e. the foam volume created after 30 s of bubbling time is slightly increasing with the surfactant concentration. However, crossing the cmc induces a boost in the foamability. For all samples, the initial foam height is kept for a certain amount of time, until the foam

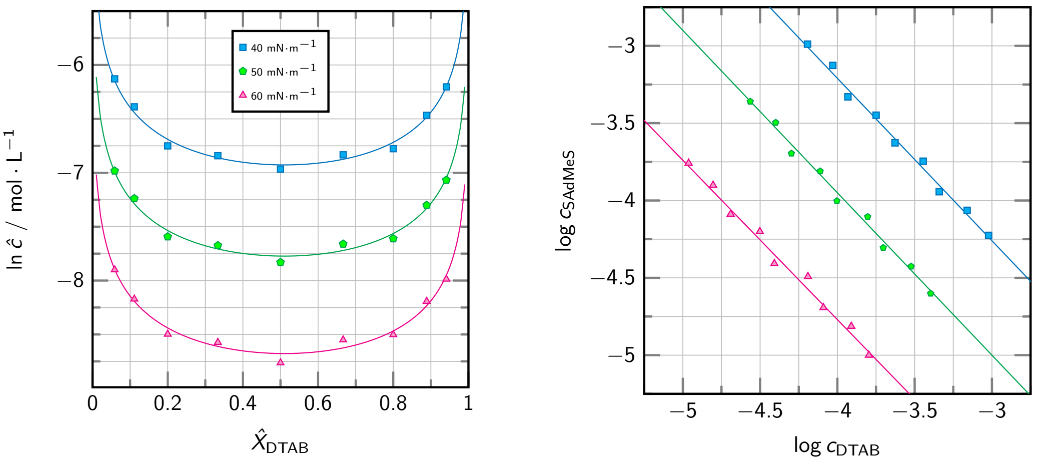

Figure 4.29.: Left: Total ion concentration $\hat{c}$ as function of the bulk mole fraction of DTAB determined at 40, 50 and 60 mN m^{-1} surface tension. Solid lines according to equation 4.7. Right: Corresponding concentrations in bi-logarithmic representation. Linear functions with slope -1.05, -1.05 and -1.03 are given as guide to the eye.

lamellae start to rupture. The threshold time for that to happen increases with concentration. Unfortunately, the reproducibility in the decay curves was rather poor, as shown by the huge shaded error regions. This is due to its collapsing behaviour, which was characterised by a stepwise rupture of the lamella framework.

This observation is most likely to the preferential adsorption of the catanionic complex. As will be shown later on, the mutual cancelling of the respective headgroup charge leads to the absence of significant surface potential. Upon drainage of a big fraction of the initially entrapped liquid, the lamella becomes very thin, due to the lack of electrostatic repulsion between the opposing adsorption layers in the confined environment. Thus, very fragile films are created, which tend to collapse more easily upon any mechanical disturbance, e.g. rupture of a neighbouring lamella. The boost in foamability above the cmc can be ascribed to the presence of large aggregated structures in solution. Such

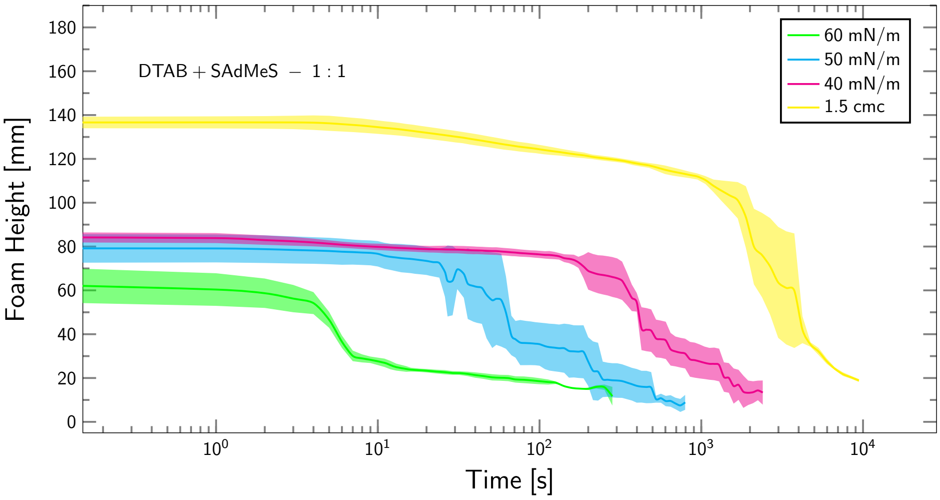

Figure 4.30.: Mean foam column height as function of time after achieving the maximum value. Every measurement was repeated at least three times. Error interval given as shaded region. Bubbling time was 30 seconds.

colloidal molecular conglomerates were verified by dynamic light scattering (cf. figure 4.31). It has been shown in the past that foam could be stabilised by catanionic mixtures beyond the aggregation threshold concentration.[167–170] These systems provide several factors which all contribute to high foam stability. First, bulk concentrations are fairly low, despite a high surface concentration. This might help to sustain a surface tension gradient and promote self healing of the film.[171] Secondly, the formation of the catanionic complex allows for large and elongated aggregate structures, which slows down the film drainage by increasing the liquid viscosity.[172]

4.2.2.4. Spectroscopic Study of Anionic Adamantane Surfactant

Figure 4.32 displays the *ssp*-polarised SFG-spectra of the surface-active compounds DTAB, SAdMeS and SDS (already shown and discussed in section 4.1.5.2). The respective bulk concentrations all lead to a comparable height in the peak tail of water modes. In comparison with the spectra from the earlier

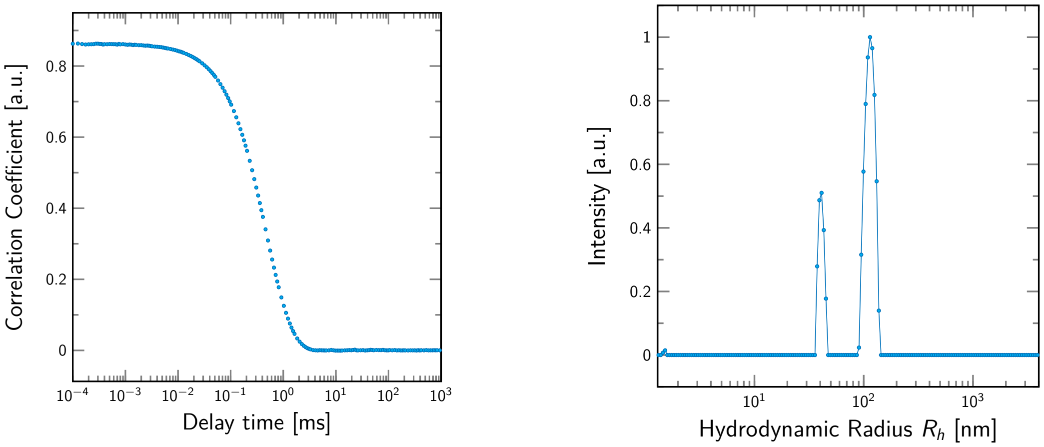

Figure 4.31.: Dynamic light scattering of 1:1-mixtures of DTAB:SAdMeS ($c = 1.5\times$ cmc). Left: Correlation function. Right: Size distribution of the hydrodynamic radius according to the Stokes-Einstein relation.

discussed surfactant nDPB, DTAB differs in the absence of a signal around 3080 $\mathrm{cm^{-1}}$. Apart from that, their appearance is quite similar with equal peak positioning. In analogy to the previous discussions, CH-spectra of cationic and anionic surfactant species are oppositely influenced by the water background, which leads to higher effective intensities on the left side of the DTAB spectrum and, vice versa, to low SFG-signal intensity for the two anionic species. The spectra of SAdMeS does not display a significant peak at 2875 $\mathrm{cm^{-1}}$, due to the lack of methyl groups. However, between 2890 and 2975 $\mathrm{cm^{-1}}$, the spectrum reveals a feature with maximum around 2920 $\mathrm{cm^{-1}}$. An as pronounced signal could not be observed in the linear surfactant's spectrum, and thus be used for the identification of SAdMeS in mixed surfactant systems. A more extensive discussion on the origin of the individual signals is given below.

Figure 4.33 shows the SFG-spectra of certain DTAB:SAdMeS-mixtures recorded under different polarisation schemes (*ssp, ppp, sps*). The bulk concentration was chosen to yield 40 $\mathrm{mN\,m^{-1}}$, according to the above surface tension data. No significant intensity is observed on the right side of the spectra,

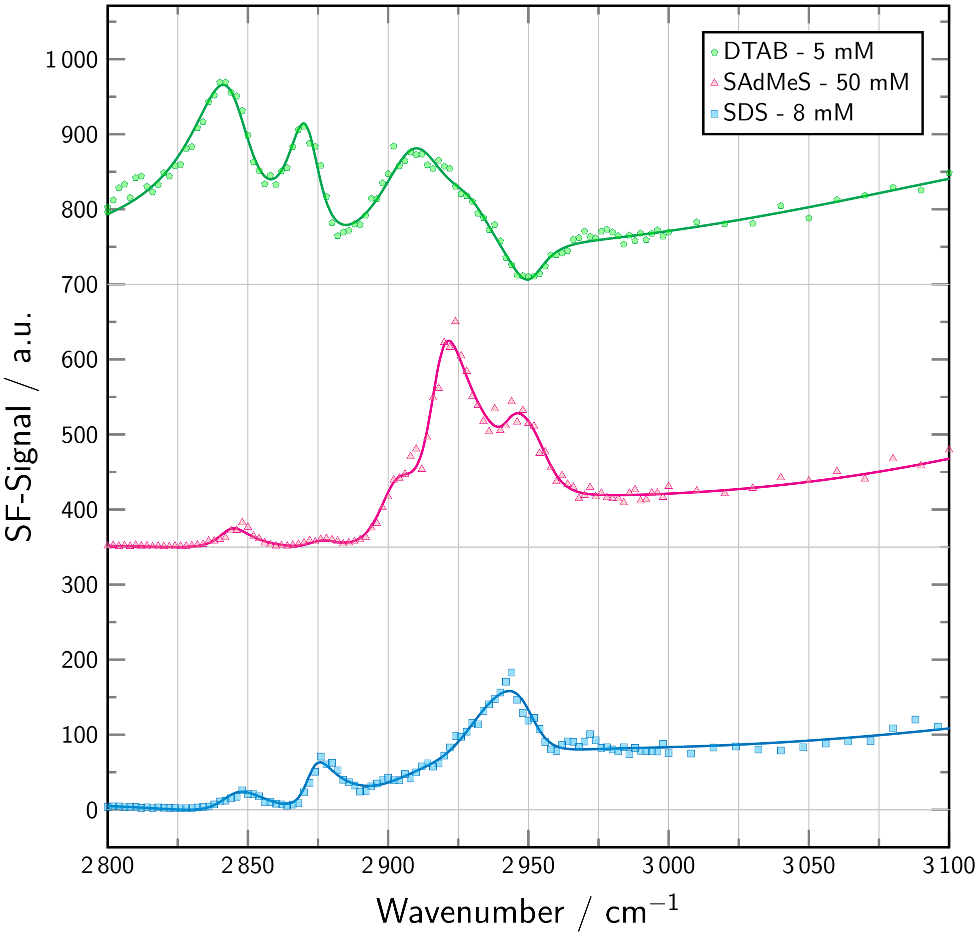

Figure 4.32.: SFG-Spectra of DTAB (5 mmol L^{-1}), SDS (8 mmol L^{-1}) and SAdMeS (50 mmol L^{-1}) in *ssp* polarisation in the overlapping spectral regime of CH and OH vibrational modes.

indicating vanishing excess charge, and thus, equimolar surface composition. The *ssp*-spectra for the three different mixtures show the usual spectral features for the d^+ and r^+ vibrational mode. From first glance, their intensity compares to each other within one spectrum, however, the observed absolute maximum SFG-intensity decreases from the 16:1 to the 1:16 composition. The obvious peaks in the region between 2900 and 2960 cm^{-1} can be fitted with a triplet of signals at 2900, 2918 and 2940 cm^{-1} and also require a signal in opposite phase at 2955 cm^{-1} to obtain a good agreement with the experimental data.

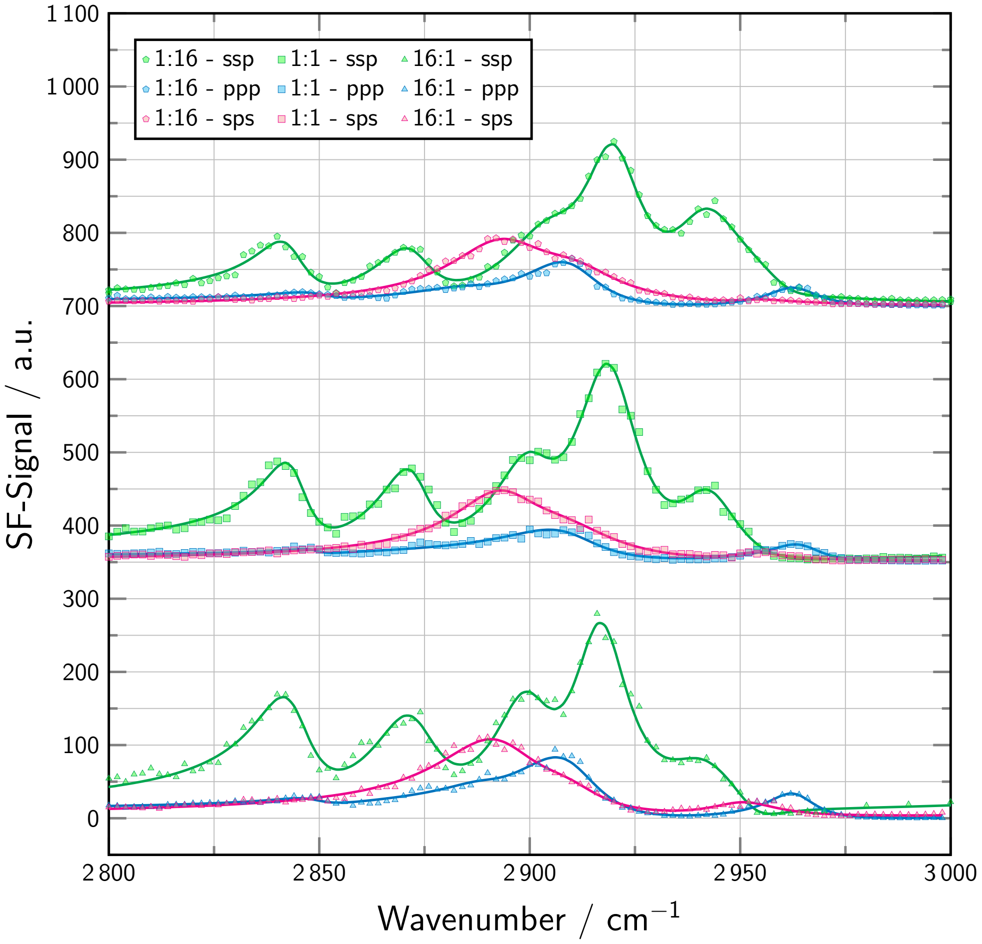

Figure 4.33.: SFG-spectra (*ssp, ppp, sps*) of DTAB:SAdMeS mixtures in the spectral regime of CH-vibrations. Spectra are offset for clarity. Best fit to the spectra are given as solid lines.

Background signals due to water aligned by excess charge were simulated with a constructive interfering signal of varying peak strength centred at 3300 cm^{-1} with fixed peak broadening Γ_w of 200 cm^{-1}. The asymmetric methyl stretching mode r^-, especially visible in *ppp* polarisation, can be found at 2962 cm^{-1}. Both, *sps* and *ppp* spectra exhibit a broad feature in the region between 2880 and 2925 cm^{-1}, whereby the *sps* spectra, with a maxima at 2893 cm^{-1}, surpass the *ppp* spectra, with a maxima at 2907 cm^{-1}, in intensity. These features can be ascribed to the asymmetric methylene stretching, and presumably, in the case of the *ppp* spectra, also the methine mode.[83]

As shown in figure 4.34, the fitting procedure unveiled that the differences in the shape of the *ssp*-spectra, i.e. the decrease of the shoulder at 2900 cm^{-1} and the intensity increase around 2940 cm^{-1} with increasing SAdMeS content, can be explained by the receding water contribution, rather than a significant change in the CH-peak intensities.

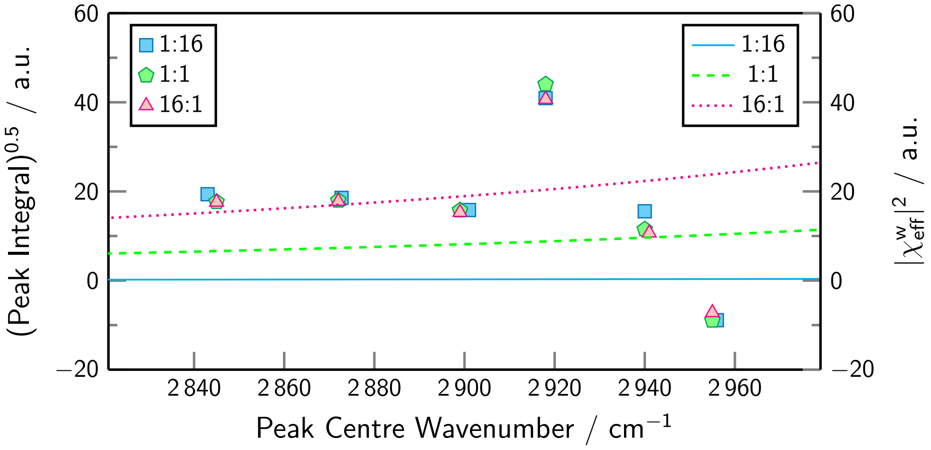

Figure 4.34.: Fitted peak area square root with peak centre frequency corresponding to the *ssp* spectra in figure 4.33 are given as symbols (left axis). The frequency-dependent water background contribution $|\chi_{\mathrm{eff}}^{w}|^2$, as obtained from spectra deconvolution, is given as solid line in the same colour scheme (right axis). Note that the respective ordinates refer to different quantities.

As discussed before, the SFG-spectrum is extremely sensitive towards electric fields generated by charge-excess within the surface layer. The observed changes in the water SFG-contribution can be ascribed to subtle variations of the surface composition and bulk ionic strength for the different surfactant mixtures. Apart from that, however, the CH-vibrations maintain their oscillator strengths within the estimated experimental error. Therefore, one can assume a near-constant surfactant monolayer composition within the investigated concentration window.

As shown by the peak deconvolution, contributions from d^+ and r^+ vibrational modes to the SFG-spectrum are nearly equal. Considering, that DTAB, as shown in figure 4.32, itself shows a d^+/r^+ signal ratio $\simeq 1.25$, and the fact that the pure SAdMeS-spectrum also possesses d^+ modes, one can assume a certain ordering effect of the cage-molecule on the tails of the quaternary ammonium surfactant. This effect can be rationalised via a simple geometric picture. Assuming that the headgroups are densely packed and their respective nitrogen and sulfur atoms are anchored in the same plane, the rigid adamantyl framework may help to support the all-trans geometry of the dodecyl-tail, up until half of its total length (cf. figure 4.35). Thus, the possibility for SFG-active methylene units in the linear surfactant is reduced, especially in its lower half.

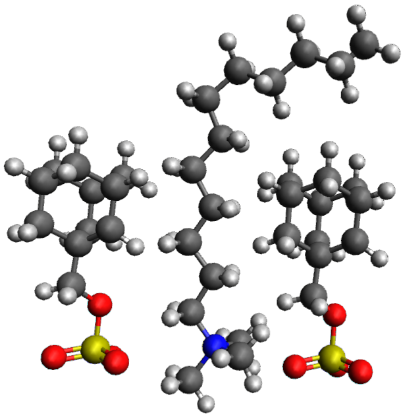

Figure 4.35.: Scheme a of cationic dodecyltrimethylammonium sufactant backbone supported by rigid anionic adamantylmethylsulfate co-surfactants in a monolayer.

A feature, that has not been observed for the systems in the previous section, is the huge peak at 2918 cm^{-1}. In the literature, signals in that particular region are ascribed to the Fermi resonance of methylene modes, but an intensity as observed, especially with respect to the d^+ mode at 2845 cm^{-1}, can be regarded as unusual, and its assignment has to be reconsidered here.

A possible additional contribution to the SFG-spectrum might originate from the three bridging CH units of the adamantane cage. In the literature, only a few examples discussing the methine stretch of sp^3-hybridised tertiary carbon can be found within the context of SFG-spectroscopy.[173–176] In these publications, however, the spectral assignment of that particular vibration appears to be rather ambiguous, due to its weak SFG-activity and the proximity to other vibrational modes. Ji and Shen[177] ascribed a signal at 2902 cm^{-1} to the methine stretching mode of interfacial adsorbed leucine molecules. The chemical environment consisting of solely aliphatic hydrated carbon is very similar in the adamantane cage. Thus, the signal around 2900 cm^{-1} is likely to contain contributions from the methine modes, if the authors' assumption is correct. Lu and Wang[131] located the CH-resonance of isopropanol at 2914 cm^{-1}. They discussed the difference to the peak centre frequencies, usually found around 2900 cm^{-1} in IR- and Raman experiments, and argued that the OH-function in direct vicinity to the CH-group might be responsible for the relative blue-shift. Following these considerations, the signal around 2918 cm^{-1} must include additional SFG-contributions.

A possible candidate here might be an asymmetric methylene stretching mode. Different authors have independently assigned signals around 2920 cm^{-1} to the d^- mode in *ssp* polarisation.[177–182] However, comparison with *ppp* and *sps* spectra speaks against that hypothesis. The intense peak in *ssp* polarisation is located at higher wavenumbers, which indicates, according to the polarisation selection rules,[83,131] that the respective peak is not due to the d^- mode. It might be possible that the framework of the adamantyl moiety enables coupled motions of several CH groups in the interconnected rings that lead to nondegenerate methylene stretches.[183] Another possibility may be the isolated CH_2 group between the cage and the headgroup which might experience a spectral shift and/or signal splitting due to its position in the molecule.

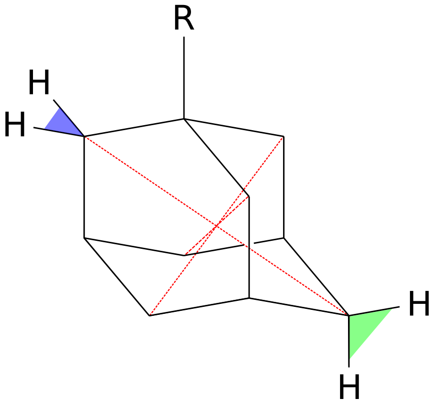

Figure 4.36.: Architecture and structural relation in the adamantyl cage. The planes defined by the HCH angles of the opposing methyl units (green and blue areas) are perpendicular to each other (D_{2d} pointgroup symmetry).

In the adamantyl rest none of the methylene groups is in direct connection to another methylene group. At first glance this should render all of the six respective units SFG-active since they do not share an inversion centre with their immediate neighbours. However, when the molecule is viewed as a whole, one finds three pairs of CH_2 units, where the respective dipole moments point in opposite direction (cf. figure 4.36). This degree of symmetry is responsible for a rather small contribution of the d^+ modes from the adamantane cage, considering the actual number of isolated methylene units in the molecule. At this point it should nonetheless be stated that even molecules, which are assumed to exhibit total internal inversion symmetry, such as the octahedral complex potassium ferrocyanide[184] or the aromatic benzene,[185] have been reported to produce SFG signals, due to the symmetry reducing effect of the asymmetric force field at the interface.

For the d^- vibration the situation is quite different. The opposing methylene pairs are arranged with a relative 90° twist angle, similar to the CH-configuration in an allene molecule. Therefore the transition dipole moments of the respective d^- modes of the opposing groups lie in different planes. Hence, the methylene units in the adamantyl moiety can be expected to produce a significant signal from asymmetric vibrations, depending on the actual molecular orientation and polarisation combination.

Furthermore, the cage exhibits three methine units per molecule arranged in a C_{3v} geometry analogous to a methyl group. One can assume that (co)adsorption at the interface forces the point group axis to be aligned more or less perpendicular to the surface plane. Therefore methine units possess a net orientation, which should lead to a detectable SFG-response, despite the small reported SFG-sensitivity of methine groups.[83] However, due to strong overlap in that spectral region, the methine and the d^- vibration can not be distinguished from each other.

In conclusion, although they possess significant differences in surface-activity, mixtures of SAdMeS and the oppositely charged linear surfactant DTAB in the range from 16:1 to 1:16 can be expected to form nearly electroneutral composed monolayers at the air water interface. This was verified by the maintained SFG-intensity distribution for the different CH-vibrational modes and the small intensity by aligned interfacial water. The latter is slightly increasing with the DTAB content which suggests a little, but recognisable, excess of the cationic compound. By the introduction of the adamantyl surfactant in into the DTAB monolayer, new spectral features like the intense d^- feature in *sps* polarisation, the methine mode in *ppp* and *ssp* spectra and the huge peak in the Fermi resonance region, can be observed, which may be used for the species identification of adamantyl surfactants in future work.

4.2.3. Cationic Adamantane Amphiphile

4.2.3.1. Synthesis of Adamantyltrimethylammonium Bromide

Amantidin hydrochloride (Sigma, > 98 %) was dissolved in water and solid NaOH was added in small portions. Subsequently, the precipitate was filtered off, washed with cold water and dried under vacuum. The intermediate product was then dissolved in isopropanol and 5 equivalents of formic acid were added slowly at 60 °C. To this mixture, 4 equivalents of formaldehyde were added dropwise at 60 °C and stirring was continued overnight under reflux. To this mixture NaOH solution (25 wt.%) was added until phase separation occurred. The organic phase was separated and the aqueous phase was extracted three times with dichloromethane. The organic phases were combined, washed with saturated KCl solution and dried with $NaSO_4$. The solvent was removed under vacuum and the oily liquid was distilled at 125 °C under reduced pressure (30 mbar) to obtain the intermediate product N,N-Dimethyl-(1-adamantyl)amine (AdDMA).

AdDMA was dissolved in isopropanol and 1 equivalent of iodomethane was added. The stirring of the mixture was continued for 5 h under reflux. The white precipitate was filtered off, dried under vacuum and recrystallised from a methanol/acetone mixture. A glass column loaded with anion exchange resin (Amberlite-402(Cl), Alpha Aesar) was used to remove iodide and introduce bromide as the counterion. To do so, the resin was properly prepared by sequential elution with water, NaOH solution (10 wt.%), water, KBr solution (20 wt.%), water and finally methanol (in that particular order). The iodide salt was dissolved in methanol and slowly eluated. The eluate was dried under vacuum and the obtained white solid was recrystallised in a methanol/acetone mixture. Drying under vacuum yielded the pure final product adamantyl trimethylammonium bromide (AdTAB). Analytical data are listed below. For NMR-spectra cf. section A.1.

N,N-Dimethyl-(1-adamantyl)amine (AdDMA):

^{1}H-NMR ($CDCl_3$, 400 MHz, δ[ppm]): 2.10(s, 6H), 1.91(br. s, 3H), 1.52(br. s, 6H), 1.46(m, 6H);

^{13}C-NMR ($CDCl_3$, 101 MHz, δ[ppm]): 53.4, 37.9, 36.9, 36.8, 29.5.

1-Adamantyltrimethylammonium bromide (AdTAB)

^{1}H-NMR (D_2O, 400 MHz, δ[ppm]): 2.85(s, 9H), 2.18(br. s, 3H), 1.93(d, 6H, $^{3}J_{H} = 2.3$ Hz), 1.56(dd, 6H, $^{3}J_{H} = 12.3, 30.1$ Hz).

^{13}C-NMR (D_2O, 100 MHz, δ[ppm]): 72.7, 47.6 (t, $^{1}J_{CN} = 4.0$ Hz), 34.5, 34.2, 30.0.

Elemental analysis: wt.% found (calculated) C: 57.1 (56.9), H: 8.3 (8.8), N: 5.0 (5.1).

4.2.3.2. AdTAB as Co-Surfactant

In this section, the surface adsorption characteristics of the cationic adamantane derivative AdTAB will be discussed. Measurement of the concentration-dependent surface tension of AdTAB revealed a rather weak surface-activity (cf. figure 4.37). In order to obtain a value significantly different from $72\,\mathrm{mN\,m^{-1}}$, dimensions of $1\,\mathrm{mol\,L^{-1}}$ substance had to be dissolved. Thus, referring to AdTAB as a proper surfactant might be quite an exaggeration. Typically, such high concentrations are rather observed with so-called hydrotropes like sodium

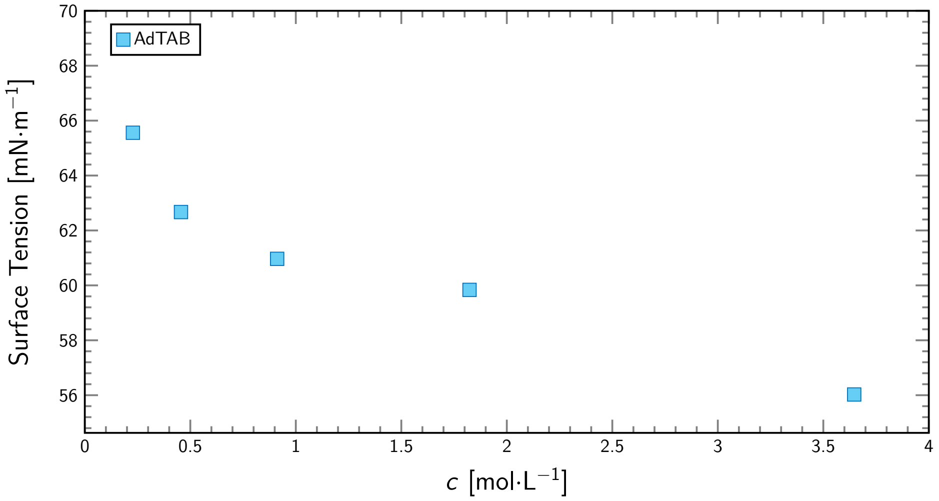

Figure 4.37.: Surface tension of AdTAB solutions as function of the bulk concentration.

xylene sulfonate.[186] This class of amphiphilic molecules is known to be unable of forming discrete micellar aggregates on its own. However, they can build some loose structuring in solution and facilitate the mixing of two otherwise immiscible components. In combination with co-surfactants, ionic hydrotropes have been used to tailor the shape of the mixed micelles.[187–189] In accordance, the influence of AdTAB on adsorption layers of oppositely charged SDS will be investigated in the following section.

Figure 4.38 shows the concentration dependant surface tension for the mixed SDS:AdTAB solutions, as a function of the bulk SDS concentration. Analogous to the previously discussed system of linear surfactant plus cage amphiphile, the addition of the oppositely charged additive shifts the curve towards smaller concentrations. However, this effect is less pronounced than observed before. To be more specific, the required C_{12}-surfactant concentration to achieve $40\,\mathrm{mN\,m^{-1}}$ in a 1:1 mixture is reduced by a factor 0.025 for DTAB:SAdMeS and around 0.1 for SDS:ADTAB. Additionally, only a minor reduction in the surface tension at the cmc of 1-2 $\mathrm{mN\,m^{-1}}$ can be observed.

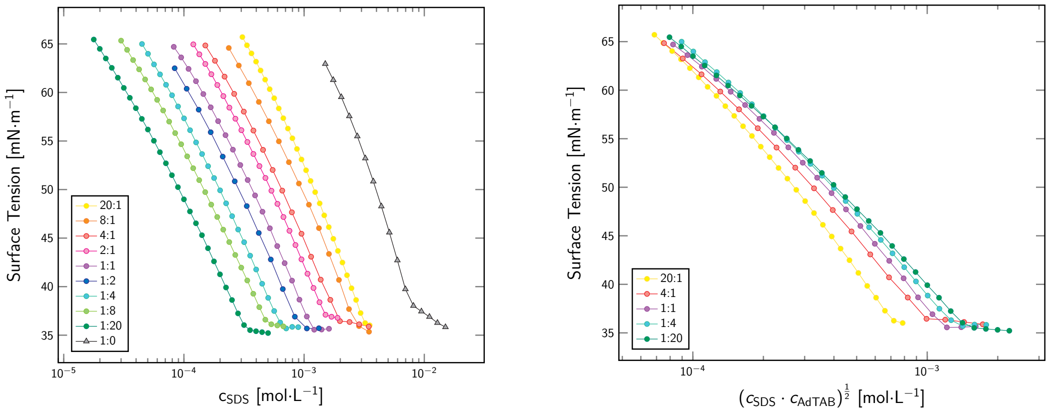

Figure 4.38.: Left: Isotherms of SDS:AdTAB mixtures in different bulk compositions. Note that the abscissa refers to the DTAB concentration. Right: Corresponding data plotted as function of the ionic product of both organic ions. For clarity, only every second composition is shown.

Plotting the surface tension as a function of the ionic product of the organic salt combination $(c_{\mathrm{SDS}} \cdot c_{\mathrm{AdTAB}})^{1/2}$ yields a result which differs from the previously analysed systems. This time the curves do not collapse onto a single master function. Instead, the graphs appear to converge at high surface tension but vary in a monotonous fashion for concentrations near the cmc. The respective graph appears to be more extensively curved to the right if the sample contains AdTAB to a lesser extent. This fact is also mirrored in the minimum molecular area, as determined from the limiting slope of the isotherm via the Gibbs relation (cf. figure 4.39). In the present case, a stoichiometry factor of $n = 2$ accounts for the dissociation of surfactant in the monolayer, regardless of which ion type serves as counterion, i.e. co-surfactant or inorganic ion.

Starting from a very similar value as for the DTAB:SAdMeS mixture, the area demand decreases with increasing SDS proportion in solution. A possible explanation for that behaviour is the gradual expulsion of the cage-amphiphile from the monolayer, which means deviation from the electroneutral

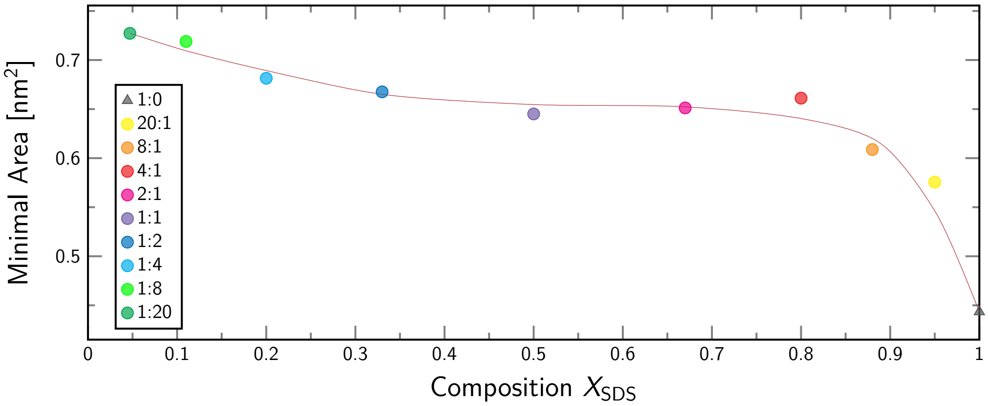

Figure 4.39.: Minimal molecular area, calculated from the limiting slope of the surface tension plots (cf. figure 4.38) via the Gibbs equation accounting for 1:1 stoichiometry. Solid line given as guide to the eye.

stoichiometry in the adsorption layer. However, the sudden step between the 20:1 and the 1:0 samples, indicates that there is still a certain preference for the catanionic complex in the monolayer instead of the anionic surfactant (plus counterion). Note, that the change in the slope could not be rationalised by simply treating AdTAB as indifferent electrolyte and SDS as the actual surfactant. According to equation 4.17 stoichiometric amounts of salt ($c_{\mathrm{XY}} = a \cdot c_{\mathrm{RX}}$) only introduce a factor $c^* = f_{\pm} c_{\mathrm{RX}} \cdot \sqrt{a+1}$, and thus leave the slope $\frac{d\gamma}{d \ln c_{\mathrm{RX}}}$ unaffected. In the present case solutions are still very dilute and activity corrections can be neglected since $f_{\pm} \simeq 1$.

The double-logarithmic mapping of the individual amphiphile concentrations at surface tensions of 60, 50 and 40 $\mathrm{mN\,m^{-1}}$ yields linear functions with slopes of -0.69, -0.77 and -0.84, which obviously is significantly different from -1. Therefore, one can conclude a considerable variation and asymmetry in the surface composition, which consequently implies non-negligible co-adsorption of inorganic counterions for compensation of the excess charge. To sum up, the effect of AdTAB on SDS can not solely be described by charge screening in the vein of an indifferent electrolyte, nor by catanionic complex formation with a preferred surface stoichiometry, but rather as a combination of the two effects. Similar to these findings, significant deviation from the electroneutral composition has been reported for other catanionic mixtures, where the individual surfactants exhibit a considerable mismatch in solubility.[113,190,191]

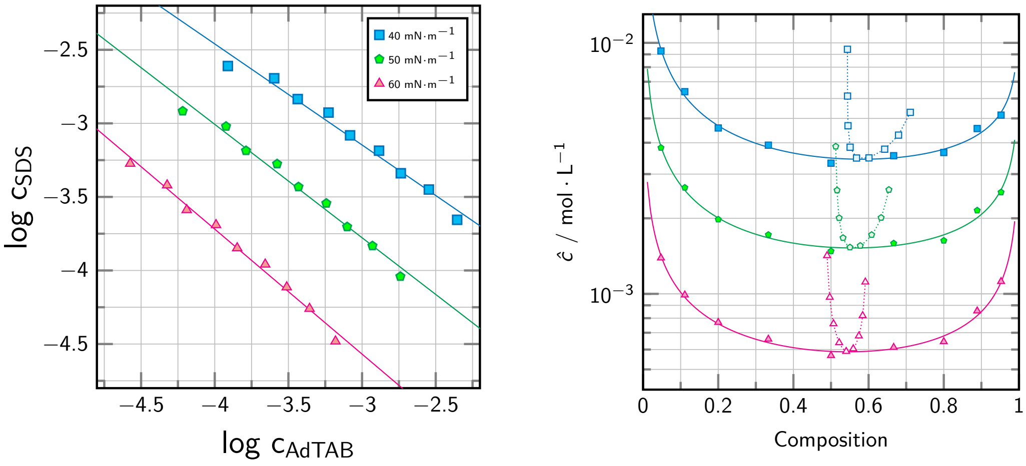

Figure 4.40.: Left: Individual surfactant concentrations required to yield surface tensions of 40, 50 and 60 mN m^{-1}. Linear fitting function given as guide to the eye. Right: Total ion concentration as function of the bulk composition $\hat{X}_{\mathrm{SDS}}$ (filled symbols). Fitting functions according to equation 4.21 given as solid lines. The derived surface composition $\hat{X}^{\sigma}_{\mathrm{SDS}}$ is given as open symbols.

The approach of Aratono was applied for the estimation of the amount of AdTAB in the mixed monolayer. In order to account for the variation in the surface composition, the expression $\hat{X}^{\sigma}_{\mathrm{SDS}}(\hat{X}_{\mathrm{SDS}})$ was approximated with a monotonous third-order polynomial $(A, B, C, D \geq 0)$ in the investigated concentration regime.

$$\hat{X}^{\sigma}_{\mathrm{SDS}} = A\hat{X}^{3}_{\mathrm{SDS}} + B\hat{X}^{2}_{\mathrm{SDS}} + C\hat{X}_{\mathrm{SDS}} + D \tag{4.20}$$

Thus, upon substitution of $\hat{X}^{\sigma}_{\mathrm{SDS}}$ with the auxiliary polynomial function and subsequent integration, the resulting expression for the fitting function reads:

$$
\begin{aligned}
\ln \hat{c} &= \left[\int \frac{\hat{X}_{\mathrm{SDS}} - \hat{X}^{\sigma}_{\mathrm{SDS}}}{\hat{X}_{\mathrm{SDS}} - \hat{X}^{2}_{\mathrm{SDS}}} d\hat{X}_{\mathrm{SDS}} \right]_{\hat{X}^{\sigma}_{\mathrm{SDS}} = 3^{rd} \text{ Order Polynomial}} \\
&= \ln\Big(1 - \hat{X}_{\mathrm{SDS}}\Big) \cdot (A + B + C + D - 1) + \\
&\quad + (A + B) \cdot \hat{X}_{\mathrm{SDS}} + \frac{A\hat{X}^{2}_{\mathrm{SDS}}}{2} - D \cdot \ln\Big(\hat{X}_{\mathrm{SDS}}\Big) + \text{Const.}
\end{aligned}
\tag{4.21}
$$

The respective phase diagrams for three different surface pressures are given in figure 4.40. The synergism in the SDS:AdTAB mixture is again expressed in a minimum in the $\ln \hat{c}(\hat{X}_{\mathrm{SDS}})$ curves. However, for the presented mixture, the derived surface composition does not amount to a single value but varies monotonously in a certain interval. The synergism between the surfactant species yields an azeotropic point at the shared global minimum of both, bulk and surface composition. Contrarily to the previously discussed systems, where the catanionc complex formation results in an extremely narrow distribution of $\hat{X}^{\sigma}$ around the azeotrope, the weaker attractive interactions in SDS:AdTAB mixtures lead to a considerable curve broadening. This effect appears to be strongest for higher concentrations, or surface pressures, respectively. As a result, surface compositions at low surface tension and high bulk SDS percentage differ more from the electroneutral composition, than the respective diluted solutions. This trend might be caused by the different length scales of attractive Van-der-Waals and Coulomb forces. At high degrees of dilution, the long-ranging electrostatic forces favour the formation of the electroneutral catanionic complex stoichiometry in the monolayer. However, at higher concentrations the short-ranged hydrophobic interactions, which are more significant between two linear n-dodecyl moieties than between an n-dodecyl and a compact adamantyl cage, come into play and induce the integration of a considerable dodecyl sulfate excess. Besides, charge screening effects at higher concentrations may also weaken the attraction between the oppositely charged headgroups. Therefore, the surface layer gets enriched with the more surface-active surfactant dodecylsulfate.

4.2.3.3. SFG-study of mixed SDS:AdTAB systems

For a more detailed look on the adsorption layers of mixed SDS:AdTAB solutions several SFG-spectroscopy measurements were performed. Figure 4.41 displays the spectra of three mixtures of SDS:AdTAB in *ssp, ppp* and *sps* polarisation combination for mixing ratios of 20:1, 1:1 and 1:20 and a shared surface tension of $40\,\mathrm{mN\,m^{-1}}$, according to the tensiometry results. First, the *ssp* spectra will be discussed. They suggest, as evidenced by the non-vanishing intensity on the right side of the spectra, that an electrical field must be present at the interface. Fitting of the spectra revealed an opposite sign of the parameter A_w for the water signal relative to the symmetric aliphatic stretching signals. For better comparability, the water contribution is fixed at a wavenumber of ω_w $= 3150\,\mathrm{cm^{-1}}$ with peak broadening Γ_w assumed to be $100\,\mathrm{cm^{-1}}$. At high bulk excess of AdTAB, water contributions could be reduced by a certain degree.

Additionally, the spectral region of water stretching modes is given in the bottom right panel of figure 4.41, which again shows that particular trend. The optical processes employed in the SFG-spectrometer required to generate the tunable IR-light energy also lead to a certain modulation of the output intensity. At $3125\,\mathrm{cm^{-1}}$ latter drops substantially, which caused an unsteady curve even after normalisation, especially for rather high SFG-responses. Therefore data above that wavenumber was not considered for the spectral fitting of the

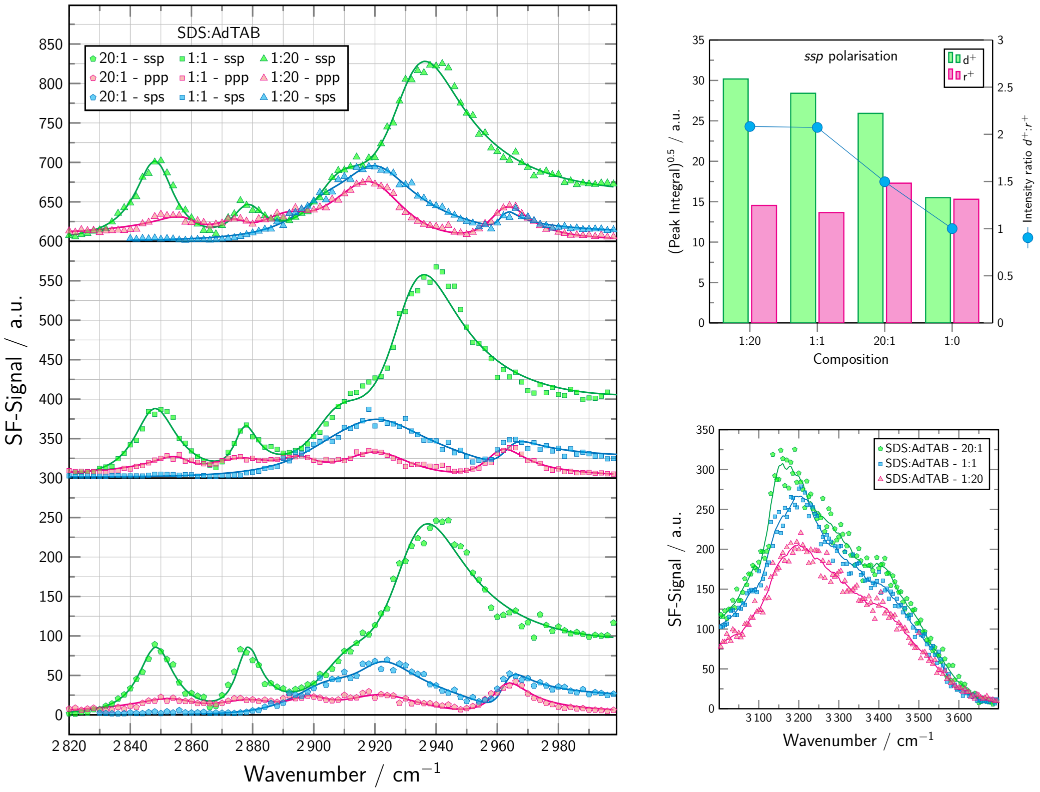

Figure 4.41.: Left: SFG-spectra (*ssp, ppp, sps*) of mixed SDS:AdTAB solutions. For clarity, *ppp* spectra are amplified by a factor of 2 and all three data sets of the same composition are offset by a fixed value. Solid lines correspond to best fit functions. Right top: Results of the deconvolution procedure for the d^+ and r^+ mode in *ssp* polarisation combination. Right bottom: SFG-spectra (*ssp*) in the spectral regime of OH vibrational modes. Savitzky-Golay smoothed lines given as guide to the eye.

CH-modes.

On the left side of the CH-spectrum, the symmetric stretching intensities show a slight variation in their apparent maxima, especially for the r^+ mode, which is declining with increasing AdTAB content. Despite the similar appearance in comparison to the pure SDS spectrum, the SDS:AdTAB mixture exhibits some characteristics in its SFG-spectra.

The first to name is the difference in the $d^+ : r^+$-ratio. For the presented mixed systems, this quantity is well leaning towards the d^+ mode, which is illustrated in the adjoining bar chart. This is in contrast to pure SDS at comparable surface pressure, where both vibrational modes contribute almost equally as much to the SFG-response. Note that absolute intensities of the three mixtures and the 1:0 sample may be affected by adjustment between the respective measurements. However, they can be compared by considering their relative intensities $d^+ : r^+$.[139] This quantity decreases from well above 2 for the 1:20 mixture to 1 for the pure SDS sample in water. Without going further into detail, this already verifies the significant interaction of AdTAB with dodecyl sulfate in the surfactant layer, but more on that later.

The second feature different from pure SDS is the shoulder at $2910\,\mathrm{cm}^{-1}$, adjacent to the intense Fermi resonance signal at the wider region around $2940\,\mathrm{cm}^{-1}$. It is most prominent for the 20:1 and 1:1 mixtures. In accordance to earlier assignments, it is probably due to a methine and/or a d^- contribution from the adamantyl framework.

Similar to the *ssp* spectrum, the *sps* polarisation combination also allows for significant interference effects between the water and CH vibrational modes, which shift and perturb the spectra to a certain degree. For a complete portrayal of the CH/OH region cf. figure 4.42, where the spectral regime from 2800 until $3700\,\mathrm{cm}^{-1}$ for a 1:1 mixture with normal and d_{25}-SDS is shown. The effect of SDS deuteration on the spectra will be discussed later on. In this polarisation combination, two main features can be observed for the SDS:AdTAB mixture. One broad feature around $2920\,\mathrm{cm}^{-1}$, which can be assigned mainly to the asymmetric methylene stretch and a smaller peak at $2965\,\mathrm{cm}^{-1}$ corresponding to the asymmetric methyl stretch of the terminal SDS group. Whereas the first feature grows with increasing AdTAB content, the second one shows a decreasing tendency, which is in agreement with the expulsion of the cage-

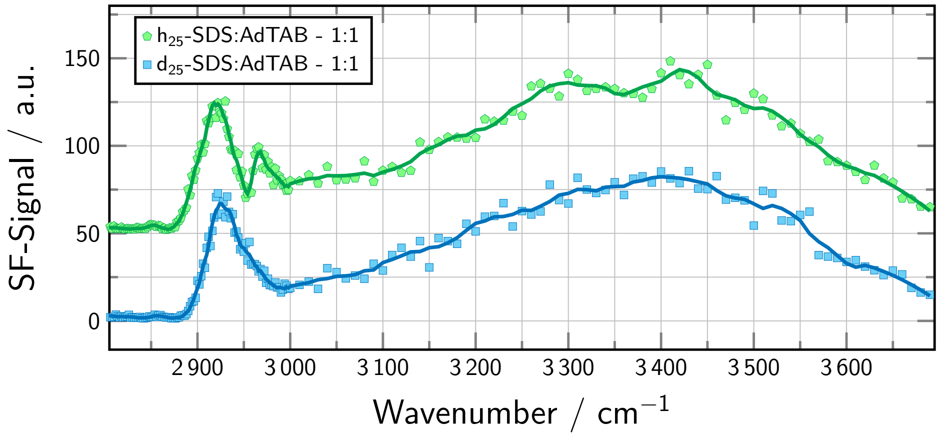

Figure 4.42.: *sps* spectra of 1:1 SDS:AdTAB mixtures. Spectra are offset for clarity. Savitzky-Golay smoothed line given as guide to the eye.

amphiphile and its exchange for dodecyl sulfate.

The *ppp* spectra of the three mixtures slightly differ from each other, indicating a subtle change in the monolayer composition. Generally, they all contain signals from d^+, r^+, d^-, CH and r^- modes as weak peaks at 2855, 2878, 2895, 2918 and 2963 cm^{-1}. Most prominently and in accordance with the previous observations, the maximum at 2918 cm^{-1} gradually outgrows the asymmetric methyl signal with increasing AdTAB content, until the profile resembles the *ppp* polarised DTAB:SAdMeS spectrum.

In a second experimental series, SDS was exchanged with its perdeuterated analogon, as shown in the left panel of figure 4.43. Note, that the absolute values of this series are not compared to the previously described results since the setup was adjusted between the measurements. For the different compositions, a certain trend can be observed. The *ssp* peak maxima of the signals at 2850 cm^{-1} and 2930 cm^{-1} decline for high d_{25}-SDS content in the mixture. This is due to the increasing proportion of the now masked anionic surfactant in the monolayer. Once again, the characteristic peak-shoulder around 2910 cm^{-1} can be observed, especially for the 1:1 and 1:20 composition of SDS:AdTAB. In accordance, the *ppp* spectra also decrease in signal intensity, when increasing the relative amount of SDS in the mixture. As expected, they do not contain signal at 2880 and 2965 cm^{-1}, which verifies the absence of contributions from SDS, as well as other organic impurities with methyl groups. As for the mixtures with conventional SDS, the signal at 2918 cm^{-1} is most pronounced, when the bulk composition is very AdTAB-rich.

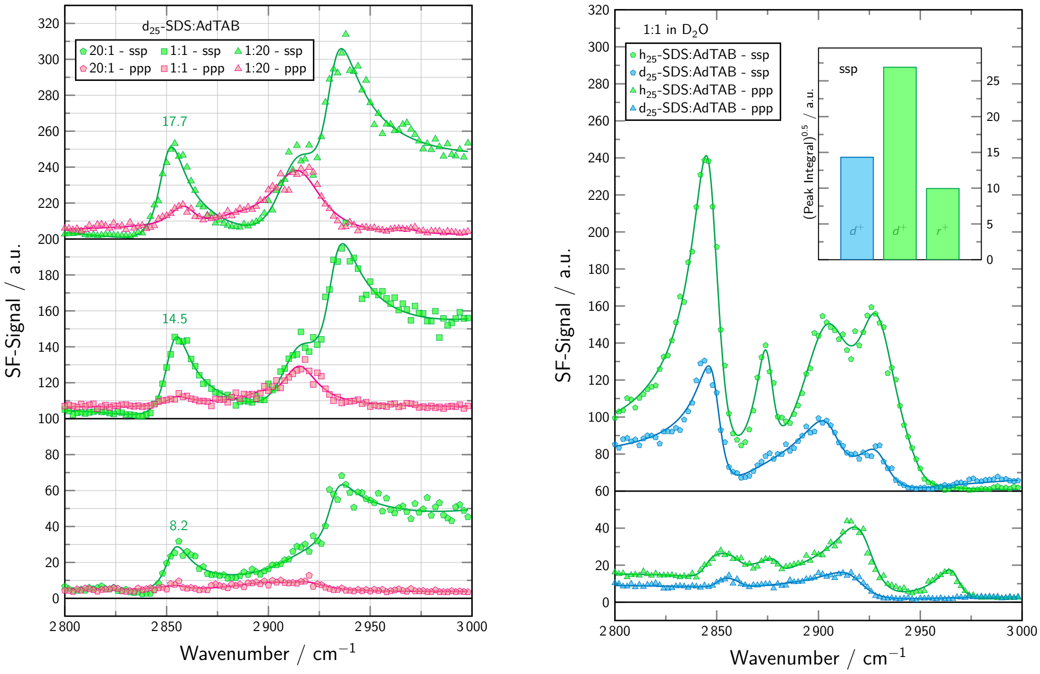

Figure 4.43.: Left: SFG-spectra (*ssp, ppp*) of mixed d_{25}-SDS:AdTAB solutions. For clarity, *ppp* spectra are amplified by a factor of 2 and both data sets of the same composition are offset by a fixed value. d^{+} integral (from *ssp*) annotated above the peak. Right: SFG-spectra (*ssp,ppp*) of equimolar composed SDS:AdTAB solutions in D_2O. Solid lines correspond to best fit functions. Peak area square roots of the methyl and methylene symmetric stretching modes in the *ssp* spectra are given as bar chart in the corresponding colour scheme.

By exchanging H_2O with D_2O, the distortion of the aliphatic region of the SFG-spectrum by contributions from interfacial water could be minimised. Exemplarily, the *ssp*-spectra of a 1:1 SDS:AdTAB mixture is shown in the right panel of figure 4.43 for perdeuterated and conventional SDS. Additionally, the result of the spectra deconvolution for the symmetric stretching modes is given as bar chart inset. For the fitting procedure, remaining SFG-contributions from water, caused by the surface electrical field were summarised as non-resonant background. At first glance, the curves adopt quite the same shape, as was observed for the SDS:Bola mixtures in D_2O discussed earlier. Accordingly, the protonated mixture exhibits a significantly more intense d^+ mode, as compared to the r^+ signal. Spectra deconvolution yielded a similar intensity distribution as for the samples in conventional water. The variations in absolute intensity are due to the set-up adjustment, uncertainty in the fitting procedure of background signals and unresolved overlapping peaks. By masking the SDS contribution, AdTAB was found to contribute around one half of the combined d^+ peak area square root. Consequently, the other half must then originate from the dodecyl sulfate tails. Considering the r^+ contribution is around the same height as the d^+ difference, it can be argued that the order in the SDS hydrophobic backbone, as determined by SFG-spectroscopy, is not significantly influenced by the integration of AdTAB into the monolayer.

In the spectra of the SDS:bola:D_2O mixtures, one also finds a broad feature in the region between 2900 and 2950 cm^{-1}. However, an as clearly resolved feature around 2905 cm^{-1} as in the SDS:AdTAB mixtures is not found in these systems. Thus, it can be concluded that the broad feature also contains a characteristic footprint of the adamantane rest. As discussed above, the specific orientation of the methylene groups and the presence of methine groups may be responsible for that.

The *ppp* spectra of 1:1 mixtures with masked and unmasked SDS in D_2O are not very different from those in conventional water, except from a background contribution from deuterated water. Again, a significant shoulder is found at 2918 cm^{-1} in both spectra, which, to such extent, has not been found in systems without the adamantyl unit. The intensity relationship between the two spectra is in agreement with previous observations, whereby universally higher values of the SFG-intensity are found with the perprotonated mixture. This implies, that the broad signal between 2900 and 2950 cm^{-1} in this mixture is not only due to methine vibrations, but also incorporates other contributions from the dodecyl tail, e.g. Fermi resonances or the asymmetric methylene vibration.

Contrarily, the same spectral region in the *sps* spectrum appears to be dominated by contributions from adamantyl, since the lower wavenumber peak of the doublet below 3000 cm^{-1} mostly maintains its height upon deuteration of the dodecyl sulfate component, whereas the right feature with a maximum at 2967 cm^{-1} completely disappears. This is presumably because the *sps* polarisation combination primarily probes the asymmetric vibrations of methyl and methylene groups.[83] As discussed above, the adamantyl geometry is resulting in intense d^- contributions, compared to the linear surfactant species. Consequently, masking of SDS only removes the r^- contribution from the spectrum.

In conclusion, SFG-spectroscopy of the mixed SDS:AdTAB systems could show, that in agreement with the surface tension data, the surface composition of the mixed monolayer is not as constant as for the other discussed systems, which might be due to the significant mismatch in surface-activity of SDS and AdTAB. By selective deuteration of SDS, contributions from AdTAB could be revealed. A pronounced feature roughly around 2915 cm^{-1} in any polarisation scheme was found and ascribed to d^- and/or methine vibrations which are characteristic for the adamantyl moiety. Other than for the DTAB:SAdMeS mixture, the integration of AdTAB into the SDS monolayer appeared to have no positive influence on the degree of order in the dodecyl tails. Therefore, one could speculate, that the hydrophobic part of the cationic amphiphile is not as deeply buried in the monolayer with C_{12}-surfactant, as it is with the anionic adamantyl species. This is probably because of the missing spacer unit between headgroup and adamantayl cage in the AdTAB molecule and also its more hydrophilic character, which keeps AdTAB closer to the solution phase.

4.2.3.4. Foaming Behaviour of mixed SDS:AdTAB Systems

Like for the DTAB:SAdMeS mixture, the SDS:AdTAB systems were also investigated with respect to their foaming behaviour. Therefore, the foam decay of a series of compositions between 20:1 to 1:20 and concentrations between 1.5 × *cmc* and $c(\gamma_\infty = 60\,\mathrm{mN\,m^{-1}})$, according to the tensiometry results, was monitored.

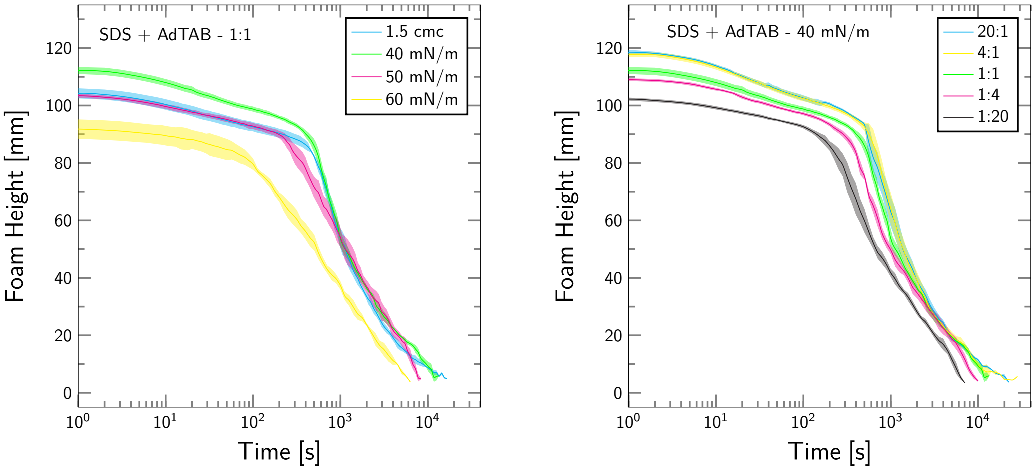

Figure 4.44.: Foam decay of selected samples of the SDS:AdTAB mixtures as function of the time after reaching the maximum height. Every sample was measured at least three times. Error given as shaded region.

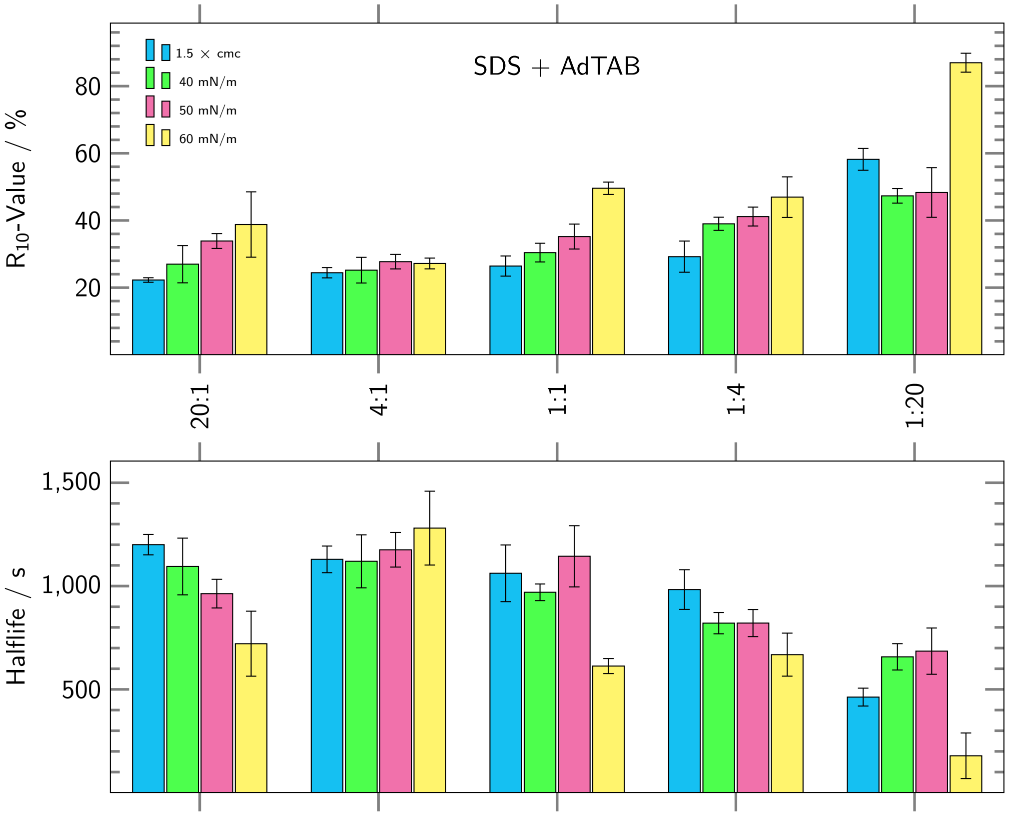

Figure 4.45.: Foam stability parameters of mixed SDS:AdTAB solutions. Top: Foam column half-life time. Bottom: R_{10}-Value = Collapsed foam height (in %) ten minutes after reaching the maximum value.

Contrarily to the DTAB:SAdMeS mixtures, the SDS:AdTAB mixtures exhibited a good reproducibility in their foam decay curves, as shown in figure 4.44. Exemplarily, two sets of mixtures and concentrations are depicted (1:1 and $40\,\mathrm{mN\,m^{-1}}$). For these systems, the errors between the individual measurements of the same sample were very small, and the decay of the foam column happened very steadily until full collapse was achieved. All investigated systems exhibited good stability of the column. However, noticeable trends were detectable. Rather straight forward, faster decay and slightly worse foamability are found for reduced concentrations at fixed composition (i.e. 1:1). In comparison to the DTAB:SAdMeS mixtures, where the $60\,\mathrm{mN\,m^{-1}}$ sample almost immediately collapsed, this system still is remarkably stable.

Keeping the surface tension fixed and varying the composition showed a reduced foamability and life-time of the foam column for increasing excess of AdTAB in the mixture. The stability parameters halflife-time and R_{10} for the whole experimental series are summarised in figure 4.45. Despite some scattering in the data the highest R_{10} value and the lowest half-life were found for the 1:20 mixture in every surface tension batch.

In the literature, foam stability is often correlated with the dilatational elasticity of the surfactant monolayer.[192–196] This property is accessible by sinusoidal perturbation of an interface and measurement of the system response, i.e. the surface tension. The complex surface dilatational modulus E is given by:[165]

$$E = \frac{d\gamma}{d \ln A} = |E| \cdot e^{i\phi} \tag{4.22}$$

Here, ϕ represents the phase shift between the perturbation and the response function. The composition dependent modulus of different SDS:AdTAB mixtures at a surface tension of $40\,\mathrm{mN\,m^{-1}}$ is given in figure 4.46.

For the applied frequency, the monolayer still behaves as soluble, and thus the dilatational behaviour is mostly governed by the diffusion of surfactant. Therefore, the observed trough-like shape of the E vs. X_{SDS} data is in accordance with the results of the SDS:DDPB dynamic surface tension analysis (cf. section 4.1.4). For bulk compositions, which are close to the equilibrium surface composition, perturbations are quickly compensated by diffusional mass transport. Consequently, the modulus shows rather small values. In contrast, for the very asymmetric composed mixtures, the concentration of the minor component is fairly low, which means that establishment of the equilibrium composition

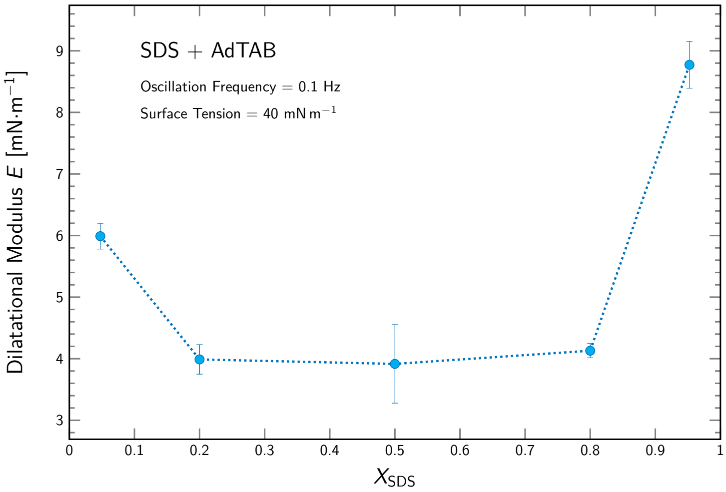

Figure 4.46.: Surface dilatational modulus of mixed SDS:AdTAB solutions. Perturbation frequency was 0.1 Hz and concentrations were chosen to yield 40 mN m^{-1} surface tension.

is comparably slower. This implies, that the surface tension response towards surface expansion or compression, respectively, i.e. the dilatational modulus, is considerably elevated. The very SDS-rich solution shows a higher modulus than the AdTAB-rich solution. This might be due to the differences in total surfactant concentration (cf. figure 4.29). Since $\hat{c}$ is around twice as much for the AdTAB-rich solution, and therefore also the concentration of the minor component, a better compensation of surface disturbances for the 1:20-mixture is reasonable.

Although the composition dependence of the modulus can be rationalised by the diffusional transport, it does not necessarily match the reduced foam stability of the 20:1 composition. However, SFG-spectroscopy could show a reduction of the electric field penetration depth via the water stretching modes. Accordingly, the reduction in the foam stability might, at least to a certain degree, be due to the diminished electrostatic repulsion of the opposing adsorption layers, which eases coalescence of bubbles and, as a result, the collapse of the foam column.

4.2.4. Combined Cage-Amphiphiles

In analogy to the previously shown results, the two adamantyl amphiphiles were combined and examined via tensiometry and SFG-spectroscopy in order to investigate how a catanionic monolayer with two bulky residues behaves. Figure 4.47 displays the surface tension isotherm of a 1:1-mixture of SAdMeS and AdTAB as well as an equimolar mixture of the corresponding C_{12}-surfactants SDS:DTAB. Tables 4.6 and 4.7 contain the best-fit parameters of the Frumkin model and the surfactant characteristic parameters A_{min} and pC_{20}. Similar to a solution of pure SAdMeS, no kink in the graph indicates the onset of micellisation for the SAdMeS:AdTAB system. Instead, white crystals precipitated, when combining AdTAB and SAdMeS solutions with a resulting surfactant-only ionic product $(c_{\text{SAdMeS}} \cdot c_{\text{AdTAB}})^{\frac{1}{2}} > 20\,\text{mmol}\,\text{L}^{-1}$. Therefore, the surface tension could not be reduced significantly beyond $50\,\text{mN}\,\text{m}^{-1}$, in agreement with pure SAdMeS-solutions.

Table 4.6.: Fitting parameters according to the Frumkin model for the curves shown in figure 4.47.

Surfactant	ω [10^5 m^2 mol^{-1}]	b [m^3 mol^{-1}]	a
SAdMeS:AdTAB	5.8	0.32	1.4
SDS:DTAB	3.9	372	1.35

Table 4.7.: Surfactant characteristic parameters corresponding to the curves shown in figure 4.47 with the ionic product taken as measure for the concentration.

Surfactant	pC_{20}	A_{min} [nm^2]
SAdMeS:AdTAB	2.02	107
SDS:DTAB	5.82	63

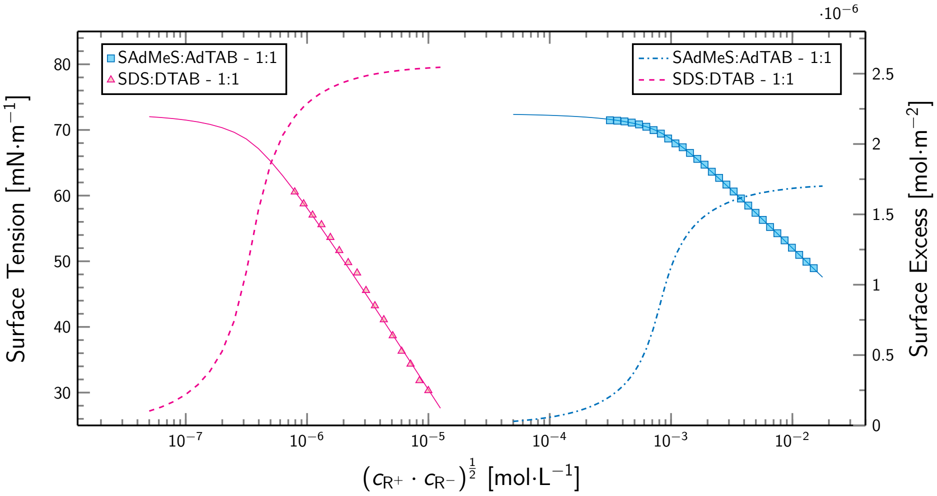

Figure 4.47.: Left axis: Surface tension as function of the surfactant-only ionic product of 1:1 catanionic mixtures. The according Frumkin-type fit is given as solid line. Best fit parameters are listed below. Right axis: The derived surface excess concentration is given as broken line.

This is in contrast to the catanionic mixtures where linear surfactant species are involved. These systems usually show a significant difference in the obtained maximum surface pressure (i.e. surface pressure at the cmc), with respect to the individual components. Examples also have been shown in the previous sections. For long-chain surfactant mixtures, stoichiometric complexes are formed by mutual cancellation of headgroup charge. This enables close packing and aligns the alkyl backbones towards an all-trans configuration driven by significant inter-chain attraction, which results in a rather low surface tension. Contrarily, the rigid adamantane framework has no degrees of freedom. Upon merging SAdMeS and AdTAB solutions, the surface affinity of the mixed surfactant is elevated by catanionic complex formation. However, the adamantyl moieties do not interact as severe due to their rather bulky architecture, which leads to a not as dense surface packing. This manifests as a considerable difference in the slopes of the $\gamma(\log(c^*))$ plots, and consequently the excess concentration, as shown in figure 4.47 as well as the minimum surfactant area (cf. table 4.7).

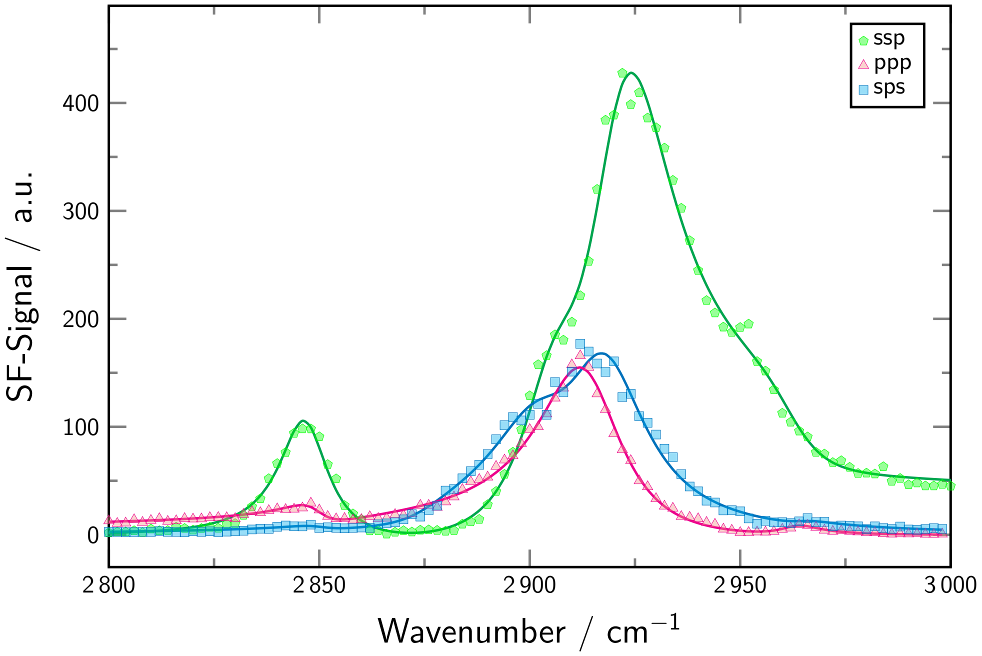

Figure 4.48.: SFG-Spectra (*ssp, ppp, sps*) of a 1:1 mixture of SAdMeS and AdTAB in the overlapping spectral regime of CH and OH vibrational modes.

The good surface-activity (in comparison to the parent compounds), the absence of terminal methyl groups in the hydrophobic rest and the rigid alkyl cage structure also make the surfactant combination interesting as a model compound for SFG-spectroscopy. Figure 4.48 shows SFG-spectra of a 1:1-mixture of SAdMeS and AdTAB (each 15 mmol L^{-1}). The *ssp* spectrum displays only two main features. First the d^+ peak at 2845 cm^{-1}, and second a broad and intense signal from 2880 to 2970 cm^{-1} with maximum intensity at 2925 cm^{-1}. It contains also a rather poorly resolved shoulder on each side and transitions into a non-vanishing SFG-intensity at $\geq$ 3000 cm^{-1}. A fitting routine reveals an opposite phase between the water background and the CH-contributions, and thus a negative surface excess charge. This is in agreement with the higher surface affinity of SAdMeS compared to AdTAB, allowing the anionic species to adsorb at a slightly higher amount. No noteworthy contribution from an r^+ vibrational mode is observed, although AdTAB, does bear three methyl groups per molecule in its headgroup. The proximity to the nitrogen might induce a spectral shift of the headgroup r^+ mode to a different wavenumber. Such a shift has been reported in the literature for the trimethylammonium function in the choline headgroup of membrane lipids,[197,198] and more recently for the headgroup methyl units of the C_{16} species of a quaternary ammonium surfactant.[199] In accordance to that, the subtle signal around 2965 cm^{-1} in *ppp* polarisation, might rather be due to the r^+ mode of the headgroup than an r^--mode. This would also explain the absence of a corresponding peak in the *sps* spectrum, since, according to the polarisation selection rules,[83,131] symmetric stretching vibration does not contribute to the SFG-signal in that polarisation combination.

The most prominent feature in the *ppp* spectrum, however, is the broad and intense signal with maximum at 2911 cm^{-1}. A peak in SFG-intensity has been observed at similar positions in the DTAB:SAdMeS and SDS:AdTAB spectra, although far less pronounced. Thus, its assignment to a vibrational component from the adamantyl cage, rather than from contributions in the linear alkyl tail is justified retrospectively. In accordance to the previous assignments, the feature can be ascribed to the overlapping signals from methine stretching and d^- vibrations. At the interface, the rigid aliphatic framework creates a high degree of anisotropy concerning the spatial orientation of the involved CH and CH_2 groups. In combination with the high number density in the double-cage catanionic adsorption layer, this especially elevates the signal in polarisation combinations which probe the asymmetric stretching vibrations (*sps, ppp*) to impressive heights. The resulting spectrum is characteristic for the adamantane cage and differs distinctively from conventional linear surfactant spectra as shown in the previous sections. Usually, spectra of conventional surfactant in these polarisation combinations are dominated by contributions from the methyl group, and the methylene groups, even though present in non-centrosymmetric conformations, are only of minor importance (also cf. spectra in refs. [87, 149, 200, 201]). However, since they may be located at different positions in the alkyl tail, the orientation of the methylene units in the gauche-defect is ill-defined and does only yield a small signal. In contrast, the group orientation is fixed in the adamantyl frame, and the alignment of the molecules in the surface layer by the anchoring headgroup produces a significant SFG-signal as a result of that.

5. Summary

In the presented work, several aqueous surfactant systems were investigated with special focus on the self-assembled monolayers at the air/water interface. The first part of this thesis is devoted to bolaamphiphiles, which exhibit two hydrophilic groups, separated by a linear alkyl backbone. A symmetric divalent (DDPB) and an asymmetric univalent (UHPB) model bolaamphiphile were synthesized and compared to the conventional long-chain cationic surfactant nDPB. It could be shown by tensiometry measurements, that the exchange of the terminal methyl unit of nDBP by a second hydrophilic moiety severely reduces the surface-activity of the amphiphile.

Via sum-frequency generation spectroscopy the vibrational signatures of adsorption layers of nDPB, UHPB, and DDPB were measured. A dilution series of nDPB spanning over four orders of magnitude could show that the surface concentration of surfactant levels off above the cmc via the intensities of d^+ and r^+ vibrational modes. The respective water signal experiences a modulation of its intensity, which is due to the interplay of increasing surface charge and decreasing screening-length. SFG-spectra of DDPB and UHPB suggested a near-saturated monolayer above $25\,\mathrm{mmol\,L^{-1}}$ and exhibited a depression of the water signal, which agrees with the surfactant/counterion stoichiometry.

The presented results show that catanionic mixtures of SDS and a divalent symmetrical or a monovalent unsymmetrical bolaamphiphile, respectively, behave similarly to their conventional double linear tailed counterparts when it comes to the establishment of the surface pressure. A nearly constant surface composition close to the electroneutral point over a broad range of bulk compositions was indicated by a derivation of Aratono's approach. Displaying the surface tension isotherm of the systems SDS:nDPB, SDS:UHPB and SDS;DDPB as a function of the surfactant-only ionic product c^{*}, lead to a collapse of all surface tension isotherms onto a single curve for each respective mixture. This further supported the finding of near-constant surface composition. In terms of surface-activity, an increase could be found from nDPB:SDS over DDPB:SDS to UHPB:SDS. The amount of adsorbed catanionic complex determined via the Frumkin adsorption isotherm was found to agree well with the number and size of involved hydrophilic groups.

The dynamic surface tension of the SDS:DDPB mixture displayed a strong dependency on the bulk composition. The further away the mixture was from the 2:1 ratio, the longer it took to establish a certain equilibrium surface tension. Evaluation of the kinetics with the long-time linearisation method of the Ward-Tordai equation showed a good correlation with the concentration of the catanionic complex, which implies that the adsorption process near equilibrium is mostly dominated by the combined species in a 2:1 ratio, even if the respective bulk composition is vastly different.

SFG-spectroscopy could shed some light onto the interfacial architecture of the investigated pyridinium surfactant mixtures, which are due to the special structure of the bolaamphiphiles and affect the interaction with the oppositely charged co-surfactant SDS. Despite a surfactant ratio near the electroneutral point in the monolayer, SFG-spectroscopy indicates some negative excess charge even for the 1:20 SDS:bola mixtures by the presence of significant third-order contributions from aligned water. However, the actual dodecylsulfate excess is not necessarily as pronounced due to the low ionic strength and large Debye screening length in the catanionic solutions.

By selective deuteration, individual contributions to the SFG-spectrum of the mixed solutions could be distinguished. The results obtained by spectral deconvolution helped to propose a model structure of bola and co-surfactant, which concerns the degree of bending within the respective alkyl backbone and the number of Gauche-defects in the hydrophobic rest. A signal ratio of roughly 3:1 for the d^+ vibrational mode of bola and SDS can be nicely rationalised with a heavily curved bola backbone ($\simeq$180°) and moderately kinked dodecylsulfate tail. The ratio of methyl and methylene contributions from SDS was found different for the two mixtures. This could either mean that SDS:UHPB monolayers produce fewer Gauche-defects in total, or that the mean orientation of the terminal methyl group of SDS (and its distribution) is different for the two mixtures. Unlike in the double-tailed SDS:nDPB cationic complex, both mixtures of SDS and bolaamphiphile do not exhibit a pronounced enhancement of the SDS *n*-alkyl tail ordering, as evidenced by the ratio between the corresponding methyl and methylene SFG-contributions.

In the second part of this thesis, amphiphilic molecules were investigated, which bear the 1-adamantyl diamondoid moiety as the main hydrophobic unit. Therefore the cationic species AdTAB and the anionic SAdMeS were synthesised. SAdMeS exhibited a weaker surface activity and as a consequence also weaker foam stability, compared to the linear C_{11}-alkylsulfate counterpart SUndS. Combination with the oppositely charged surfactant DTAB, however, yielded remarkably synergistic mixtures. Evaluation with Aratono's method and re-plotting as γ vs. c^* both suggested an equimolar monolayer composition in the bulk composition range between 16:1 and 1:16.

Foam stability measurements were weakly reproducible, which might be indicative for the absence of an electrostatic stabilisation of foam lamellae, and thus agrees with the 1:1 surface composition. Enlarged aggregates, which boost the foamability and stability of the DTAB:SAdMeS mixtures above the cmc, were verified via DLS.

The electroneutral composition was further verified via SFG-spectroscopy, which showed only minor contributions of water to the SFG-intensity and a stable CH peak intensity distribution for the compositions 16:1, 1:1 and 1:16. In comparison to the spectrum of pure DTAB, the mixed system exhibited a reduced d^+/r^+ ratio which is indicative for an ordering effect of SAdMeS on the DTAB tails. Intense contributions in *sps* and *ppp* spectra around $2900\,\mathrm{cm}^{-1}$ were ascribed to d^- and methine stretching vibrations from the adamantyl framework. A comparably small intensity of the d^+ vibration was rationalised via symmetry-considerations.

AdTAB alone was found to be an even weaker surfactant than SAdMeS is. This manifests also in the extent of the synergism with SDS, which is weaker than for the previously discussed systems. Surface tension analysis indicated a certain dynamic in the surface composition of mixed SDS:AdTAB adsorption layers in the bulk compositional range between 20:1 and 1:20. The pronounced mismatch in hydrophilicity was proposed as the reason for that, which means that SDS alone could compete with the catanionic complex in terms of surface activity to some degree, and AdTAB is located somewhere between a co-surfactant and an indifferent electrolyte.

SFG-spectroscopy in the region from 2800 to $3600\,\mathrm{cm}^{-1}$ could verify this finding via a significant signal from OH-vibrations in the mixed SDS:AdTAB spectra. Variation of the composition of the mixtures also manifested in the SFG-spectra, which again confirmed a considerable deviation from the electroneutral stoichiometry. Via selective deuteration, contributions from SDS and AdTAB could be separated, and again a characteristic peak pattern for the adamantyl framework could be found.

The foaming behaviour of mixed SDS:AdTAB solutions was investigated and the results showed good reproducibility. Reduced foam stability was measured for the very AdTAB rich samples. However, this trend was not mirrored in surface dilatational modulus, which showed a minimum around the 1:1 composition. It could be argued that the reduced foam stability in AdTAB-rich samples is mostly due to the weaker electrostatic repulsion.

Both cage-like surfactants were combined in solution and compared to a conventional catanionic mixture. The results showed a moderate surface activity and an elevated area demand for the double-cage system, which was explained via the weaker hydrophobic interactions of the adamantyl units, as compared to two linear C_{12} moieties. In the SFG-spectrum SAdMeS:AdTAB showed the features already seen in the other two mixed systems, although, more pronounced.

6. Publications

Excerpts of this thesis will be used for publication in the following article:

- A. Dietz, H. Motschmann. Composition and Molecular Structure in Mixed Monolayers of Sodium Dodecylsulfate and Cationic Bolaamphiphile. *Reproduced in part with permission from J. Phys. Chem. C, submitted for publication. Unpublished work copyright 2020 American Chemical Society.*

Results not shown in this work will be published in the following article:

- P. Karageorgiev, U. Paap, D. Feucht, A. Dietz, K. Rustler, B. König , and H. Motschmann. Forcing a pendant drop in a resonant vibrational mode by a cyclic photochemical reaction. *in preparation.*

Previously published work:

- A. A. Dietz, M. J. Hofmann, H. Motschmann, *The Journal of Physical Chemistry B* **2016**, *120*, 29, 7143–7147.

A. Appendix

A.1. NMR-Spectra

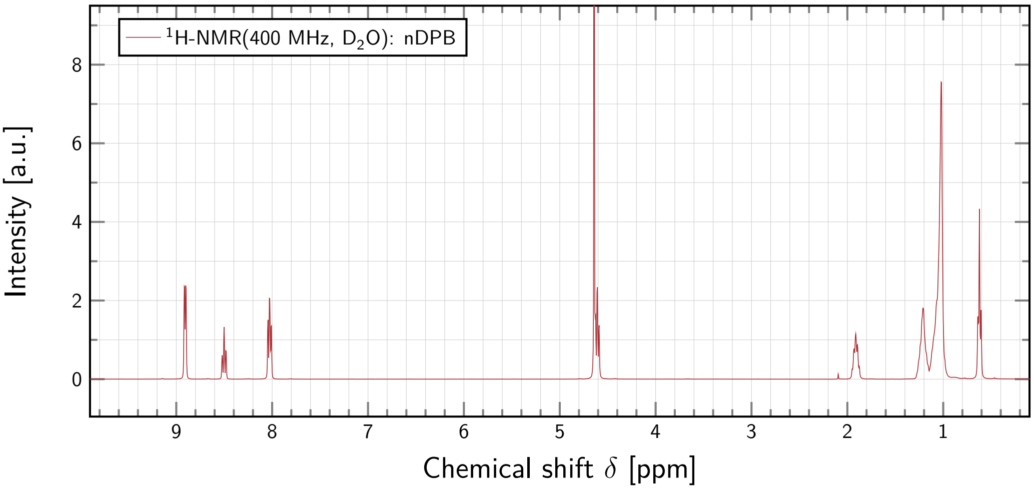

Figure A.1.: NMR spectrum of nDPB in D_2O: ^{1}H-NMR(400 MHz).

For easier portrayal of the data, shown spectra were compressed to a total of approximately 3000 data points by displaying only $\frac{1}{n}$ data points of the original spectrum. The abscissa displays the mean value of the evenly spaced n data points within the reducing interval. In order to maintain the original peak pattern the ordinate is chosen to display the maximum value within the reducing interval. Thus, no possible peak maximum is lost by the data reduction procedure. Peak picking and integration, as listed in the above sections, was conducted on the original spectra via the software Mnova NMR (Mestrelab Reseach S.L., Santiago de Compostela, Spain).

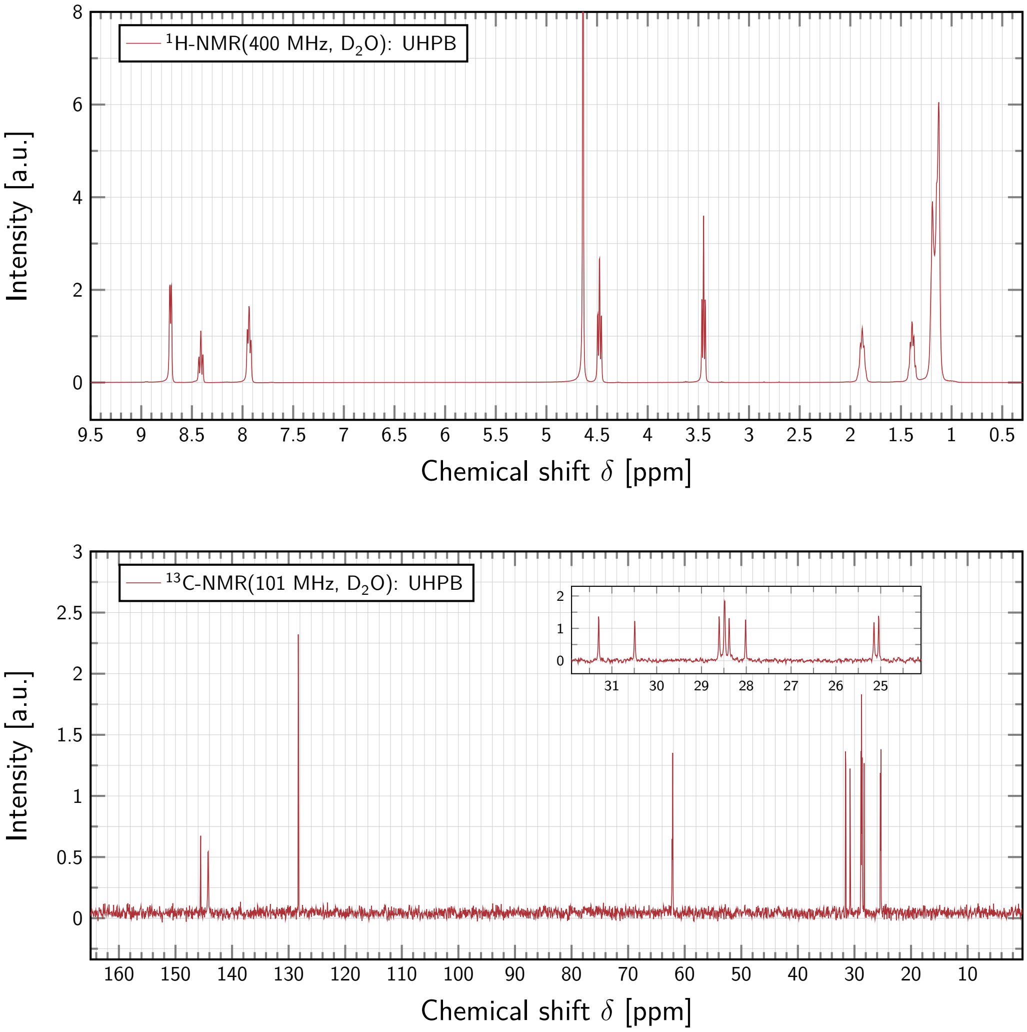

Figure A.2.: NMR spectra of UHPB in D_2O. Top: ^{1}H-NMR(400 MHz). Bottom: ^{13}C-NMR(101 MHz).

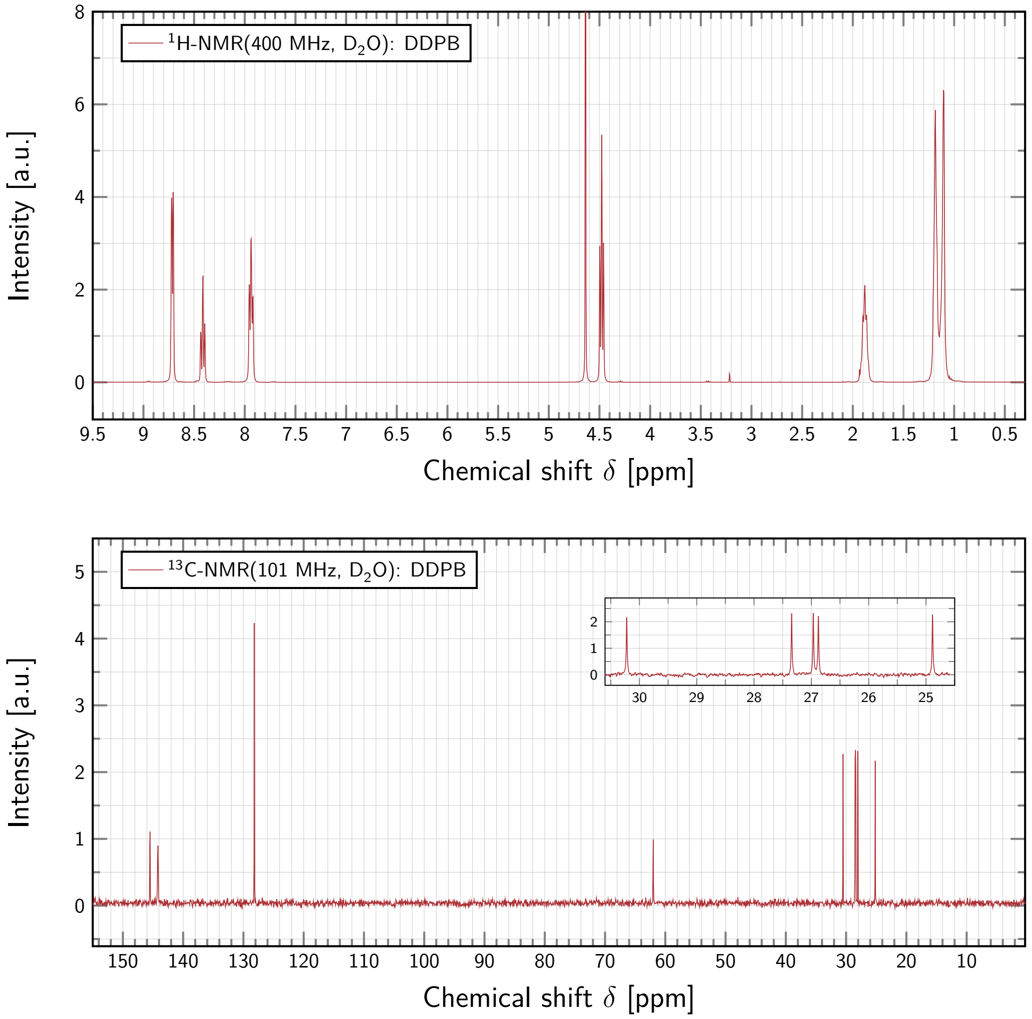

Figure A.3.: NMR spectra of DDPB in D_2O. Top: ^{1}H-NMR(400 MHz). Bottom: ^{13}C-NMR(101 MHz).

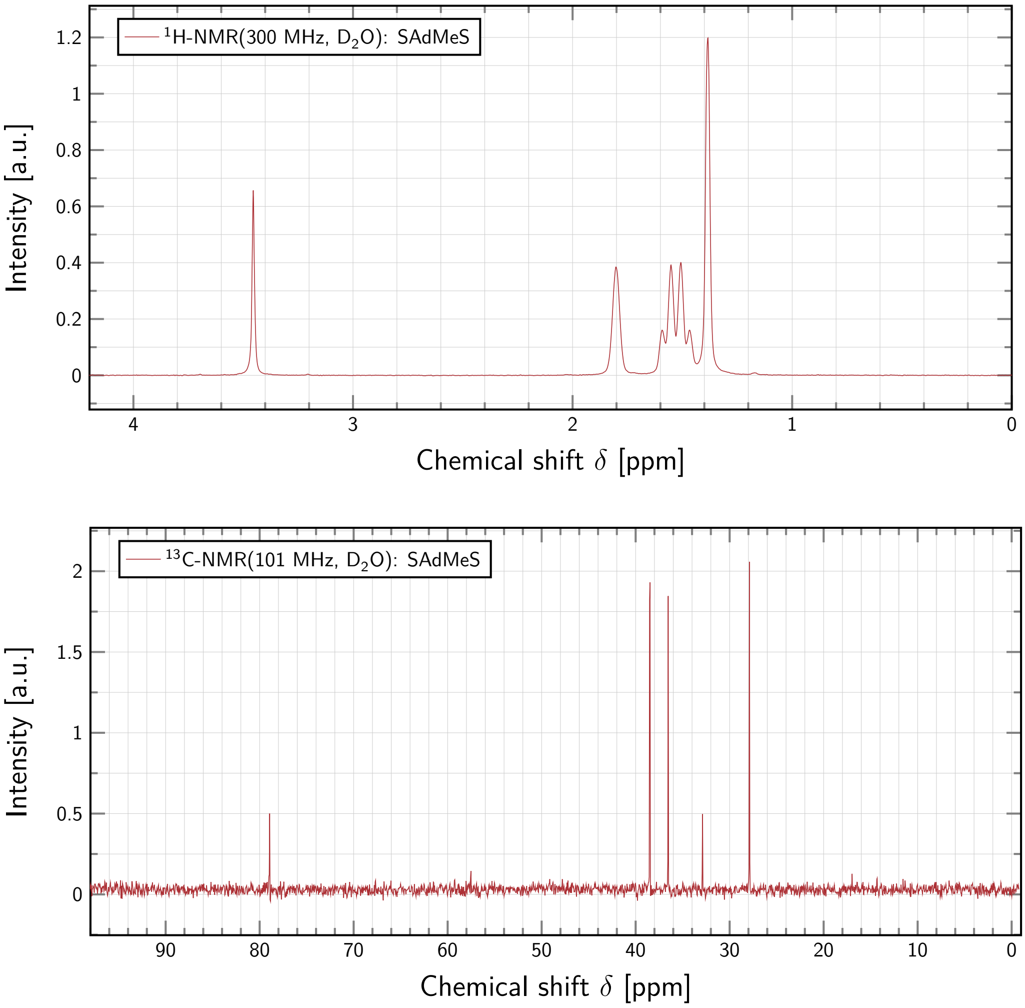

Figure A.4.: NMR spectra of SAdMeS in D_2O. Top: ^{1}H-NMR(300 MHz). Bottom: ^{13}C-NMR(101 MHz).

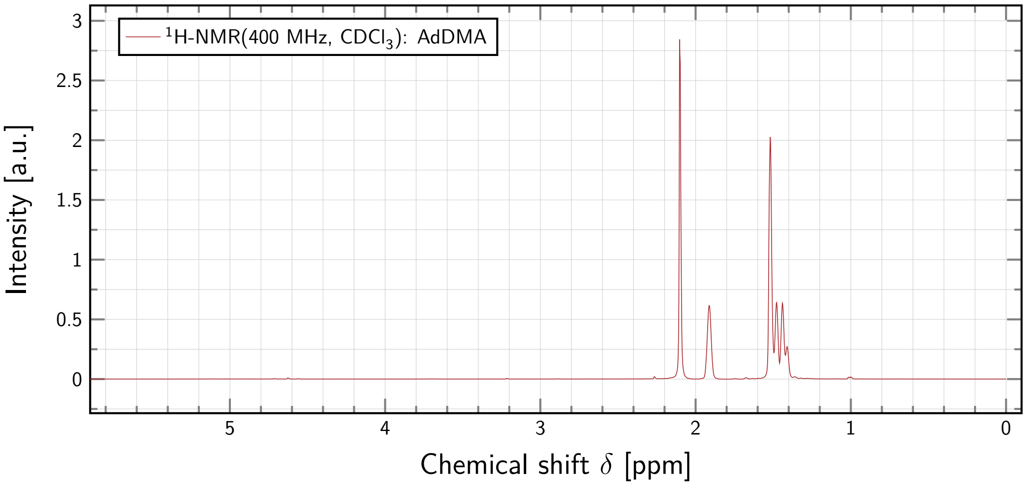

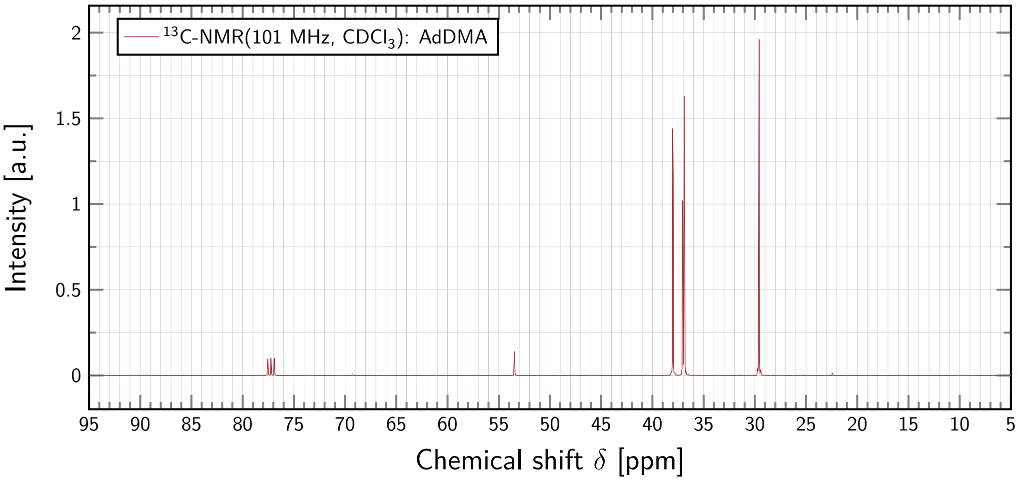

Figure A.5.: NMR spectra of AdDMA in CDCl$_3$. Top: ^{1}H-NMR(400 MHz). Bottom: ^{13}C-NMR(101 MHz).

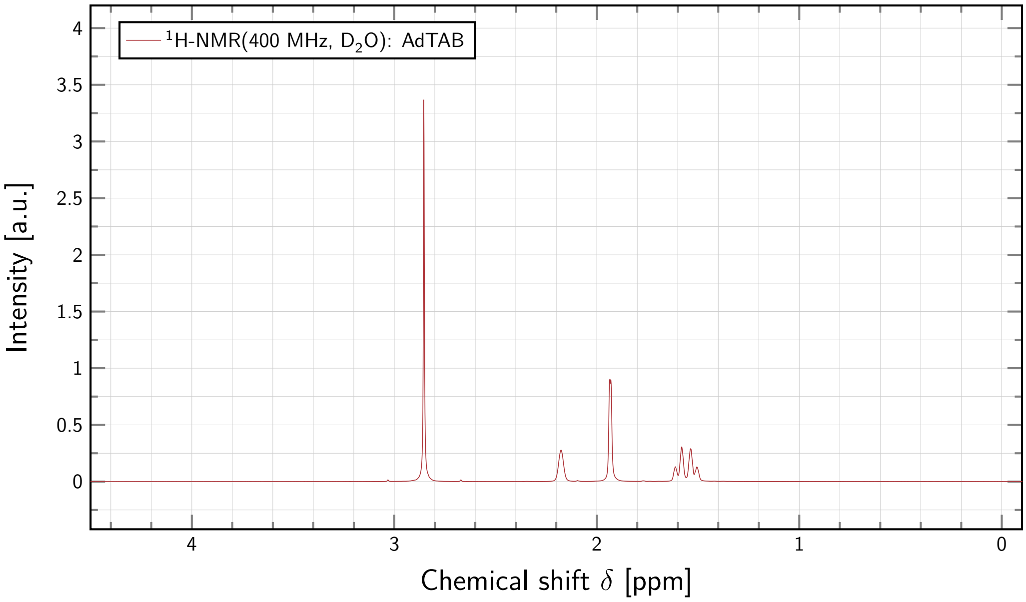

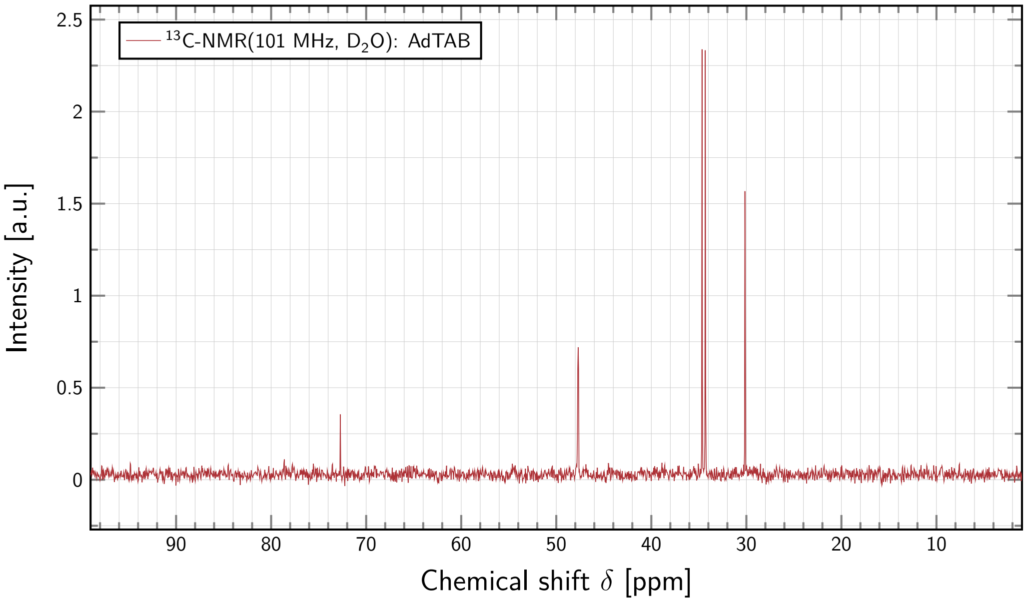

Figure A.6.: NMR spectra of AdTAB in D_2O. Top: ^{1}H-NMR(400 MHz). Bottom: ^{13}C-NMR(101 MHz).

Bibliography

[1] C. M. Thompson, L. M. Carl, G. A. Somorjai, *The Journal of Physical Chemistry C* **2013**, *117*, 26077–26083.

[2] Z. Chen, D. H. Gracias, G. A. Somorjai, *Applied Physics B: Lasers and Optics* **1999**, *68*, 549–557.

[3] L. Fu, Z. Wang, V. S. Batista, E. C. Y. Yan, *Journal of diabetes research* **2016**, *2016*, 7293063.

[4] C. Humbert, B. Busson in *Biointerface Characterization by Advanced IR Spectroscopy*, Elsevier, **2011**, pp. 279–321.

[5] T. Miyamae, H. Kato, M. Kato, *Chemistry Letters* **2018**, *47*, 1139–1142.

[6] K. Engelhardt, A. Rumpel, J. Walter, J. Dombrowski, U. Kulozik, B. Braunschweig, W. Peukert, *Langmuir* **2012**, *28*, 7780–7787.

[7] J. W. Gibbs, *Thermodynamics*, Ox Bow Press, Woodbridge, Conn., **1993**.

[8] I. Langmuir, *Journal of the American Chemical Society* **1917**, *39*, 1848–1906.

[9] K. B. Blodgett, *Journal of the American Chemical Society* **1935**, *57*, 1007–1022.

[10] P. Warszyński, K. D. Wantke, H. Fruhner, *Colloids and Surfaces A: Physicochemical and Engineering Aspects* **2001**, *189*, 29–53.

[11] V. B. Fainerman, R. Miller, R. Wüstneck, A. V. Makievski, *The Journal of Physical Chemistry* **1996**, *100*, 7669–7675.

[12] T. Gilányi, R. Mészáros, I. Varga, *Langmuir: The ACS Journal of Surfaces and Colloids* **2000**, *16*, 3200–3205.

[13] M. J. Rosen, B. Gu, D. S. Murphy, Z. H. Zhu, *Journal of colloid and interface science* **1989**, *129*, 468–475.

[14] R. F. Egerton, *Electron Energy-Loss Spectroscopy in the Electron Microscope*, Springer US, Boston, MA, **2011**.

[15] K.-M. Schindler, *Chemie in unserer Zeit* **1996**, *30*, 32–38.

[16] S. N. Magonov, M.-.-H. Whangbo, *Surface Analysis with STM and AFM*, Wiley, **1995**.

[17] J. Daillant, A. Gibaud, *X-ray and neutron reflectivity: Principles and applications*, Springer, Berlin, Heidelberg, **2009**.

[18] P. R. Griffiths, J. A. de Haseth, *Fourier transform infrared spectrometry*, 2nd ed., Wiley-Interscience, Hoboken, N.J, **2007**.

[19] M. P. Fuller, P. R. Griffiths, *Analytical chemistry* **1978**, *50*, 1906–1910.

[20] Zhu, Suhr, Shen, *Physical review. B Condensed matter* **1987**, *35*, 3047–3050.

[21] G. Korosi, E. S. Kovats, *Journal of Chemical & Engineering Data* **1981**, *26*, 323–332.

[22] D. F. Evans, H. Wennerström, *The colloidal domain: Where physics, chemistry, biology, and technology meet*, VCH, New York, NY, **1994**.

[23] D. L. Hu, B. Chan, J. W. M. Bush, *Nature* **2003**, *424*, 663–666.

[24] M. S. Gordon, R. Blickhan, J. O. Dabiri, J. J. Videler, *Animal Locomotion: Physical Principles and Adaptations*, CRC Press, Milton, **2017**.

[25] M. J. Rosen, J. T. Kunjappu, *Surfactants and interfacial phenomena*, 4. ed., Wiley, Hoboken, NJ, **2012**.

[26] T. Tadros in *Encyclopedia of Colloid and Interface Science*, Springer Berlin Heidelberg, Berlin, Heidelberg, **2013**, pp. 1164–1165.

[27] A. Mohsenipour, R. Pal in *Handbook of surface and colloid chemistry*, CRC Press, Boca Raton, **2016**, pp. 639–684.

[28] A. Patist in *Handbook of applied surface and colloid chemistry*, *Vol. 2*, Wiley, Chichester, **2002**, pp. 239–248.

[29] A. J. Prosser, E. I. Franses, *Colloids and Surfaces A: Physicochemical and Engineering Aspects* **2001**, *178*, 1–40.

[30] P. Warszyński, W. Barzyk, K. Lunkenheimer, H. Fruhner, *The Journal of Physical Chemistry B* **1998**, *102*, 10948–10957.

[31] J. T. Davies, *Proceedings of the Royal Society of London. Series A. Mathematical and Physical Sciences* **1958**, *245*, 417–428.

[32] J. T. Davies, E. K. Rideal, *Interfacial phenomena*, 2. ed., 6. print, Acad. Pr, New York, **1981**.

[33] P. A. Kralchevsky, K. D. Danov, G. Broze, A. Mehreteab, *Langmuir: The ACS Journal of Surfaces and Colloids* **1999**, *15*, 2351–2365.

[34] R. P. Borwankar, D. T. Wasan, *Chemical Engineering Science* **1988**, *43*, 1323–1337.

[35] V. V. Kalinin, C. J. Radke, *Colloids and Surfaces A: Physicochemical and Engineering Aspects* **1996**, *114*, 337–350.

[36] M. Gouy, *Journal de Physique Théorique et Appliquée* **1910**, *9*, 457–468.

[37] D. L. Chapman, *The London Edinburgh and Dublin Philosophical Magazine and Journal of Science* **1913**, *25*, 475–481.

[38] W. B. Russel, D. A. Saville, W. R. Schowalter, *Colloidal dispersions*, 1. paperback ed., Cambridge Univ. Press, Cambridge, **2001**.

[39] Y. Burak, D. Andelman, *Physical review. E Statistical physics plasmas fluids and related interdisciplinary topics* **2000**, *62*, 5296–5312.

[40] J. N. Israelachvili, *Intermolecular and surface forces*, 12. Aufl., Academic Press, London, **2007**.

[41] C. M. Phan in *Physical chemistry of gas-liquid interfaces*, Developments in physical & theoretical chemistry, Elsevier, Amsterdam, **2018**, pp. 79–104.

[42] H.-J. Butt, K. Graf, M. Kappl, *Physics and chemistry of interfaces*, 1. ed., Wiley-VCH, Weinheim, **2003**.

[43] O. Stern in *Otto Sterns Veröffentlichungen – Band 2*, Springer Berlin Heidelberg, Berlin, Heidelberg, **2016**, pp. 197–206.

[44] D. C. Grahame, *Chemical reviews* **1947**, *41*, 441–501.

[45] B. E. Conway, *Journal of The Electrochemical Society* **1991**, *138*, 1539.

[46] B. E. Conway, W. G. Pell, *Journal of Solid State Electrochemistry* **2003**, *7*, 637–644.

[47] W. Schmickler, D. Henderson, *The Journal of Chemical Physics* **1984**, *80*, 3381–3386.

[48] M. Peng, A. V. Nguyen, *Advances in Colloid and Interface Science* **2020**, *275*, 102052.

[49] S. R. Middleton, N. R. Pallas, J. Mingins, B. A. Pethica, *The Journal of Physical Chemistry C* **2011**, *115*, 8056–8063.

[50] C. A. MacLeod, C. J. Radke, *Langmuir: The ACS Journal of Surfaces and Colloids* **1994**, *10*, 3555–3566.

[51] T. Gilányi, I. Varga, R. Mészáros, *Phys. Chem. Chem. Phys.* **2004**, *6*, 4338–4346.

[52] K. Lunkenheimer, D. Prescher, R. Hirte, K. Geggel, *Langmuir* **2015**, *31*, 970–981.

[53] P. M. Holland, D. N. Rubingh in *Mixed surfactant systems*, ACS Symposium Series, American Chemical Society, Washington, DC, **1992**, pp. 2–30.

[54] B. Kronberg, K. Holmberg, B. Lindman in *Surface chemistry of surfactants and polymers*, John Wiley & Sons Ltd, Chichester, West Sussex, **2014**, pp. 251–269.

[55] J. H. Clint, *Journal of the Chemical Society Faraday Transactions 1: Physical Chemistry in Condensed Phases* **1975**, *71*, 1327.

[56] M. Aratono, T. Kanda, K. Motomura, *Langmuir: The ACS Journal of Surfaces and Colloids* **1990**, *6*, 843–846.

[57] Y. J. Nikas, S. Puvvada, D. Blankschtein, *Langmuir: The ACS Journal of Surfaces and Colloids* **1992**, *8*, 2680–2689.

[58] G. Kume, M. Gallotti, G. Nunes, *Journal of Surfactants and Detergents* **2008**, *11*, 1–11.

[59] Q. Zhou, M. J. Rosen, *Langmuir: The ACS Journal of Surfaces and Colloids* **2003**, *19*, 4555–4562.

[60] P. M. Holland, D. N. Rubingh in *Cationic surfactants*, Surfactant science series, Dekker, New York, NY, **1991**, pp. 141–189.

[61] P. M. Holland, D. N. Rubingh, *The Journal of Physical Chemistry* **1983**, *87*, 1984–1990.

[62] E. Frotscher, J. Höring, G. Durand, C. Vargas, S. Keller, *Analytical chemistry* **2017**, *89*, 3245–3249.

[63] M. N. Islam, T. Okano, T. Kato, *Langmuir: The ACS Journal of Surfaces and Colloids* **2002**, *18*, 10068–10074.

[64] P. Sehgal, O. Kosaka, H. Doe, D. E. Otzen, *Journal of Dispersion Science and Technology* **2009**, *30*, 1050–1058.

[65] S.-Y. Lin, Y.-Y. Lin, E.-M. Chen, C.-T. Hsu, C.-C. Kwan, *Langmuir: The ACS Journal of Surfaces and Colloids* **1999**, *15*, 4370–4376.

[66] K. Szymczyk, B. Jańczuk, *Colloids and Surfaces A: Physicochemical and Engineering Aspects* **2007**, *293*, 39–50.

[67] E. Lucassen-Reynders, J. Lucassen, D. Giles, *Journal of colloid and interface science* **1981**, *81*, 150–157.

[68] J. Rodakiewicz-Nowak, *Journal of colloid and interface science* **1982**, *85*, 586–591.

[69] A. Patist, S. Devi, D. O. Shah, *Langmuir: The ACS Journal of Surfaces and Colloids* **1999**, *15*, 7403–7405.

[70] D. Góralczyk, *Journal of colloid and interface science* **1980**, *77*, 68–75.

[71] C. Tondre, C. Caillet, *Advances in Colloid and Interface Science* **2001**, *93*, 115–134.

[72] A. Khan, E. Marques in *Specialist Surfactants*, Springer Netherlands, Dordrecht, **1997**, pp. 37–80.

[73] E. F. Marques, O. Regev, A. Khan, M. da Graça Miguel, B. Lindman, *The Journal of Physical Chemistry B* **1998**, *102*, 6746–6758.

[74] S. Ghosh, A. Ray, N. Pramanik, B. Ambade, *Comptes Rendus Chimie* **2016**, *19*, 951–954.

[75] Z.-J. Yu, G.-X. Zhao, *Journal of colloid and interface science* **1993**, *156*, 325–328.

[76] K. Motomura, M. Aratono in *Mixed surfactant systems*, Surfactant science series, Dekker, New York, NY, **1993**, pp. 100–144.

[77] D. Góralczyk, *Journal of colloid and interface science* **1996**, *179*, 211–217.

[78] M. Aratono, M. Villeneuve, T. Takiue, N. Ikeda, H. Iyota, *Journal of colloid and interface science* **1998**, *200*, 161–171.

[79] Matsuki, Aratono, Kaneshina, Motomura, *Journal of colloid and interface science* **1997**, *191*, 120–130.

[80] A. G. Lambert, P. B. Davies, D. J. Neivandt, *Applied Spectroscopy Reviews* **2005**, *40*, 103–145.

[81] H. Arnolds, M. Bonn, *Surface Science Reports* **2010**, *65*, 45–66.

[82] X. Zhuang, P. B. Miranda, D. Kim, Y. R. Shen, *Physical review. B Condensed matter* **1999**, *59*, 12632–12640.

[83] H.-F. Wang, W. Gan, R. Lu, Y. Rao, B.-H. Wu, *International Reviews in Physical Chemistry* **2005**, *24*, 191–256.

[84] M. Buck, M. Himmelhaus, *Journal of Vacuum Science & Technology A: Vacuum Surfaces and Films* **2001**, *19*, 2717.

[85] M. J. Hofmann, P. Koelsch in *Soft matter at aqueous interfaces*, Lecture notes in physics, Springer, Heidelberg, **2016**, pp. 491–513.

[86] G. L. Richmond, *Chemical reviews* **2002**, *102*, 2693–2724.

[87] M. R. Watry, M. G. Brown, G. L. Richmond, *Applied Spectroscopy* **2016**, *55*, 321A–340A.

[88] S. Ebnesajjad, A. H. Landrock in *Adhesives Technology Handbook*, Elsevier, **2015**, pp. 19–34.

[89] P. L. Du Noüy, *The Journal of general physiology* **1919**, *1*, 521–524.

[90] L. Wilhelmy, *Annalen der Physik und Chemie* **1863**, *195*, 177–217.

[91] M. Korenko, F. Šimko, *Journal of Chemical & Engineering Data* **2010**, *55*, 4561–4573.

[92] J. D. Berry, M. J. Neeson, R. R. Dagastine, D. Y. C. Chan, R. F. Tabor, *Journal of colloid and interface science* **2015**, *454*, 226–237.

[93] J.-H. Fuhrhop, T. Wang, *Chemical reviews* **2004**, *104*, 2901–2937.

[94] G. H. Escamilla, G. R. Newkome, *Angewandte Chemie International Edition in English* **1994**, *33*, 1937–1940.

[95] N. Aydogan, N. L. Abbott, *Journal of colloid and interface science* **2001**, *242*, 411–418.

[96] G. Mao, Y.-H. Tsao, M. Tirrell, H. T. Davis, V. Hessel, J. van Esch, H. Ringsdorf, *Langmuir: The ACS Journal of Surfaces and Colloids* **1994**, *10*, 4174–4184.

[97] Y. Yan, J. Huang, Z. Li, X. Zhao, B. Zhu, J. Ma, *Colloids and Surfaces A: Physicochemical and Engineering Aspects* **2003**, *215*, 263–275.

[98] N. Jayasuriya, S. Bosak, S. L. Regen, *Journal of the American Chemical Society* **1990**, *112*, 5844–5850.

[99] R. Fornasier, P. Scrimin, P. Tecilla, U. Tonellato, *Journal of the American Chemical Society* **1989**, *111*, 224–229.

[100] Y. Yan, T. Lu, J. Huang, *Journal of colloid and interface science* **2009**, *337*, 1–10.

[101] Y. Yan, W. Xiong, J. Huang, Z. Li, X. Li, N. Li, H. Fu, *The Journal of Physical Chemistry B* **2005**, *109*, 357–364.

[102] F. Menger, S. Wrenn, *The Journal of Physical Chemistry* **1974**, *78*, 1387–1390.

[103] K. Lunkenheimer, G. Czichocki, R. Hirte, W. Barzyk, *Colloids and Surfaces A: Physicochemical and Engineering Aspects* **1995**, *101*, 187–197.

[104] A. Javadi, N. Mucic, D. Vollhardt, V. B. Fainerman, R. Miller, *Journal of colloid and interface science* **2010**, *351*, 537–541.

[105] G. Czichocki, D. Vollhardt, H. Much, *Journal of colloid and interface science* **1983**, *95*, 275–276.

[106] H. Fauser, M. Uhlig, R. Miller, R. von Klitzing, *The Journal of Physical Chemistry B* **2015**, *119*, 12877–12886.

[107] K. Motomura, N. Ando, H. Matsuki, M. Aratono, *Journal of colloid and interface science* **1990**, *139*, 188–197.

[108] V. Fainerman, E. Lucassen-Reynders, *Advances in Colloid and Interface Science* **2002**, *96*, 295–323.

[109] M. J. Schwuger, *Kolloid-Zeitschrift und Zeitschrift für Polymere* **1971**, *243*, 129–135.

[110] V. B. Fainerman, E. V. Aksenenko, N. Mucic, A. Javadi, R. Miller, *Soft Matter* **2014**, *10*, 6873–6887.

[111] V. I. Kovalchuk, R. Miller, V. B. Fainerman, G. Loglio, *Advances in Colloid and Interface Science* **2005**, *114-115*, 303–312.

[112] C. Stubenrauch, V. B. Fainerman, E. V. Aksenenko, R. Miller, *The journal of physical chemistry. B* **2005**, *109*, 1505–1509.

[113] N. Schelero, R. von Klitzing, V. B. Fainerman, R. Miller, *Colloids and Surfaces A: Physicochemical and Engineering Aspects* **2012**, *413*, 115–118.

[114] Xi Yuan Hua, M. J. Rosen, *Journal of colloid and interface science* **1988**, *124*, 652–659.

[115] X.-C. Wang, L. Zhang, Q.-T. Gong, L. Zhang, L. Luo, Z.-Q. Li, S. Zhao, J.-Y. Yu, *Journal of Dispersion Science and Technology* **2009**, *30*, 137–143.

[116] V. B. Fainerman, A. V. Makievski, R. Miller, *Colloids and Surfaces A: Physicochemical and Engineering Aspects* **1994**, *87*, 61–75.

[117] J. Eastoe, J. Dalton, *Advances in Colloid and Interface Science* **2000**, *85*, 103–144.

[118] A. V. Makievski, V. B. Fainerman, R. Miller, M. Bree, L. Liggieri, F. Ravera, *Colloids and Surfaces A: Physicochemical and Engineering Aspects* **1997**, *122*, 269–273.

[119] A. F. H. Ward, L. Tordai, *The Journal of Chemical Physics* **1946**, *14*, 453–461.

[120] E. Rillaerts, P. Joos, *The Journal of Physical Chemistry* **1982**, *86*, 3471–3478.

[121] K. Kinoshita, E. Parra, D. Needham, *Journal of colloid and interface science* **2017**, *504*, 765–779.

[122] K. D. Danov, P. A. Kralchevsky, K. P. Ananthapadmanabhan, A. Lips, *Journal of colloid and interface science* **2006**, *303*, 56–68.

[123] J. Eastoe, J. Dalton, P. Rogueda, D. Sharpe, J. Dong, J. R. P. Webster, *Langmuir: The ACS Journal of Surfaces and Colloids* **1996**, *12*, 2706–2711.

[124] R. Teppner, K. Haage, D. Wantke, H. Motschmann, *The Journal of Physical Chemistry B* **2000**, *104*, 11489–11496.

[125] M. G. Brown, E. A. Raymond, H. C. Allen, L. F. Scatena, G. L. Richmond, *The Journal of Physical Chemistry A* **2000**, *104*, 10220–10226.

[126] D. E. Gragson, B. M. McCarty, G. L. Richmond, *Journal of the American Chemical Society* **1997**, *119*, 6144–6152.

[127] E. Weißenborn, B. Braunschweig, *Molecules (Basel Switzerland)* **2019**, *24*.

[128] J. Schaefer, G. Gonella, M. Bonn, E. H. G. Backus, *Physical Chemistry Chemical Physics : PCCP* **2017**, *19*, 16875–16880.

[129] D. Lis, F. Cecchet, *Beilstein journal of nanotechnology* **2014**, *5*, 2275–2292.

[130] D. K. Hore, E. Tyrode, *The Journal of Physical Chemistry C* **2019**, *123*, 16911–16920.

[131] R. Lu, W. Gan, B.-H. Wu, Z. Zhang, Y. Guo, H.-F. Wang, *The journal of physical chemistry. B* **2005**, *109*, 14118–14129.

[132] K. M. Bratlie, K. Komvopoulos, G. A. Somorjai, *The Journal of Physical Chemistry C* **2008**, *112*, 11865–11868.

[133] E. K. Humphreys, M. T. L. Casford, P. K. Allan, C. P. Grey, S. M. Clarke, *The Journal of Physical Chemistry C* **2017**, *121*, 20567–20575.

[134] S. Ye, Y. Tong, A. Ge, L. Qiao, P. B. Davies, *The Chemical Record* **2014**, *14*, 791–805.

[135] K. Engelhardt, W. Peukert, B. Braunschweig, *Current Opinion in Colloid & Interface Science* **2014**, *19*, 207–215.

[136] G. R. Bell, C. D. Bain, R. N. Ward, *Journal of the Chemical Society Faraday Transactions* **1996**, *92*, 515.

[137] M. C. Messmer, J. C. Conboy, G. L. Richmond, *Journal of the American Chemical Society* **1995**, *117*, 8039–8040.

[138] K. T. Nguyen, A. V. Nguyen, G. M. Evans, *The Journal of Physical Chemistry C* **2015**, *119*, 15477–15481.

[139] E. Brandes, Dissertation, Universität Regensburg, Regensburg, **2019**.

[140] L. B. Dreier, Y. Nagata, H. Lutz, G. Gonella, J. Hunger, E. H. G. Backus, M. Bonn, *Science Advances* **2018**, *4*, 7415.

[141] P. E. Ohno, H.-F. Wang, F. M. Geiger, *Nature communications* **2017**, *8*, 1032.

[142] S. Z. Can, C. F. Chang, R. A. Walker, *Biochimica et Biophysica Acta* **2008**, *1778*, 2368–2377.

[143] E. Tyrode, J. Hedberg, *The Journal of Physical Chemistry C* **2011**, *116*, 1080–1091.

[144] G. Ma, H. C. Allen, *Photochemistry and photobiology* **2006**, *82*, 1517–1529.

[145] G. Ma, H. C. Allen, *Langmuir : the ACS journal of surfaces and colloids* **2006**, *22*, 5341–5349.

[146] S. K. Das, S. Sengupta, L. Velarde, *The journal of physical chemistry letters* **2016**, *7*, 320–326.

[147] G. S. Aleiner, O. G. Us'yarov, *Colloid Journal* **2010**, *72*, 731–736.

[148] K. T. Nguyen, A. V. Nguyen, *Langmuir* **2019**, *35*, 4825–4833.

[149] K. T. Nguyen, A. V. Nguyen, *Soft Matter* **2014**, *10*, 6556–6563.

[150] K. T. Nguyen, T. D. Nguyen, A. V. Nguyen, *Langmuir* **2014**, *30*, 7047–7051.

[151] R. C. Fort, P. v. R. Schleyer, *Chemical reviews* **1964**, *64*, 277–300.

[152] H. Schwertfeger, A. A. Fokin, P. R. Schreiner, *Angewandte Chemie (International ed. in English)* **2008**, *47*, 1022–1036.

[153] R. Hrdina, *Synthesis* **2019**, *51*, 629–642.

[154] E. A. Shokova, V. V. Kovalev, *Russian Journal of Organic Chemistry* **2012**, *48*, 1007–1040.

[155] M. Mella, M. Freccero, T. Soldi, E. Fasani, A. Albini, *The Journal of Organic Chemistry* **1996**, *61*, 1413–1422.

[156] M. A. Gunawan, J.-C. Hierso, D. Poinsot, A. A. Fokin, N. A. Fokina, B. A. Tkachenko, P. R. Schreiner, *New J. Chem.* **2014**, *38*, 28–41.

[157] L. Wanka, K. Iqbal, P. R. Schreiner, *Chemical reviews* **2013**, *113*, 3516–3604.

[158] A. A. Spasov, T. V. Khamidova, L. I. Bugaeva, I. S. Morozov, *Pharmaceutical Chemistry Journal* **2000**, *34*, 1–7.

[159] A. Štimac, M. Šekutor, K. Mlinarić-Majerski, L. Frkanec, R. Frkanec, *Molecules (Basel Switzerland)* **2017**, *22*.

[160] J. Wang, J. R. Schnell, J. J. Chou, *Biochemical and Biophysical Research Communications* **2004**, *324*, 212–217.

[161] L. H. Pinto, R. A. Lamb, *Trends in Microbiology* **1995**, *3*, 271.

[162] J. W. Guo, X. Zhong, H. Zhu, L. J. Feng, Y. de Cui, *Chinese Chemical Letters* **2012**, *23*, 653–656.

[163] T. Yoshimura, M. Okada, K. Matsuoka, *Journal of Oleo Science* **2016**, *65*, 843–852.

[164] E. V. Vashkevich, N. Y. Yurashevich, N. G. Kozlov, V. I. Potkin, T. N. Potkina, *Russian Journal of Applied Chemistry* **2001**, *74*, 1892–1898.

[165] M. J. Hofmann, H. Motschmann, *Colloids and Surfaces A: Physicochemical and Engineering Aspects* **2017**, *529*, 1024–1029.

[166] J. Wang, A. V. Nguyen, S. Farrokhpay, *Colloids and Surfaces A: Physicochemical and Engineering Aspects* **2016**, *488*, 70–81.

[167] A. Stocco, D. Carriere, M. Cottat, D. Langevin, *Langmuir : the ACS journal of surfaces and colloids* **2010**, *26*, 10663–10669.

[168] D. Varade, D. Carriere, L. R. Arriaga, A.-L. Fameau, E. Rio, D. Langevin, W. Drenckhan, *Soft Matter* **2011**, *7*, 6557.

[169] C. Wang, H. Fang, Q. Gong, Z. Xu, Z. Liu, L. Zhang, L. Zhang, S. Zhao, *Energy & Fuels* **2016**, *30*, 6355–6364.

[170] J. Ferreira, A. Mikhailovskaya, A. Chenneviere, F. Restagno, F. Cousin, F. Muller, J. Degrouard, A. Salonen, E. F. Marques, *Soft Matter* **2017**, *13*, 7197–7206.

[171] R. Tuinier, C. G. Bisperink, C. van den Berg, A. Prins, *Journal of colloid and interface science* **1996**, *179*, 327–334.

[172] Z. Xue, A. J. Worthen, C. Da, A. Qajar, I. R. Ketchum, S. Alzobaidi, C. Huh, M. Prodanović, K. P. Johnston, *Langmuir* **2016**, *32*, 28–37.

[173] M. A. Upshur, M. M. Vega, A. G. Bé, H. M. Chase, Y. Zhang, A. Tuladhar, Z. A. Chase, L. Fu, C. J. Ebben, Z. Wang, S. T. Martin, F. M. Geiger, R. J. Thomson, *Chemical science* **2019**, *10*, 8390–8398.

[174] P. Balzerowski, K. Meister, J. Versluis, H. J. Bakker, *Physical Chemistry Chemical Physics : PCCP* **2016**, *18*, 2481–2487.

[175] L. Kong, C. Lee, S. H. Kim, G. R. Ziegler, *The Journal of Physical Chemistry B* **2014**, *118*, 1775–1783.

[176] S. Kataoka, P. S. Cremer, *Journal of the American Chemical Society* **2006**, *128*, 5516–5522.

[177] N. Ji, Y.-R. Shen, *The Journal of Chemical Physics* **2004**, *120*, 7107–7112.

[178] A. M. Buchbinder, E. Weitz, F. M. Geiger, *Journal of the American Chemical Society* **2010**, *132*, 14661–14668.

[179] J. C. Conboy, M. C. Messmer, G. L. Richmond, *The Journal of Physical Chemistry B* **1997**, *101*, 6724–6733.

[180] J. Chen, C. Yang, J. Guo, D. Zhu, S. Fu, Z. Yang, X. Zhong, *Tenside Surfactants Detergents* **2016**, *53*, 120–126.

[181] M. A. Upshur, H. M. Chase, B. F. Strick, C. J. Ebben, L. Fu, H. Wang, R. J. Thomson, F. M. Geiger, *The journal of physical chemistry. A* **2016**, *120*, 2684–2690.

[182] A. Saha, H. P. Upadhyaya, A. Kumar, S. Choudhury, P. D. Naik, *The Journal of Physical Chemistry C* **2014**, *118*, 3145–3155.

[183] A. M. Buchbinder, E. Weitz, F. M. Geiger, *The Journal of Physical Chemistry C* **2010**, *114*, 554–566.

[184] E. Brandes, C. Stage, H. Motschmann, J. Rieder, R. Buchner, *The Journal of Chemical Physics* **2014**, *141*, 18C509.

[185] T. Kawaguchi, K. Shiratori, Y. Henmi, T. Ishiyama, A. Morita, *The Journal of Physical Chemistry C* **2012**, *116*, 13169–13182.

[186] J. Eastoe, M. H. Hatzopoulos, P. J. Dowding, *Soft Matter* **2011**, *7*, 5917.

[187] K. Nakamura, T. Shikata, *Langmuir: The ACS Journal of Surfaces and Colloids* **2006**, *22*, 9853–9859.

[188] P. Hassan, G. Fritz, E. W. Kaler, *Journal of colloid and interface science* **2003**, *257*, 154–162.

[189] G. Garg, P. A. Hassan, V. K. Aswal, S. K. Kulshreshtha, *The Journal of Physical Chemistry B* **2005**, *109*, 1340–1346.

[190] R. M. Fernandes, E. F. Marques, B. F. Silva, Y. Wang, *Journal of Molecular Liquids* **2010**, *157*, 113–118.

[191] T. Kato, M. Iwai, T. Seimiya, *Journal of colloid and interface science* **1989**, *130*, 439–447.

[192] D. Georgieva, A. Cagna, D. Langevin, *Soft Matter* **2009**, *5*, 2063.

[193] C. Stubenrauch, R. Miller, *The Journal of Physical Chemistry B* **2004**, *108*, 6412–6421.

[194] L. Wang, R.-H. Yoon, *International Journal of Mineral Processing* **2008**, *85*, 101–110.

[195] K. Wantke, K. Małysa, K. Lunkenheimer, *Colloids and Surfaces A: Physicochemical and Engineering Aspects* **1994**, *82*, 183–191.

[196] K. Wantke, H. Fruhner, J. Fang, K. Lunkenheimer, *Journal of colloid and interface science* **1998**, *208*, 34–48.

[197] J. Liu, J. C. Conboy, *Langmuir: The ACS Journal of Surfaces and Colloids* **2005**, *21*, 9091–9097.

[198] N. A. Anderson, L. J. Richter, J. C. Stephenson, K. A. Briggman, *Langmuir: The ACS Journal of Surfaces and Colloids* **2006**, *22*, 8333–8336.

[199] R. K. Ciszewski, B. P. Gordon, B. N. Muller, G. L. Richmond, *The Journal of Physical Chemistry B* **2019**, *123*, 8519–8531.

[200] R.-J. Feng, X. Li, Z. Zhang, Z. Lu, Y. Guo, *The Journal of Chemical Physics* **2016**, *145*, 244707.

[201] M. Schleeger, Y. Nagata, M. Bonn, *The journal of physical chemistry letters* **2014**, *5*, 3737–3741.

List of Figures

List of Tables

Eidesstattliche Erklärung

Ich, Alexander Anton Dietz, erkläre hiermit an Eides statt, dass ich die vorliegende Arbeit ohne unzulässige Hilfe Dritter und ohne Benutzung anderer als der angegebenen Hilfsmittel angefertigt habe; die aus anderen Quellen direkt oder indirekt übernommenen Daten und Konzepte sind unter Angabe des Literaturzitats gekennzeichnet. Die Arbeit wurde bisher weder im In- noch im Ausland in gleicher oder ähnlicher Form einer anderen Prüfungsbehörde vorgelegt. Von den vorgesehenen Rechtsfolgen habe ich Kenntnis genommen.

Ort, Datum	Unterschrift